Technical University of Denmark

DTU

Quality assessment of turbid media
milk and pharmaceuticals

Kamran, Faisal; Andersen, Peter E.

Publication date:
2014

Document Version
Publisher's PDF, also known as Version of record

[Link back to DTU Orbit](#)

DTU Library
Technical Information Center of Denmark

Quality assessment of turbid media:
Milk and Pharmaceuticals

Faisal Kamran

This thesis is presented for the degree of
Doctor of Philosophy
2014

Department of Photonics Engineering
Denmark Technical University
Denmark

Quality assessment of turbid media:
Milk and Pharmaceuticals

Biophotonics Team
Diode Lasers and LED Systems group
Department of Photonics Engineering
Technical University of Denmark
Frederiksborg 399
4000, Roskilde
Denmark
http://www.fotonik.dtu.dk

To my Mother and Father

Acknowledgements

Summary

The work presented in this thesis primarily aims at application and improvement of spectroscopic techniques for analysis of dairy products, like milk and yoghurt, and pharmaceutical solids, combining the fields of biomedical optics and near infrared (NIR) spectroscopy. A non-invasive non-contact technique called oblique incidence reflectometry (OIR) is explored for analysis of dairy products and is verified using Monte Carlo (MC) simulations as well. The accuracy of the results was comparable to photon time-of-flight (PTOF) spectroscopy measurements which provided independent validation of OIR. PTOF spectroscopy was then used for quantitative analysis of another turbid medium, pharmaceutical tablets. The application of PTOF spectroscopy is limited by few reasons, one being the use of MC data bases. To improve its potential in various other fields that require rather fast analysis, an analytical model was tested and validated to investigate its potential to replace MC data bases in homogeneous semi-infinite media.

OIR is a spatially resolved spectroscopic technique and in this thesis, work on OIR presents the challenges that needs to be tackled for successful application of the technique for in-line sample inspection. The analysis approach is validated on milk and yoghurt samples. MC simulations are used to provide sensitivity analysis of the technique with the current implemented system.

To perform a quantitative analysis of pharmaceutical tablets, a time-resolved new generation broadband PTOF spectroscopic system was used to conduct a comprehensive study. Results from compressed intact tablets show that, in the given dynamic range, PTOF spectroscopy can be a viable alternative to conventional NIR spectroscopy for drug content prediction in tablets. Also characterization of physical properties, influenced by particle size, form and external process parameters like compression force, is rather meaningful and direct in PTOF data.

To increase the potential applications of PTOF spectroscopy, a new recently developed time domain analytical solution to radiative transfer equation was evaluated using time-resolved data from liquid phantoms. The same data was used to compare the evaluations with models based on diffusion theory and MC simula-

tions. Evaluation showed results from analytical solution in agreement with MC simulations beyond diffusion approximation limits. This provided a potential increase in number of fields where PTOF spectroscopy can be used in future.

SUMMARY - DANSK

Arbejdet præsenteret i denne afhandling sigter primært på anvendelse af og forbedring af spektroskopiske teknikker til analyse af mejeriprodukter, såsom mælk og yoghurt, og farmaceutiske tabletter, og kombinerer således områderne biomedicinsk optik og nær infrarød (NIR) spektroskopi. En ikke-invasiv ikke-kontakt teknik, såkaldt oblique incidence reflectometry (OIR), er anvendt til analysen af mejeriprodukter, og valideret vha. Monte Carlo (MC) simuleringer. Nøjagtigheden af resultaterne var sammenlignelig med foton flyvetids (photon time-of-flight : PTOF) spektralanalytiske målinger, som uafhængigt validerede OIR. PTOF spektroskopi blev derefter anvendt til kvantitativ analyse af et andet kraftigt spredende medium; farmaceutiske tabletter. Anvendelsen af PTOF spektroskopi har visse begrænsninger, hvoraf en er brugen af såkaldte MC look-up databaser. For at forbedre metodens potentiale i andre anvendelsesområder, hvor der fx kræves hurtig analyse (real-tid), blev en analytisk model testet og valideret med henblik på at erstatte brugen af MC look-up databaser i homogent spredende halv-uendelige medier.

OIR er en rumligt opløst, ikke-kontakt spektroskopisk teknik og arbejdet i denne afhandling tager udgangspunkt i de udfordringer der ligger i at anvende OIR teknikken til in-line inspektion af prøver. Metoden er valideret på prøver af mælk og yoghurt prøver. Derudover anvendes MC simuleringer i en følsomhedsanalyse af OIR teknikken for den nuværende implementering af målesystemet.

En ny generation af et tidsopløst, bredbåndet PTOF spektroskopisk blev opbygget med henblik på at gennemføre en fyldestgørende kvantitativ analyse af farmaceutiske tabletter. Resultaterne fra komprimerede, intakte tabletter viser at PTOF spektroskopi kan være et velegnet alternativ til konventionel NIR spektroskopi til ikke-kontakt bestemmelse af koncentrationsmåling af lægemidler i det givne dynamikområde. Endvidere er karakterisering af eksterne procesparametre, såsom kompressionskraft, der direkte influerer partikelstørrelse og form, ligetil med denne metode.

For at forbedre anvendelsesmulighederne af PTOF spektroskopi blev en nyligt udviklet løsningsmetode baseret på en an-

alytisk løsning af transportligningen i tidsdomænet evalueret på tidsopløste data fra fantomer. De samme data blev anvendt til at sammenligne resultaterne fra modeller baseret på diffusionsteori og MC simuleringer. Sammenligningen viste at resultaterne fra den nye analytiske løsning udviste god overensstemmelse med MC simuleringerne, endda ud over diffusionsapproksimationens gyldighedsområde. Dette kan betyde langt flere fremtidige anvendelsesmuligheder for PTOF spektroskopi.

LIST OF PUBLICATIONS

This thesis is based on the following papers, which will be referred to in the text by their Roman numerals.

I **Non-invasive assessment of dairy products using spatially resolved diffuse reflectance spectroscopy**
Otto H. A. Nielsen, Faisal Kamran, Anders B. Dahl, Jacob L. Skytte, Frederik D. Nielsen, Carsten L. Thomsen, Peter E. Andersen, Rasmus Larsen, Jeppe R. Frisvad.
Applied Spectroscopy **14-07529**, Accepted (March 10, 2015) [1].

II **Transmission near-infrared and photon time-of-flight spectroscopy in a comparative analysis of pharmaceuticals**
Faisal Kamran, Otto H. A. Nielsen, Anders Sparén, Olof Svensson, Jonas Johansson, Stefan Andersson-Engels, Peter E. Andersen, Dmitry Khoptyar.
Applied Spectroscopy **69(3)**, 389-397 (2015) [2].

III **Computational effective solution of the inverse problem in time-of-flight spectroscopy**
Faisal Kamran, Otto H. A. Abildgaard, Arman A. Subash, Peter E. Andersen, Stefan Andersson-Engels, Dmitry Khoptyar.
Optics Express **23(5):**, 6937-6945 (2015) [3].

IV **Sensitivity analysis for Oblique incidence reflectometry using Monte Carlo simulations.**
Faisal Kamran, Peter E. Andersen.
Submitted to Applied Optics **237341**, April 1, 2015 [4].

Related publications not included in this thesis:

**Broadband photon time of flight spectroscopy:
Advanced spectroscopic analysis for ensuring safety
and performance of pharmaceutical tablets**
F. Kamran, O. H. A. Nielsen, S. A. Angels, D. Khoptyar.
ACP/IPOC **AF3KI.4**, OSA (2013) [5].

**Broadband photon time of flight spectroscopy:
advanced spectroscopic tool for PAT in
pharmaceutical and dairy industries**
D. Khoptyar, F. Kamran, O. H. A. Nielsen, A. Sparén,
J. Johansson, O. Svensson, S. A. Angels.
EuroPACT **(2014)** **[6]**,

.

Abbreviations

AOTF	acousto-optical tunnable filter
APD	avalanche photodiode
API	active pharmaceutical ingrediant
CF	compression force
CW	continuous wave
DM	diffusion model
DOS	diffuse optical spectroscopy
FOV	field of view
FPS	filler particle size
KFCV	k-fold cross validation
LKM	Liemert-Kienle model
LOOCV	leave one out cross validation
MCP	micro-channel palate
MCS	Monte Carlo simulations
MSC	multiplicative scatter correction
MVDA	mulitvariate data analysis
NIR	near-infrared
OIR	oblique incidence reflectometry
PC	principle component
PCA	principle component analysis
PLS	partial least squares
PLSR	partial least squares regression
PMT	photomultiplier tube
PTOF	photon time of flight
PTOFS	photon time of flight spectroscopy
RSS	residual sum of squares
RTE	radiative transport equation
RTT	radiative transport theory

SD	standard deviation
SPC	single photon counting
TCSPC	time correlated single photon counting
TI Amp	trans-impedance amplifier
TNIRS	transmission near-infrared spectroscopy
WMC	white monte carlo

CONTENTS

Papers

INTRODUCTION

1.1 Motivation

The safety and the quality of the consumable products, especially dairy products e.g., milk and yoghurt, and pharmaceuticals have always been of a major concern but never as much stressed and researched as in the last twenty years. With the increased awareness of the importance and requirements of the enforced high standards, companies are constantly investigating new and improved methods to ensure the safety and quality of their products.

Food industry demands the methods that are non-contact, non-invasive and fast to be possibly applied for in-line inspection of all the products. Not only the final product but also the changes in the structure through out the process are of the interest which require a stable monitoring technology. Pharmaceutical industry, on the other hand, uses the standard NIR spectroscopy for evaluation of the tablets. But the challenge is to develop the methods not only accurate enough to determine analytical parameters but also have an inherent robustness such that the prediction of drug concentration is insensitive to the variations in, e.g., raw material particle size and batch quality.

For the purpose of investigating these turbid media, two very different approaches are investigated. A diffusion based non-contact non invasive technique called oblique incidence reflectometry and an advanced time domain technique known as photon time-of-flight spectroscopy. The later technique is limited in it's application because of time consuming database requirements normally created using Monte Carlo simulations. An analytical fast solution to radiative transfer equation was implemented for time-of-flight data analysis to potentially increase it's application areas.

The work described in this thesis is mainly concerned with the quality assessment of dairy products (milk and yoghurt), pharma-

ceuticals, analysis of oblique incidence reflectometry and analytical modelling for time-of-flight spectroscopy.

1.2   Aims and outline of this thesis

The general aims of the work presented in this thesis are:

(i) to explore a non-invasive non-contact technique for in-line monitoring of dairy products like milk and yoghurt;

(ii) to investigate the potential applicability of oblique incidence reflectometry (OIR);

(iii) to explore the potential of photon time-of-flight spectroscopy (PTOFS) as a viable alternative for analysis of pharmaceuticals and

(iv) to increase the potential applications of PTOFS.

Scientific contributions made in pursuit of these goals, are published in the peer-reviewed scientific articles that are enclosed at the end of the thesis.

The thesis chapters, and their connections to the papers are outlined below:

Chapter 2 describes the interactions between light and turbid medium as light propagates through it. Overview includes scattering, index of refraction, absorption and anisotropy. In addition, an overview of the physical models used to describe light propagation in turbid media is provided, including the radiative transport equation, Monte Carlo simulations, the diffusion approximation and an analytical solution in time domain beyond diffusion approximation.

Chapter 3 provides the first part of OIR where theory and the modelling of the technique are discussed along with the limits for implementation of the technique (Paper **I**). Oblique Monte Carlo simulations are used to validate the technique.

Chapter 4 presents the contribution towards the development and improvement in OIR which is then applied in Paper **I**. Results on original OIR method are presented with validation from Lorenz-Mie theory and are also compared to previously published results. Sensitivity analysis is described for OIR for the resolution requirements for a system in different dynamic range of optical properties. This serves the basis for Paper **IV** which investigates the system requirements value of anisotropy of the medium.

Chapter 5 covers various aspects of PTOFS. Theory, setup

and advantages are discussed along with it's application to pharmaceuticals. In Paper **II**, PTOFS presented setup was used for comprehensive study on pharmaceuticals for quantitative analysis.

Chapter 6 presents the multivariate data analysis used in Paper **II**. PCA and PLS regression are discussed along with importance of pretreatment in spectroscopic techniques.

Chapter 7 discusses the potential increase in PTOFS application because of a more evolved time-domain analytical solution (LK-model) of radiative transport. Diffusion model is widely used but suffers from the limited validity under certain conditions. In Paper **III**, LK-model is compared with MC simulations and diffusion model experimentally using liquid phantoms.

LIGHT-MATTER INTERACTION AND MODELLING

Application of the techniques that use light, have increasingly become of great interest in large number of industries working with turbid media. Because of non-destructive, often non-invasive ability of measurements, photonics-based techniques require a good understanding of how light interacts when it comes in contact with matter. Light-matter interaction gives birth to a number of phenomena among which, absorption and scattering are the most significant ones and this chapter describes these phenomena, relevant to the methods investigated in this PhD thesis. When the light enters in a medium, it can get absorbed due to the absorption bands of the molecules [7]. In the scope of this thesis, only linear affects of absorption are considered where absorption strength depends on the light intensity. For other light absorption phenomena, references are provided [8, 9]. Light scattering originates from the interaction of photons with the structural heterogeneities present inside material bodies at the wavelength scale.

After the description of the relevant interactions, radiative transport equation (RTE) is introduced which is an accurate physical description of the light interaction with matter in real life. Discussion on the approaches used to model the RTE is followed based on numerical, analytical and diffusion based models.

2.1 Scattering

Turbid media consist of large quantities of inhomogeneities which are referred to as "scatterers". These scatterers, when in lights' path of trajectory, force it to deviate from its course and move in all the directions. Scattering in turbid media is due to several optical effects [10]. Tissue is an example of a turbid medium and the

light attenuation in a tissue depends on the wavelength of the incident light along with the medium characteristics. From a classical electromagnetic point of view, light is a propagating wave. Its encounter with scatterers (considered as charged particles) generates new radiating waves and their superposition determines the direction and the scale of the scattering [11]. However, in this thesis we will consider the particle nature of the light only from which the RTE is drawn. The phenomena like diffraction or interference are not considered for this reason.

Scattering can be further divided into two types. First is "elastic scattering" in which the wavelength of the scattered photon is similar to the incident wavelength. Rayleigh [12] and Mie scattering [13] are examples of elastic scattering. Scattering due to the particles over ∼10 times smaller than the wavelength causes the Rayleigh scattering. Mie scattering predominates when the size of the scatterer is comparable to the wavelength of the incident light. Another type of scattering called "inelastic scattering", where incident and scattering wavelengths are different from each other, is often very weak and examples include Raman [14] and Brillouin scattering [15–17]. In this thesis only elastic scattering is considered, i.e. where the energy, and thus the wavelength, is conserved in the scattering process.

Depending on the number density of the scatterers, two different regimes exist, i.e. single scattering and multiple scattering, and different calculation approaches can be applied to each of these regimes. Scattering by single particles is the subject of several books [18, 19] and so is multiple scattering [11, 19] but the summarized short descriptions for understanding are presented below.

2.1.1 Single-particle scattering

In 1871 Rayleigh [12, 20], explained the reason for the blue colour of the light by considering scatterers of much smaller size compared to the wavelength of incident light using Maxwell's equations. In modern electromagnetic scattering, a medium is defined by collection of charged particles with specific set of properties that define the medium. The size and shape of the particle are one of the fundamental properties in determining the scattered field, as they influence the probability of direction of scattering for photons. In 1908, Mie [13] improved upon it by introducing varying sizes of scatterers in the solution.

Scattering by a single particle can be expressed mathematically in two parameters: the scattering cross-section σ_{sca} and the scattering phase function, $p(\theta)$, where θ is the angle between incident and scattered photon. In Rayleigh scattering, the intensity of the scattered light, I_{sca}, increases with the shorter wavelength, approximately proportional to λ^{-4}; while in Mie scattering, it is proportional to λ^{-1}.

$$I_{\text{sca}}^{\text{Ray}} \propto \lambda^{-4}. \tag{2.1}$$

$$I_{\text{sca}}^{\text{Mie}} \propto a\lambda^{-b}. \tag{2.2}$$

Here, the coefficient a is related to the number density of the scatterers, and b to the size of the scatterer.

Final scattered field normally has the contribution from individual scatterers. For their small number density N_{sca} [cm^{-3}], with linearly independent contributions, the scattering property of the medium can be characterized by a scattering coefficient, μ_{s} [cm^{-1}]:

$$\mu_{\text{s}} = N_{\text{sca}}\sigma_{\text{sca}}, \tag{2.3}$$

which describes the scattering probability per unit length.

In turbid media like biological tissue the scattering of light is not isotropic (Rayleigh) rather exhibits dominant forward Mie scattering [21, 22]. The scattering phase function describes the normalized angular distribution of the power of the scattered field and is usually assumed to have dependence only on the deflection angle θ. Figure 2.1 illustrates the phase function. The shape of the phase function is determined by the size and refractive index of the spherical scatterer and the wavelength of the light incident upon it. The multiple side lobes in the phase function are due to interference effects.

Figure 2.1. *Mie scattering phase functions for dielectric spherical scatterers with a diameter of 2 μm and refractive index of 1.5, at wavelength = 1000 nm [23]*

2.1.2 Multiple scattering

In a highly scattering densely packed medium like dairy products (Paper **I**) and pharmaceuticals (Paper **II**), composed of scatterers with different sizes, shapes, refractive indices and orientation, the effect of the phase function dies out due to the sheer volume of scattering events. Instead of electromagnetic wave propagation a statistic description of the scattering medium is generally employed instead. In this case, the scattering material is described using an average scattering coefficient (μ_{s}), together with an average angular distribution function, i.e., the scattering phase function ($p(\cos\theta)$). μ_{s} defines the probability of scattering in a unit length. Its reciprocal, "mean free path", gives an estimate of distance a photon travels before encountering a scattering event. A well known Henyey-Greenstein phase function is commonly used to describe the angular distribution of the scattered light by tissues [21, 24, 25], and has the form:

$$p(\cos\theta) = \frac{1}{4\pi}\frac{1-g^2}{(1+g^2-2g\cos\theta)^{3/2}}. \tag{2.4}$$

Here, g is the anisotropy factor, defined as the average of the cosine of the scattering angles and characterizes the directionality

Figure 2.2. *Henyey-Greenstein scattering phase function for g = 0.95, g = 0.8, g = 0.5 and g = 0 (isotropic).*
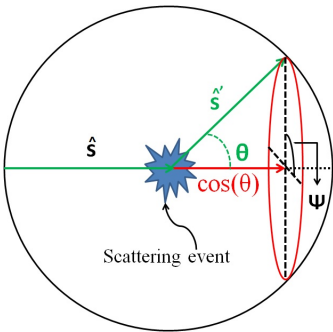
Figure 2.3. *A scattering event causes the photon to deflect at angle θ from original direction ŝ to ŝ'. ψ is the azimuthal angel of deflection. Modified from [29]*

of the scattered light. The Henyey-Greenstein phase function for different anisotropy factors is illustrated in Figure 2.2.

The so-called reduced scattering coefficient, μ'_s [cm^{-1}], is usually introduced to describe light scattering completely, which is defined by:

$$\mu'_s = (1 - g)\mu_s, \tag{2.5}$$

The wavelength dependence of the scattering parameter in a medium is related to the sizes of the scatterers. Generally, the scattering coefficient and the phase function exhibit a complex dependence on the wavelength. It is important to note that empirically observed scattering behaviour for small and intermediate sized particles is relatively well modelled [26, 27] by generalization of Equation (2.2) as:

$$\mu'_s = A(\frac{\lambda}{\lambda_0})^{-\beta}. \tag{2.6}$$

where A is the reduced scattering amplitude at reference wavelength λ_0 measured in μm while β is the slope of the wavelength dependent curve. This is known as "Power Law".

Equation (2.6) is a general description of the reduced scattering coefficient, described as a sum of the Mie-scattering and Rayleigh-scattering contributions with different weights [28]:

$$\mu'_s = a' \left[f_{\mathrm{Ray}}\lambda^{-4} + (1 - f_{\mathrm{Ray}})\lambda^{-b_{\mathrm{Mie}}} \right], \tag{2.7}$$

where a' is a scaling factor, f_{Ray} is the fraction of Rayleigh scattering, $(1 - f_{\mathrm{Ray}})$ is the fraction of Mie scattering, and b_{Mie} is the scattering power of Mie scattering.

2.1.3 Refractive index

Foundation of Equation (2.7) is based on not only on the particle size of scatterer but also on the ratio of the refractive index of the particle to the medium in which it is kept. A fundamental property of any medium is known as refractive index or index of refraction (n). In a medium with homogeneously distributed particles or molecules, it is defined in terms of the velocity of light in the medium:

$$c_m(\lambda) = \frac{c}{n(\lambda)} \tag{2.8}$$

where c is the speed of light in vacuum and λ is the wavelength of the light. The loss of the speed of light inside a medium is due to electric field interactions within the medium dipoles. The wavelength dependent index of refraction plays important role in determining the scattering behaviour of the medium. The reason is that the strength of scattering depends on the difference in refractive indices of the particles and the background. If the scatterers and the background have the same refractive index, light is no longer scattered by the particles.

Refractive index interestingly has rather more to it than simply dictating the direction and strength of the refracted light as stated by well known Snell's law. For the estimation of the optical properties using oblique incidence reflectometry (OIR), it plays rather important role and is addressed in Section 3.3.

2.2 Absorption

As discussed earlier, absorption is one of the most important interaction between light and matter and this quantum effect is based on absorption of the energy. Electromagnetic radiation can be described either as electromagnetic wave or as a stream of particles/photons. Both are valid depending on their application. However they both share an intrinsic relation given as:

$$E = \frac{hc}{\lambda} \tag{2.9}$$

where photons can be considered as electromagnetic waves with a particular wavelength λ and velocity c. h is the Planck's constant. A molecule is a charged system with difference in their ground state and excited state energy levels equal to E. Electrons are normally in the ground state in a molecule. They require quantized doze of energy to jump to the higher state, which they can take by absorbing a photon of the energy equal to the difference between the energy levels. As this energy match is essential, it makes absorption of light useful property in diagnostic role such as in spectroscopy of a turbid media. Absorption can provide a clues to identify the chemical composition of a sample and serve as a mechanism of optical contrast during imaging. The measured wavelength dependent absorption, μ_a, can be used as an identifier, or fingerprint of a substance. Absorption is used for both the spectroscopic, as shown in Figure 2.4, and imaging applications. Deposition of energy by the photon absorption is a primary event used in therapeutic applications.

Taking into account the contributions of all the absorbers present in a medium, when absorption by a single absorber can be described by the absorption cross-section, σ_{abs} [cm^2], we can express it as absorption coefficient of the medium:

$$\mu_a = N_{abs}\sigma_{abs}, \tag{2.10}$$

where N_{abs} [cm^{-3}] denotes the number density of the absorbers.

Energy of the incident beam can be lost due to absorption after passing through a small incremental distance, dL, described as:

$$dI = -\mu_a I dL. \tag{2.11}$$

This leads to the famous Beer-Lambert law, describing the transmitted light intensity after travelling through a homogeneous non-
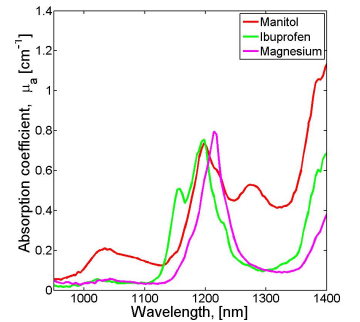
Figure 2.4. *Absorption spectra of pure ingredients used in manufacturing pharmaceutical tablets used in Paper **II***
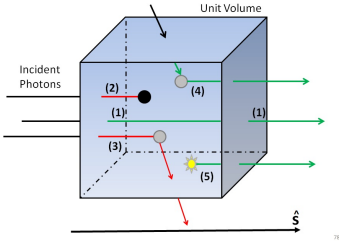
Figure 2.5. *Events considered in the derivation of the RTE. i) Photon transfer across the boundary. ii) Photon loss due to absorption. iii) Photon loss due to scattering. iv) Photon scattering in the ŝ direction from all other directions. v) Photons generated by the source.*

scattering, but absorbing medium [30]:

$$I = I_0 \exp(-\mu_a d), \tag{2.12}$$

where I [Wcm^{-2}] is the transmitted intensity, I_0 [Wcm^{-2}] is the incident intensity, and d [cm] is the thickness of the medium. In highly scattering media such as biological tissue, the Beer-Lambert law can be applied with modifications accounting for the distribution of the optical path lengths [31, 32].

2.3 Radiative Transport Theory and Equation

With optical properties defined, now we move to the central issue of modelling the light propagation in a turbid medium. Radiative transport theory (RTT) is the gold standard used for this purpose. Solving Maxwell's equation to model the light propagation in high scattering medium is impractical. Instead, RTT considers light as flow of neutral non-interacting particles (photons) i.e., light polarization and phase are not considered. Thus RTT becomes a model based on the energy transfer in a medium following the law of conservation of energy. The development of the RTT is the result of research in many areas of physics including radiation transfer [19, 33–35], neutron transport [36] and the diffusion of charged particles [37]. Early works include those by Reynolds et al. [38], Ishimaru et al. [19] and Longini et al. [39] which made it the gold standard [40].

Radiative transfer equation (RTE) is also known as Boltzmann equation. Heuristically constructed differential RTE describe the effects of absorption and scattering, considering conservation of energy in a small volume, V. Transport model is defined by a quantity called radiance, $L(\mathbf{r}, \hat{\mathbf{s}}, t)$ [Wm^{-2}sr^{-1}] which describes the radiant power flow along $\hat{\mathbf{s}}$ through unit area per steradian at position $\mathbf{r}$ and time t. All these effects including photon source and boundary are illustrated in Figure 2.5. RTE can be written as:

$$\frac{1}{c}\frac{\partial L}{\partial t} = -\underbrace{-\hat{\mathbf{s}} \cdot \nabla L}_{1)} - \underbrace{\mu_a L}_{2)} - \underbrace{\mu_s L}_{3)}$$

$$+ \mu_s \underbrace{\int_{4\pi} p(\hat{\mathbf{s}}, \hat{\mathbf{s}}')L(\hat{\mathbf{s}}')\mathrm{d}\Omega'}_{4)} + \underbrace{\mathbf{Q}}_{5)} \tag{2.13}$$

where c [ms^{-1}] is the energy transport speed in medium and $\mathbf{Q}(\mathbf{r}, \hat{\mathbf{s}}, t)$ [Wm^{-3}s^{-1}sr^{-1}] is a source term defining the energy produced per unit volume, per steradian at time t and position $\mathbf{r}$. $p(\hat{\mathbf{s}}, \hat{\mathbf{s}}')$ is the scattering phase function. dΩ' presents the differential solid angle element around $\hat{\mathbf{s}}'$ direction. Arguments for differ-

ent quantities are omitted for brevity unless considered necessary. The terms on the right-hand side describe the contributions of:

1) light transmission or transfer across the boundary;

2) absorption losses;

3) energy loss due to scattering from direction $\hat{\mathbf{s}}$;

4) added photons from scattering in the $\hat{\mathbf{s}}$ direction from all other directions, and

5) Source generating photons within the volume.

Because of coupling between all $\hat{\mathbf{s}}'$ direction, geometrical aspects and boundary conditions, the seemingly straight forward looking Equation (2.13) is in fact solvable for very few simple cases [41, 42]. For more involved applications, modelling of RTE is necessary.

2.4 Modeling of light propagation

The RTE describes particle propagation through a turbid medium where the transported particles and the host medium can have very different quantities. Several ways to model the RTE exist which include both numerical and analytical solutions. Monte Carlo (MC) simulations is a stochastic approach to solve RTE. Discrete ordinates method [36][43, 44] can also be solved numerically. Some semi-analytical and analytical approaches are based on spherical harmonics [45–48], simplified spherical harmonics [49–54] and diffusion approximation. Methods relevant for this thesis are discussed below.

2.4.1 MCS

The Monte Carlo (MC) method involves stochastic numerical simulations of the RTE by tracing fictional particles through the medium. In the limit of infinitely many particles traced, MC is an exact solution to the RTE and is often used as the gold standard for modelling the light propagation in complex structures as well as for the evaluation of other solution techniques.

Monte Carlo (MC) methods have been used for several decades in order to investigate complex physical processes such as radiative transport [55, 56]. This numerical approach has become the gold standard for modelling of photon migration in biomedical optics [57, 58] even for complicated structures like human head [59]. The freely available Monte Carlo implementation for light propagation in layered structures (MCML) has become a standard tool [58] and commercial alternatives are available [60]. The fundamentals

of Monte Carlo modelling for light propagation are carefully described in several articles and books [61–64]. A summary of various MC techniques used for light propagation in tissue are discussed by Zhu et al., [65].

Briefly, photons are launched and tracked in an arbitrary geometry with pre-defined optical properties (absorption and scattering), relying on proper generation of random numbers [64] and collecting the final photon density distribution on a sensor. The large number of function evaluations renders numerical considerations important [66, 67]. In Paper **II** we used specially developed White Monte Carlo (WMC) method [68–70], i.e. a single Monte Carlo simulation is run at zero absorption. The result can be scaled in order to apply for different scattering coefficients, and absorption is added in the final step. Paper **III** used WMC model as gold standard to compare the performance of other models with. Paper **IV** is based on MCS to explore the sensitivity of oblique incidence reflectometry and validate the experimental results presented in Paper **I**.

The main problem faced with MC simulations is the computational time as the simulations are used for creating precomputed look-up tables of the reflectance profiles [71]. In the work presented in Paper **III**, a library of precomputed MC simulations was used for evaluation and comparison of optical properties for different models. The models used for building the library was first presented by Alerstam et al. [70, 72] which is a continuation of the White Monte Carlo Light (WMCL) model developed by Wang et al. [58]. Paper **IV** used MC simulations algorithm built by S. Jacques [73].

2.4.2 Analytical solutions

As RTE is the closest description of a real world interaction between light and matter, analytical solutions may provide a closed exact form expression for modelling the RTE. However, these solutions have been solved for only few geometries and can not be generalized. Compared to MCS, analytical solutions are computationally time efficient [74].

As RTE is infeasible to solve in most of the cases, it is normally expanded on the basis of spherical harmonics yielding Legendre polynomials P_N. Truncating the series after N terms may lead to a semi-analytical solution that often provides a series of equations to be numerically solved [45, 46] which can take considerable time. In certain cases exact analytical solutions may be found as shown by Liemert and Kienle [47, 48, 74] and used in Paper **III**.

2.4.3 Diffusion approximation

Diffusion of the light has been extensively published and is a topic that would require reviews of many different fields which can not be covered in the scope of this thesis. For this reasons, the bibliography refers mainly to the publications in the field of biomedical optics and more precisely to the field of near infra-red spectroscopy (NIRS) and diffuse optical spectroscopy (DOS). A more complete picture of RTE and approximations for diffusion consideration can be seen in the referred books [19, 35, 36, 75, 76].

In special case when expansion series is truncated for $N = 1$ with some other simplifications, RTE turns into the diffusion approximation. This makes it possible to find the closed expression solution to RTE which is often adequate to apply and very fast as well. Major assumption is that radiance is nearly isotropic in high-albedo ($\mu_s \gg \mu_a$) scattering media [64]. This puts a limit that diffusion model is valid away from the source [41]. With this simplification, radiance can be expressed as:

$$L(\mathbf{r}, \hat{\mathbf{s}}, t) \approx \frac{1}{4\pi}\Phi(\mathbf{r}, t) + \frac{3}{4\pi}\mathbf{J}(\mathbf{r}, t) \cdot \hat{\mathbf{s}}, \qquad (2.14)$$

where $\Phi(\mathbf{r}, t)$ [Wm^{-2}] and $\mathbf{J}(\mathbf{r}, t)$ [Wm^{-2}] are the fluence rate and the flux respectively, expressed as:

$$\Phi(\mathbf{r}, t) = \int_{4\pi} L(\mathbf{r}, \hat{\mathbf{s}}, t)\mathrm{d}\Omega, \qquad (2.15)$$

and

$$\mathbf{J}(\mathbf{r}, t) = \int_{4\pi} L(\mathbf{r}, \hat{\mathbf{s}}, t)\hat{\mathbf{s}}\mathrm{d}\Omega, \qquad (2.16)$$

$\mathrm{d}\Omega$ is differential solid angle around the direction $\hat{s}$. In addition, the source is assumed to be isotropic:

$$\mathbf{Q}(\mathbf{r}, \hat{s}, t) = \frac{1}{4\pi}\mathbf{Q}(\mathbf{r}, t). \qquad (2.17)$$

Equation (2.14) and Equation (2.17) can be used in Equation (2.13) to get two coupled equations[1];

$$\left(\frac{1}{c}\frac{\partial}{\partial t} + \mu_a\right)\Phi + \nabla\mathbf{J} = \mathbb{Q}, \qquad (2.18)$$

$$\left(\frac{1}{c}\frac{\partial}{\partial t} + \mu_a + \mu_s'\right)\mathbf{J} + \frac{1}{3}\nabla\Phi = 0. \qquad (2.19)$$

---

[1]1)by integrating over all $\hat{\mathbf{s}}$ and 2) by first multiplying by $\hat{\mathbf{s}}$ before integrating over all $\hat{\mathbf{s}}$

Assuming that fractional change in flux is negligible[2] i.e., $\partial \mathbf{J}/\partial t = 0$, Equation (2.19) becomes Fick's law[3] of diffusion:

$$\mathbf{J} = -D\nabla\Phi, \tag{2.20}$$

where D [m] is known as the diffusion coefficient expressed as:

$$D = \frac{1}{3(\mu_a + \mu_s')} \tag{2.21}$$

The assumption of negligible change in flux is valid for $\omega \ll \mu_s'c$ [77, 78]. ω is the angular modulation frequency, time correlated via Fourier transform. The diffusion equation can be obtained by inserting Equation (2.20) into Equation (2.18):

$$\frac{1}{c}\frac{\partial\Phi(\mathbf{r},t)}{\partial t} + \mu_a(\mathbf{r})\Phi(\mathbf{r},t) - \nabla\cdot[D(\mathbf{r})\nabla\Phi(\mathbf{r},t)] = \mathbf{Q}(\mathbf{r},t). \tag{2.22}$$

For an infinitely short-pulsed point source $\mathbf{Q}(\mathbf{r},t) = \delta(\mathbf{r},t)$, diffusion equation has a solution of the form

$$\Phi(r,t) = \frac{c}{(4\pi Dct)^{3/2}}\exp(-\frac{r^2}{4Dct} - \mu_a ct). \tag{2.23}$$

which is the impulse response[4] for homogeneous scattering infinite medium for t > 0.

The obtained diffusion equation contains μ_a in it which has been a topic of the debate for several authors [77, 79–82]. Inclusion or exclusion of absorption influences the outcome of diffusion coefficient (Equation (2.21)), the diffusion equation (Equation (2.22)) and its solution (Equation (2.23)). It is shown that in the steady state solutions, the diffusion coefficient depends on absorption but in time-domain, it is independent [83].

The analytical solutions, in combination with the fact that diffusion in many cases is a sufficiently good approximation of RTE, have made diffusion solutions the most widely employed theory to solve the radiative transport problem. Paper **I** is based on a diffusion approximation solution discussed in Chapter. 3. In Paper **III** diffusion model is compared with MC based solution and an analytical solution. Many media (agricultural products, wood, food, plastic materials, paper, pharmaceutical products, etc.) have optical properties at visible and/or near-infrared wavelengths for which light propagation in the diffuse regime can be established, even in a few cubic centimeters of material. Therefore, the same techniques used to study biological tissues can be used in many practical applications to monitor industrial processes or for quality control [84–87] or in a completely different field.

---

[2]fractional change in flux during the time for a photon to traverse one transport mean free path, $l_t' = 1/(\mu_a + \mu_s')$

[3]negative sign in Fick's law means that diffusion current density(flux) is always in negative direction.

[4]also referred to as Green function

2.4.4 Limitations

Although the diffusion model is the most widely adapted analytical approximation, it has certain limitations. The first major breakdown of the approximation happens at close distances to the source where photons have not had yet enough time to undergo sufficient scattering events to be considered diffuse. This causes the diffusion model to deviate from the expected reflectance profiles based on MC simulations as shown in Figure 2.6. In such scenario, the estimation is no longer independent from phase function of scattering and has been reported often [88] along with proposed corrections [89, 90]. Anisotropic scattering is dominant in close proximity rendering diffusion ineffective in a forward problem.

Second source of diffusion break down is the high absorption relative to the scattering. This introduces another problem commonly referred to as "cross-talk". Cross-talk can be observed in the reverse problem where quantification of the performance of the model can be investigated for estimation of optical properties. Figure 2.7, shows the deduced optical properties both my MC and diffusion models for inverse problem. The systematic shift of properties for the diffusion model indicates coupling between the optical properties with the increase in absorption. This effect was also observed in Paper **II**.

Break down of the diffusion model is further addressed in Chapter 7 and Paper **III**.
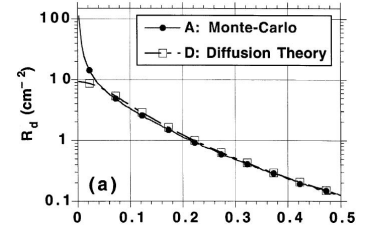
Figure 2.6. *Diffusion breakdown at close distance to source as reported by Wang et. al [88].*
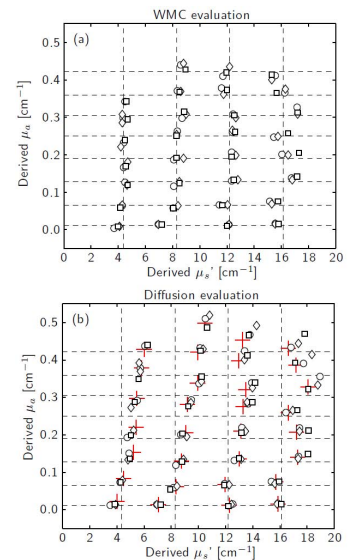
Figure 2.7. *Optical properties evaluated for inverse problem using MC simulations and diffusion model, presenting "cross-talk". Adapted from [72]*

A: OBLIQUE INCIDENCE REFLECTOMETRY (OIR)

Optical properties of turbid media are of a great interest whether the application is in the process design and manufacturing of food products or diagnostic therapeutic medicine in tissue [91]. These properties indicate changes in chemical composition and structural organization of the investigated sample. Moreover, they can help to quantify/estimate the macroscopic effects of a sample's molecular structure [92]. Diffuse optical spectroscopy (DOS) is widely applied to extract μ_a and μ_s' in the industries ranging from food analysis [93–96], pharmaceuticals [85, 86, 97, 98], biomedical diagnostics [99–103], medical treatment monitoring [104] and wood [105, 106]. As the light has possibility to non-invasively detect the changes in a medium, these properties have been of the major interest over last three decades [107–109].

Light propagation in homogeneous turbid media, like milk and yoghurt, based on diffusion theory, is determined by the sample geometry, refractive index of the environment n_o and already discussed (Ch: 2) four optical properties of the medium i.e., the refractive index n_i, the mean cosine of the scattering angle (or the asymmetry parameter) g, the absorption coefficient μ_a and the scattering coefficient μ_s. When the absorption and scattering spectra of the constituents forming the sample are well characterized, the concentrations of individual components may be calculated by measuring their optical properties with a broad spectral range. On the other hand, when the goal is to be able to distinguish between different structural compositions or forms of the similar samples, these optical properties assist by providing wavelength dependent feature development to help distinguish the subtle changes.

Measurement schemes, for optical properties in a diffuse medium, can be divided into three domains: continuous wave [110],

frequency-domain [111], and time-domain [112, 113]. While each domain has its own advantages, continuous wave is chosen for investigating the dairy products in Paper **I** and Paper **IV** for the reasons of requiring simple instrumentation and relative ease of handling. Paper **II** and Paper **III** used the time-domain technique described in Chapter 5.

When the goal is to estimate the optical properties of homogeneous turbid media, often the properties of interest are the absorption coefficient and the reduced scattering coefficient which can easily be extracted by analysing the diffuse reflectance profiles taken from samples under investigation. The scattering experienced by photons in a medium is influenced by the structural characteristics of the material, such as density, cellular structures and the interfaces between cells or more generally, by colloidal dispersions in the material. Static light scattering has been thoroughly investigated for dairy products by Skyyte et. al [114] in his thesis. Absorption, on the other hand, is related to the chemical constituents of the sample and hence can be used to probe the chemical properties of the investigated samples. Wavelength-dependent absorption is used to quantify the concentration of biologically important chromophores, such as haemoglobin, myoglobin, water, protein and for other more specific applications as well. Both empirical or semi empirical methods [115, 116] and analytical approaches [117, 118] can be used for extraction of these properties with different advantages. In this chapter we introduce a diffusion based model known as oblique incidence reflectometry (OIR) that was the topic of investigation in Paper **I** and Paper **IV**.

3.1 Theory and development

Farrell et. al [109] developed a diffusion based, two-source-point model and used that with normal incidence of light in which several points along the diffusion curve were taken to estimate the reduced scattering properties of a sample under test. The problem with the model was the need to have a close control over the power of the light source and the intensity of the light entering the sample. This method measured the total attenuation coefficient from the measured profile and to separate absorption and scattering from total attenuation measured by the model, proper intensity calibration was required. For in-line monitoring of dairy products, for instance, this could be problematic. To circumvent the requirement for an absolute intensity measurement in diffuse reflectance, Wang et al. [119] proposed the use of oblique incidence light to estimate the reduced scattering coefficient. Wang highlighted an additional advantage of oblique incidence, by using laser beam and a CCD, that the measurements are not affected by size of the laser beam, given the beam has mirror symmetry across major elliptical axis of
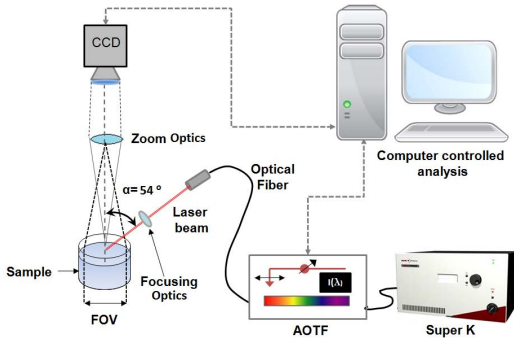
Figure 3.1: *Hyperspectral illumination system and setup for oblique incidence reflectometry. SuperK laser generates white collimated light which is tuned by AOTF for wavelength selection. Inclined laser light is projected on a sample to generate diffuse reflectance profile, captured by a CCD camera at normal incidence. Zoom optics used in front of CCD is chosen to increases the resolution but still not limiting the field of view (FOV) on the sample.(Figure not to scale)*

the spot on the surface of the sample [119]. With this development, the need of absolute intensity measurements was eliminated. The spatially resolved measurement of both the diffused light and the profile close to the entry point became much simpler and direct. Using the oblique incidence, spectral resolution was achieved by using white light [120]. Lin et al. [121] introduced absorption to the model and this approach has been used in Paper **I**. Figure 3.1 illustrates the instrumentation used for OIR. OIR has now become a recognized and established technique due to the advancements over the years which have helped in advancing the application of diffuse optical spectroscopy for clinical use [122–125]. Figure 3.2 illustrates the measurement scheme for OIR. The incident light on the surface of a sample is scattered and the intensity of the light gets reduced as it propagates away from the centre. This decay of intensity is shown with the color coding. The reason for a slower decay in the forward direction is the angular incidence of the light which produced a skewed shape. This happens because of the shift of the assumed point source buried in the sample as shown in Figure 3.3 The asymmetric shape enables the quantification of the light's mean free path in the sample presented as the centre line in Figure 3.2. This displacement is measured by the distance between the symmetry point of the reflectance profile through out the high(red) to low (blue) intensities. Paper **I** presents the details on how the measured displacement (Δx) can be used with effective attenuation by the low intensity light to estimate the required absorption and reduced scattering coefficients.
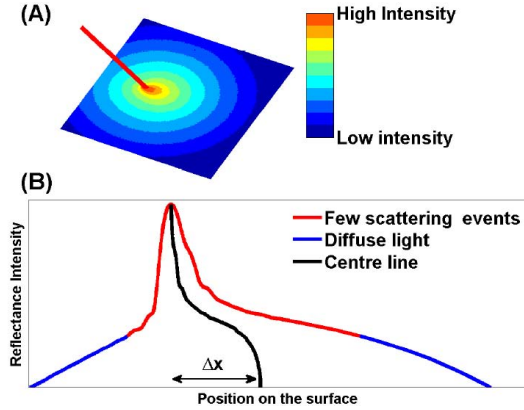
Figure 3.2: *Illustrations of OIR as given in Paper **I**. (A) A red light beam is obliquely incident on a sample surface. The surface is colour-code by the intensity of the diffuse reflectance. (B) Shows the reflectance intensity along a line though the entry point in the direction of incidence. The symmetry point of the reflectance profile shifts by a distance Δx between high and low intensity light.*
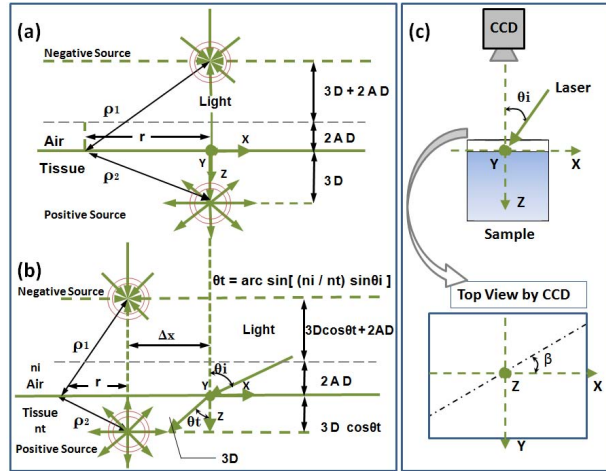
Figure 3.3: *(a) Positions of point sources in the diffusion theory model for normal incidence, (b) positions of point sources in the diffusion theory model for oblique incidence. The 'y' axis points off the page. $\rho 1$ and $\rho 2$ are the distances from the positive and the negative point sources, respectively, to the point of interest on the tissue surface at a radius 'r' from the axis of the sources. θ_t is determined from Snell's law. (c) Principle sketch of image acquisition and line extraction. θ_i is light angle with normal to the sample surface. β is formed with CCD axis.*

3.2   Constraints

It is essential to understand the scale at which the interactions take place. This is given by the length a photon has to travel before experiencing an interaction and is called transport mean free path length (mfp'). Based on Monte Carlo simulation [121], this length was defined as:

$$1mfp' = \frac{1}{0.35\mu a + \mu'_s} \qquad (3.1)$$

mfp' determines which optical properties are of interest at the present scale. Light is consid 1ered diffuse at least more than 2mfp' away from the point of entry. Which makes the diffusion models applicable away from the entry point only. High scattering media like yoghurt (3.5% fat) provide enough resistance in light path to make it diffuse at much smaller distances ($\sim 200\mu m$ at 470 nm) while in skimmed milk (0.5 % fat) this distance can be increased 10 folds ($\sim 2mm$ at 1020 nm).

Light behaviour is changed in diffuse regime and different combinations of two individual properties may lead to the same effect as presented in Figure 3.4, which is explained by similarity relation [126]. Similarity relation poses a challenge to separate μ_s and scattering phase function g, once the bulk property of μ'_s has been extracted from diffuse reflectance profile. This means the individual information of μ_s and g is lost after $\sim$2mfp' and light has no recollection of where it came from in terms of directionality. However, within the range of 2mfp', light still contains the information of it's scattering phase function. Another property of interest in close range is speckle which is the graininess observed on the image surface due to lights wave nature causing random interference [127, 128].

Figure 3.4. *Diffuse reflectance profiles on surface of a tissue, generated using MC simulations for two sets of scattering (μ_s) and anisotropy (g), keeping μ'_s constant, with normal incidence. Similarity relation gets challenged in OIR as reported in Paper **IV***

3.3   Choice of parameters

The diffusion model used in OIR was illustrated in Figure 3.3. When angle of incidence is changed from normal to the oblique, the photons travel in the medium the same distance (1mfp') before encountering any event but in the direction dictated by the refractive index mismatch (Snell's law). The displacement, Δx, length depends on how far the photons has travelled and at which angle. Therefore, the choice of appropriate incidence angle is rather important to ensure that sufficient displacement is produced for measurements. Another important factor affecting the light propagation under the angular incidence is the polarization. The light intensity becomes polarization dependent with oblique incidence. In order to get the maximum light intensity transmitted into the sample to have more number of photons for propagation, it is reasonable to choose S or P polarized light based on maximum

(a) Polarized light transmission.

(b) Caculated diffusion displacements for different scattering coefficients

Figure 3.5: *(a) Polarization effects on light transmission in a sample (n = 1.378 for milk and yoghurt) with oblique incidence and (b) length of displacement, ΔX, estimation based on angle of incidence. Vertical red line marks Brewster angle 54^0 for the total transmission for s-polarized light into the sample. An angle close to brewster window was used in Paper **I**. Absorption is neglected. Adapted from [129].*

transmission in the sample. Both these estimates are illustrated in Figure 3.5. Projected width of the beam in the sample is also presented as a function of incidence angle. It is desirable to have larger displacement than the beam width to ensure that estimation of the centreline (Figure 3.2) is distinct.

In Figure 3.5, maximum transmission of S-polarized light at Brewster window was observed. Therefore, the choice of incidence angle and polarized light for OIR measurements, 52^0 with S-polarized light, used in Paper **I** was rationalized and well supported. The selected wavelength of light delivered to the sample is polarized because of the AOTF used for wavelength selection. The state of the polarization can be changed by simply rotating the fiber delivery system around its symmetry axis. The polarization test presented in Section 4.2 gave the motivation for the improvement of the instrumentation as well as the technique used for acquiring the data. Therefore, the choice of the parameters for the instrumentation of OIR is directly influenced by refractive index as it affects choice of angle and polarization. The final choice of incidence angle in Paper **I** was motivated by the reasoning explained in this section.

3.4 Oblique MC validation

OIR has the advantage of simplicity because of the dependence of the optical properties on the shape of the measured profile and being a relatively cheap technique with the choice of a CCD that requires not too complicated instrumentation. Its accuracy is often tested in comparison to MC methods but yet has not been

analysed for its sensitivity in particular dynamic range of optical properties. It would be of interest to see how sensitive the method is to the small changes with a given setup and how to determine the requirements for appropriate setup. Paper **IV** is motivated by this idea to explore the sensitivity analysis of the technique and investigate the limits that might be imposed on the technique as well as the required instrumentation.

Figure 3.6 illustrates the MC implementation of oblique incidence used by Lin et. al. [121]. A simulated MC profile for set of optical properties is generated and fitted with the original OIR diffusion model. An accurate match between both can be seen for the distances away from the entry point. The expected skewness of the MC profile is because of the oblique incidence.

Figure 3.7 illustrates the effects on the oblique profiles due to change in the incidence angle while keeping the optical properties constant. An interesting observation is the light behaviour close to the entry point where the skewness of the profile is mainly altered. At larger distances, the profiles start becoming equally diffuse as in an isotropic medium. It is a good way to see the lose of knowledge of directionality by diffuse light.

To illustrate the variation in profiles experienced due to varying scattering properties of the media, Figure 3.8 presents the effects on expected OIR profiles with changing scattering properties. OIR's ability to use the change in the shape of profiles is what makes it superior to normal incidence case where absolute intensity is of interest. An important observation is the diminishing effect of g when scattering is overpowering. When scattering becomes relatively much larger than the anisotropy of the medium, the light can no longer propagate easily for longer displacements without encountering scattering events thereby taking away the skewness of the profile. This makes it extremely hard for any imaging system to measure the displacement produced thereby limiting the system's applicability, as investigated in Paper **IV**.

The illustrations from Oblique MC suggest some limitations that may get imposed on the instrument and also limit the OIR itself. Changing scattering values impose the requirements on imaging system. For very optically dilute media, light would pass without many scattering events covering most of the field of view (FOV) with skewed profile with not much left for diffusion model to work with. On the other hand, very high scattering media would squeeze the effect of skewness thus reducing the displacement distance. Similar change in profiles for the milk and yoghurt samples is also presented in Paper **I** and Paper **IV**. Both these issues require improvement in instrumentation if wide dynamic range of optical properties are to be measured. Higher resolution CCD cameras can help resolve the fine displacements while wide angle lenses would increase the FOV to cover larger sample area.

The inherent limit in OIR is the inability to monitor changes
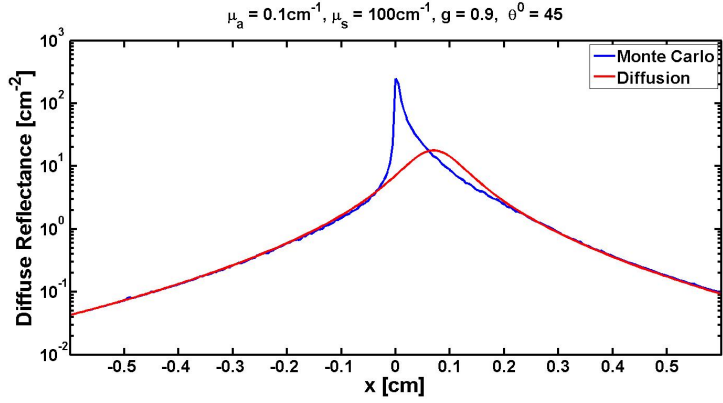
Figure 3.6: *MC and diffusion model simulation of OIR.*
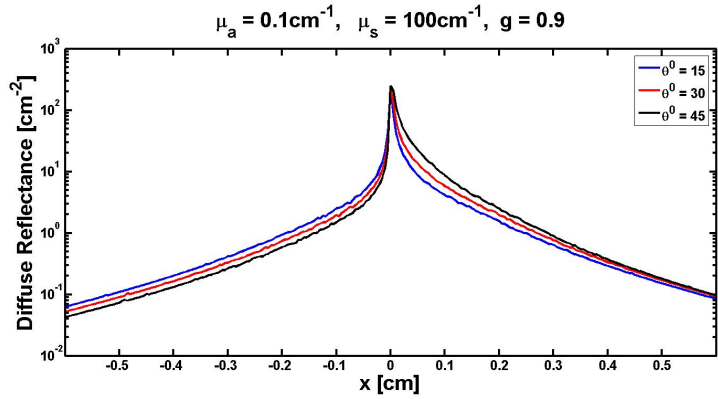
Figure 3.7: *Oblique MC simulations for varying incidence angle and effects on profiles.*
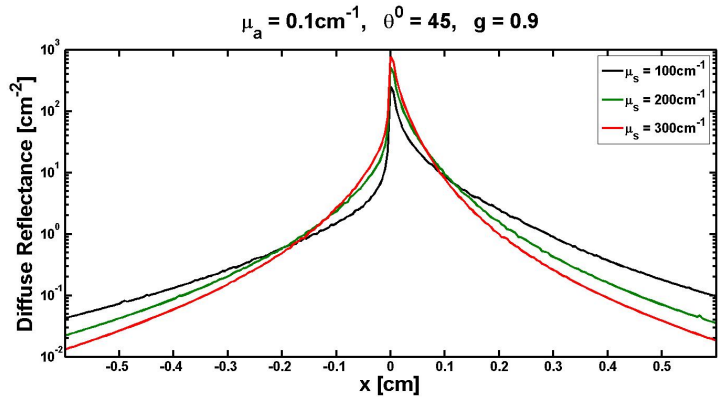
Figure 3.8: *Oblique MC simulations for varying scattering properties of the medium.*

in 'g'. Displacement is the only parameter required for the estimation of μ'_s which comes from mfp' but does not provide any estimation of anisotropy. That is why mfp' estimation is imperative as it quantifies the length scales on which the different optical interactions take place. Its specific dependency on both absorption and scattering asymmetry (g) has been the subject of various discussions [130, 131].

3.4.1 Conditions of use

To use oblique MC for sensitivity analysis, it needs to mimic the vision system in question. Which mainly is related to the optical magnification of the system to get the scale right, resolution of the sensor and the FOV. In simulations, this can easily be achieved by setting the MC bin size as a replacement to pixel size and the number of pixels to define FOV and resolution. We assume that amount of light entering the camera in the field of view is not of concern on the basis that intensity of profile is relative and can be scaled.

3.4.2 Sensitivity analysis

The idea of sensitivity analysis is to explore the OIR technique using MC simulations and determine the margins in which one can operate a measuring system and still expect to produce desirable as well as reliable results. A diffusion based technique which is analytically limiting may produce desirably distinguishable results but it is difficult to say with certainty about its ability to monitor subtle changes in a medium.

For example, during the milk fermentation process, bacteria produce acid and the pH value drops. This starts the process of acidification and structural changes begin to take place inside as the gel structures begin to form on microscopic scale. These can be termed as particles as well. Similarly change in the fat content would alter the optical properties of the medium as well. Although knowing the range of optical properties to be investigated is considered most relevant, it is equally important to know how much of a change in those quantities can be detected as well. In other words, how sensitive is the measurement system towards the changes happening in the medium of interest. Having the knowledge of such kind can help design the exact system with the required specifications instead of over spending in technology which was never needed or building the instrumentation which was never adequate to begin with.

The sensitivity analysis of OIR presented in Paper **IV** demonstrates, for example, in a particular dynamic range of optical properties, what are the margins of error a system has to operate in. This way it can be determined to what extent the expected optical

properties have to change before producing a detectable change in estimated/measured properties by the system. As OIR can not attribute a measured change to the anisotropy of the medium, the significance of the a priori knowledge of g for accurate estimation of optical properties is also highlighted.

For comparison and experimental verification, the vision system presented in Paper **I**, along with the milk samples is considered in Paper **IV**. Although, the presented OIR technique in the Paper **I** is modified and improved compared to the original technique by Lin et.al. [121], the diffusion model can be simulated for both cases in the same way using MC simulations. In Paper **IV**, Oblique MC based analysis presented the estimate and quantification of the percentage changes in optical properties measurable for the given vision system. More illustrations and examples are presented in Chapter 4.

B: OIR application and results

The investigation and analysis of OIR resulted in the improvement as well as modification of the technique to build new methods and then apply on the commercially available milk and yoghurt samples for testing purpose. In this chapter, the results are presented, with the original technique in our implementation, which served as the motivation to improve further on the methodology as presented in Paper **I**. Representation here is the part of the scientific development and contribution where previously proposed OIR method for CCD camera inspection was explored. The methods did not generalise well to the given measurements of the dairy samples thereby requiring certain improvements added to the original method for data acquisition and improved precision. Also, the sensitivity analysis conducted on OIR is discussed which is presented in Paper **IV**.

4.1 Dynamic range of optical properties

One of the major interests, when applying a new technique or instrument, is to know the dynamic range in which it operates. For this thesis work, the OIR technique was adapted and a vision system was built to implement the technique. To find out the working limits of the system, a carefully controlled measurement campaign with intralipid 20% phantom series, covering a broad range of optical properties, was conducted for the application and analysis of OIR to estimate the wavelength dependent reduced scattering. To validate the measurements, expected scattering properties based on Lorenz-Mie theory were calculated as presented by Frisvad et al. [132]. Results are summed up in Figure 4.1. The legend represents the amount of intralipid present in the solution as weight percentage. Increase in the intralipid means the increase in reduced scattering coefficient of the sample. The solid curves indicate the dynamic range measurable by the vision
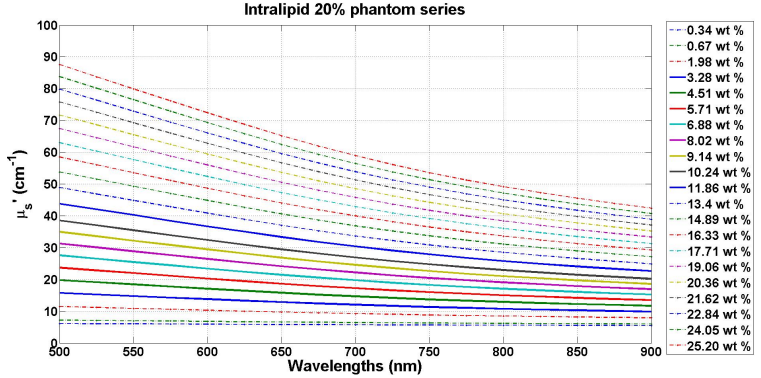
Figure 4.1: *Predicted wavelength dependent optical properties of intralipid 20% solutions series using Lorenz-Mie theory. Extended dynamic range of investigated optical properties is shown. Legend presents the wt% of intralipid in water solution. Solid lines indicate the dynamic range for which original OIR technique with previous instrumentation worked. Calculations modified from the code by Frisvad. [133]*

system from the measurement campaign. It is important to note, however, that Frisvad's calculations required an offset to be added to match the measurements. Dashed curves in Figure 4.1 indicate the optical properties not reliably measurable because they were out of the measurement range of the instrument and method. Small step size between intralipid concentrations was chosen to see if the applied technique can detect the small changes with in the measurable range of optical properties.

From the results of the measurement campaign, the limitations of the system were revealed. The results suggested that the system did not have enough resolution power to be able to resolve the structural changes in meaningful way above the range of solid curves indicating μ_s' in the range ~ 45 cm^{-1}. Also, because of the limited field of view (FOV), the system couldn't capture enough diffusion profile for OIR with scattering values lower than ~ 15 cm^{-1}. The knowledge indicated the need to change the camera and imaging objective to increase the FOV, while retaining a high spatial resolution. This enabled milk fermentation process to be characterized, which exhibits a broader dynamic range of optical properties, as presented in Paper **I**.

4.2 Original OIR vs Previous reported results

After intralipid series, a measurement campaign was conducted on commercially available milk samples to understand the dynamic
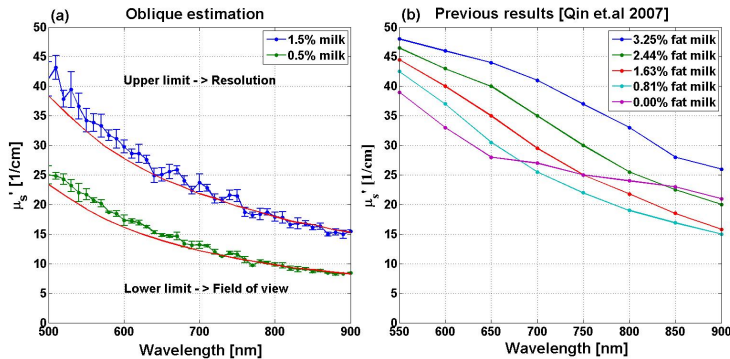
Figure 4.2: *(a) Estimated μ'_s as a function of λ with original oblique incidence reflectometry, for 1.5% and 0.5% fat milk and compared with analytical model [132] based on Lorenz-Mie theory and also with previously presented (adapted from [117]) results (b)*

range of their optical properties. Figures 4.2 presents the results that could be quantified in the already established dynamic range. Only 0.5% fat milk and 1.5% fat milk could be characterized. Products below or above revealed non-physical behaviour for the estimated curves indicating system limitations. Comparing the measured properties with predicted curves based in Lorenz-Mie theory shows that measured properties are well represented. In comparison to the only reported properties by then, our implementation produced the first physically meaningful properties for milk. However, the slight deviation of measurements from the expected curves can be observed which can be attributed to the possible cross-talk.

From the image analysis of the captured diffuse profiles, the overshooting of the entry point estimation along the line of incidence was observed. This study motivated the development of a new method to estimate the entry point which avoids the problem. Also, along with the overshooting issue of the light entry point, the estimation of the diffusion center was uncertain because the original method used the average pixel size. For the estimation of the diffusion centre, a method was proposed which made better use of the CCD chip by only using a single line along the diagonal for the estimation. To improve further, not only image distortion for point illuminations was quantified by a new method but also the new approach added both wavelength dependence and quantification of lens aberrations in identifying pixels on CCD as presented in Paper **I**.

Polarization effects were also investigated for an intralipid phantom solution. Figure 4.3 sums up the findings from the investigation. The experiment was setup by placing a glass plate on
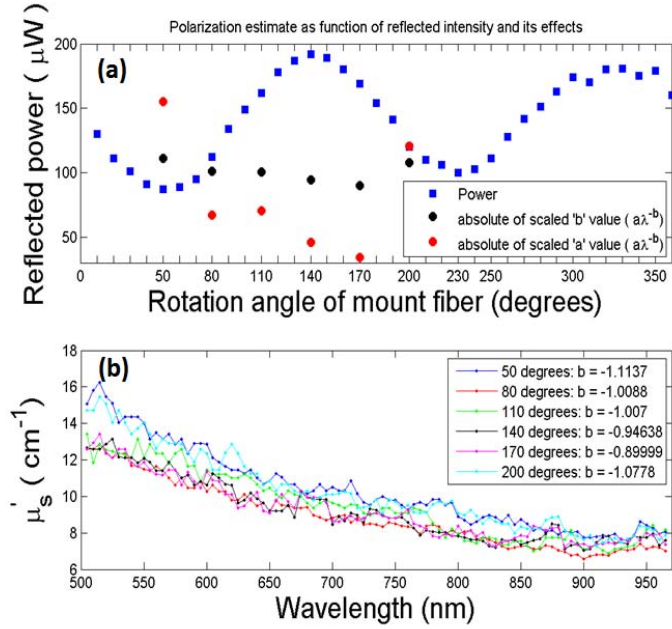
Figure 4.3: *(a) Reflected light intensity from the surface as a function of rotation angle of fiber delivery system. Red and black dots represent scaled slope and amplitude of power law $(a\lambda^{-b})$ fit to the scattering measurements on six rotaional angles. (b) OIR measured scattering properties.*

top of a sample that would reflect some of the light depending on the light polarization in the incident plane. Reflected light is collected by a photo-diode. S-polarized light will produce minimum reflection, if any, at Brewster angle as most of the light will get transmitted to the sample. By changing the rotational angle of fiber in small steps reflection intensity profile is generated. The optical properties are measured at 6 angles between 180^0 rotation of the polarization and are shown in Figure 4.3(b). We observed that for the Brewster angle (around $\sim 50^0$), the maximum transmission was achieved and the measured μ_s' profiles for both angles, close to the minimum reflection, yielded similar scattering curves in amplitude and slope. Measurements were fitted with power law (Equation 2.6) to get the slope and amplitude parameters which were plotted as points on Figure 4.3(a) for comparison to angular dependence and polarization. However, the significance of this test was the proof of the presence of polarization effects.

These studies paved the way for not only the identification of the major issues with OIR implementation but helped with the improvements done to the technique. The resulted OIR implemen-

tation was used for the discrimination of the structural properties during fermentation process which yielded excellent results. Paper **I** presented clear distinction between not only the products with different fat contents but also different structures of milk and yoghurt when the fat content was same.

4.3   Sensitivity analysis

As the goal with milk and yoghurt analysis was to be able to discriminate between structural differences and various fat levels, the interest was not focused on the quantification of the accuracy of the optical properties measured. As any model used for validation will have model based variations introduced, there is no gold standard to compare the results with. Same products measured with a different methodology and instrument may produce varying results. However, the ability to resolve the changes happening in structure of milk or yoghurt is dependent upon the sensitivity of instrument, as well as the technique itself. Therefore, it becomes rather of importance to investigate the limitations of the technique as well the working limits on the imaging system in terms of resolution and FOV. We used 3D Monte Carlo code [73] to simulate the oblique incidence reflectometry to explore the sensitivity of the current system based on the measurements from Paper **I**. This made a scientific contribution towards quantification of the relative measurable change related to dynamic range of the optical properties. The summation of these results are presented in Paper **IV** with comparison to the measurements performed in Paper **I**. The results are summarised in the manuscript but some consideration for the analysis are presented below.

4.3.1   Parameters and Scales of relevance

The two point source model presented in Chapter 3 and Paper **I** assume that the diffusion coefficient is related to the displacement of the source point inside the medium [121] by:

$$D = \frac{n_{med}\Delta x}{3Sin\theta_i} \tag{4.1}$$

where θ_i is the incident angle and n_{med} is refractive index of the medium. In the case of milk, the assumed refractive index is, $n_{milk} = 1.347$ [134].

Δx is the displacement which depends upon the optical properties of milk. The relation comes from Equation (3.1) which is linked to diffusion coefficient as:

$$3D = 1mfp' = \frac{1}{0.35\mu_a + \mu_s'} \tag{4.2}$$
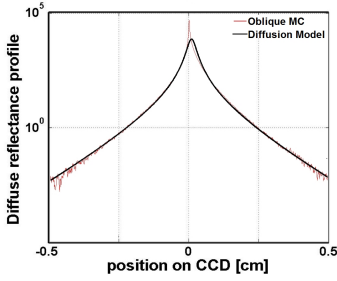
Figure 4.4. *Oblique Monte Carlo simulated diffuse reflectance profile with $\mu_s' = 40\ cm^{-1}$, $\mu_a = 0.1\ cm^{-1}$ and $\theta_i^0 = 52$.*
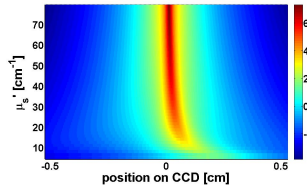
Figure 4.5. *A simulated spectrograph of diffuse reflectance profiles for OIR with μ_s' changing from 5 to 80 cm^{-1}. $g = 0.7$ and $\mu_a = 0.02$. The displacement on CCD is shown by movement of the profile center as a shift.*
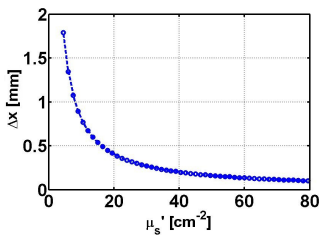
Figure 4.6. *Displacement as a function of reduced scattering for the extended dynamic range in Paper **I**.*

In Paper **I** we have reported the dynamic range of measured optical properties which were also independently verified [135]. μ_s' varies from ~5 to ~80 cm^{-1} while absorption is low by the ratio of over (1 x 20). Therefore, we can directly link μ_s' to the estimation of Δx. These changing properties give rise to the varying optical path lengths (mean free paths) thereby changing the diffuse reflectance profiles. For detection of these changes, CCD camera used had resolution of 8 mega pixel with final 3.2μm pixel size on the image surface.

4.3.2 Results

Oblique Monte Carlo may provide an optimal numerical validation for any method based on radiative transfer. Figure 4.4 shows an example of simulation generated profile based on MC and OIR model. The optical properties presented reflect the mid way range of milk and yoghurt.

In Figure 4.5, the drift of the diffusion center caused as an effect of changing optical properties is presented. It is clear that the higher scattering produced very small Δx with well defined scattered profiles as the light got diffuse. The decrease in scattering reduced the intensity of the profile and produced larger displacements as light travels further without encountering scattering thereby not producing enough diffuse profile region on CCD. This figure illustrates the two requirements for the imaging system: high resolution to resolve very small displacements and wider FOV for spanning low scattering profiles.

The change produced in the displacement due to varying optical properties in the dynamic range is, however, relative. The requirements on ability to resolves a change depends on the range of scattering as shown in Figure 4.6. Here, displacement as a function of reduced scattering coefficient is presented. The range of Δx is from 102 μm to 1.79 mm from high to low scattering respectively. μ_s' was varied in steps of 1.5 cm^{-1} which corresponds to 30% change in lowest scattering to 1.9 % change in highest scattering.

With the varying percentage change in the optical properties the resolution requirements also differ through out the dynamic range. Figure 4.7 sums up the resolution requirements to capture the change ($\mu_s' = 1.5$ cm^{-1}) introduced in scattering. Current system resolution appears as red dashed line. It shows that the system, theoretically, suffices the need of resolution for all milk products as well as yoghurt 3.5% fat for higher spectral range at least. After that displacements produced are less than a pixel. However, this does not reflect the real time limits which are discussed in next section.

4.3.3   Discussion

The results presented above with MC simulations for oblique incidence and estimation of resolution requirements were for the best case scenario. Wavelength dependence of μ_s' was not shown here because that dependence indicated a single sample representing a select region of the extended dynamic range only. However, the analysis here holds the same value for the changing reduced scattering through out the full dynamic range.

The most significant aspect is the resolution requirement of the system. Theoretically, OIR technique has no limit on the resolution and is capable of determining the optical properties in any range as well as the relative change in those properties. However, the method is in itself limiting with the definition of it's application in diffuse region. For OIR, the diffusion of light is mandatory before its application. Therefore, it is impossible to get the anisotropy factor of the medium directly because by the inverse problem solving, from Δx estimation, only μ_s' can be retrieved. Thereby any changes introduced in the measurements caused by g affect are lost and can not be modelled.

The value of $g = 0.7$ assumed in MC simulations was not accurate for milk and yoghurt as the g values form 0.93 for low fat milk with blue light to 0.68 for whole milk have been reported in the literature [136]. The measurements on milk and yoghurt in Paper **I** were affected by both cross-talk (Section 2.4.4) and the effect of g. Given the very low absorption present in the samples generally, the cross-talk was mainly visible for very high water absorption peaks as it increased the error in the estimation of μ_s'. g on the other hand was not quantified or addressed in OIR so it might be limiting the accuracy more. The anisotropy has a wavelength dependence of interest [71]. Wang et. al [88] also reported this problem for the method and we have addressed the contribution of g in Paper **IV**. In summation, it was important to include the anisotropy estimation in the measurements to improve upon the accuracy of the method. This would require the adaptation of the technique as presented in time-domain diffusion measurements [137, 138].

Second important factor limiting the precision of the measurements was the nature of the reflectance profiles captured by CCD. Diffusion based models stemmed from the photon nature of the light that is why they capture only the discrete effects like scattering and absorption. However, a high resolution CCD camera can capture a full, high dynamic range image of a sample surface that tells a much larger story of the other optical phenomena taking place on the surface as well. One major source of error in precision came from inaccurate estimation of the light entry point. Wave nature of the light produces interference patterns all over the surface giving rise to "speckle" which made it hard to quantify
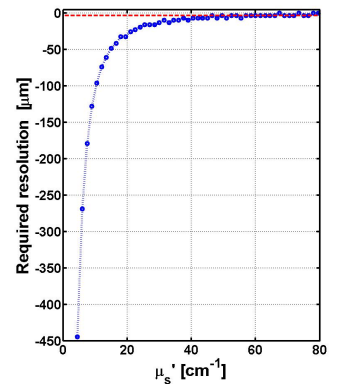
Figure 4.7. *Required resolution to detect a change of 1.5 cm^{-1} in μ_s' at different dynamic ranges of scattering. Red horizontal line marks the the 3.2 μm pixel size currently used.*

the exact point of entry. This uncertainty in the measurement of the entry point was a source of error in th estimation of optical properties as well.

In current system, the center perturbations were spread over $\sim$ 20-30 pixels giving a range between $\sim$ 60 to 100 μm for the estimation. In Figure 4.7, the reduced scattering properties below $\sim$ 15 cm^{-1} to $\sim$ 20 cm^{-1} fall outside this limit. These simulations validate the findings in Paper **I** where we observe high precision for the optical properties below $\sim$ 20 cm^{-1}. Further increase in μ_s' appears to increase the error bar as the uncertainty of the estimate becomes higher. From these results we concluded that even if the resolution of the CCD is quite high the effective resolution is limited by intensity profile of the center of the image.

Therefore, to increase the precision of the measurement technique, it is essential to incorporate both the wavelength dependence of g and methods to accurately quantify the entry point of the light.

PHOTON TIME-OF-FLIGHT SPECTROSCOPY

Visual inspection methods like OIR can provide an adequate validation and interpretation of the models depending on the purpose they are used for. But quantifying the accuracy of such models for estimation of the optical properties requires inverse problem solving. MC has been the golden standard to validate the accuracy of the measurement techniques used to extract the optical properties of the turbid media. Photon-time-of flight(PTOF) spectroscopy or PTOFS works on the principle of inverse problem solving, using MC data bases for such experimental validation. The optical properties of dairy products investigated using OIR, as explained in Chapter 3 & 4, presented in Paper **I** have also been studied using PTOFS [135]. This chapter introduces this non-destructive, rapidly evolving, time-domain spectroscopic technique and its applications which lead to the publication of Paper **II** and Paper **III**.

Figure 5.1. *Illustration of temporal pulse broadening due to light propagation through a scattering medium. On left, in random walk illustration, some photons take shorter path and reach early to the detector while others take longer and reach later. The narrow incident pulse thus spreads out because of different paths of photons and gets broadened in time as shown on right. Modified from [139].*

5.1 PTOFS Theory

The measurement principle for PTOF spectroscopy is illustrated in Figure 5.1. A light pulse of short temporal width is introduced into the sample, collected at the other end and the PTOF distribution is measured. While in the medium, photons can propagate in any direction after encountering a scattering event. This random path selection process makes some of the photons experience less scattering events thus arriving earlier than others. Because of the different propagation times, the temporal width of the emerging PTOF distribution is broadened.

By analysing the photon distribution collected over time, two distinct optical properties can be estimated from PTOFS: absorption (μ_a) and reduced scattering (μ_s'). The shape of the temporal

Figure 5.2. *Normalized fluence as solution to the diffusion equation for a semi-infinite medium in PTOFS [141]. Refractive index used is 1.55 (intralipid optical phantom) with fiber separation of 10mm. Absorption was kept constant at 0.1 cm^{-1}*
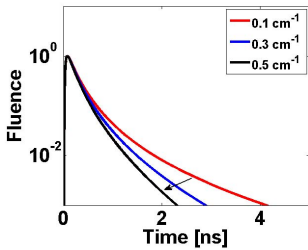
Figure 5.3. *Normalized fluence as solution to the diffusion equation for a semi-infinite medium in PTOFS [141]. Refractive index used is 1.55 (intralipid optical phantom) with fiber separation of 10mm. Scattering was kept constant at 5 cm^{-1}*

distribution of the broadened light pulse is used to deduce these optical properties. An illustration of time distribution profiles and their effects on estimated optical properties is presented in Figure 5.2, for constant μ_a, and Figure 5.3, for constant μ_s'. These properties have visibly different effects on the time-domain profiles as can be observed. Broadening of profiles and delay in the arrival of photons indicate high scattering medium. In contrast, higher absorption is indicated by contraction of the profiles. This highlights a distinct feature of PTOFS that for diffuse light, shape of the distribution profile can directly provide an estimate of optical properties. The geometry of the medium does not effect the way optical properties influence the profile. In Paper **II**, PTOFS was used to carry out measurement campaign on pharmaceutical tablets as samples mimicking a slab geometry. The source fiber delivered the laser pulse on one side of the tablet while the detection fiber collected the transmitted photons on the other side of the tablet. The tablets represent a highly diffuse medium measured also in close near-infrared range thus the detector used in that scheme was a phtonmultiplier tube (PMT) as previously used [140] to achieve high temporal resolution. In Paper **III**, the source and detection fibers were submerged inside the liquid optical phantoms. Relatively, they were optically dilute samples and measured only in the visible spectral regime therefore in this scheme, an avalanche photodiode (APD) was used as a detector.

5.2   Instrument Setup

Figure 5.4 illustrates the schematics of PTOF spectroscopic setup which is the result of development presented in several doctoral thesis [139, 141, 142]. Paper **II** and Paper **III** both used the same setup with the choice of appropriate sample and detector.

The light generated by supercontinuum source is filtered using an effective tunable acousto-optical filter (AOTF) that selects a narrow temporal width of the light profile. A small portion of beam is split which acts as a timing reference (TR) and the rest is sent to the sample. TR is used to compensate for temporal drift which enhances the measurement precision [143].

The light pulse passing through the sample gets broadened. To estimate the instrument response function (IRF), a thin double black side paper is inserted instead of the sample. The timing reference sample and IRF remains narrow. Before collection at the detector, both pulses are combined again. The fibre length for the TR signal is adjusted so it arrives $\sim$ 2 ns earlier at the NIR detector than the signal from the sample. To avoid over saturating the detector by keeping a low photon count all the time, both beam arms are fitted with attenuators to control the amount of light passing through. The photons are converted into elec-

trical charges producing current which is used by TCSPC (time-correlated-single-photon-counting) card (SPC-130, Becker & Hickl, Berlin, Germany) and converted into digital signal. Details of the process are provided in Hand book by Becker [144]. The choice of photon count rate used can have systematic effects on the shape of the signal as well which has been thoroughly investigated [145].
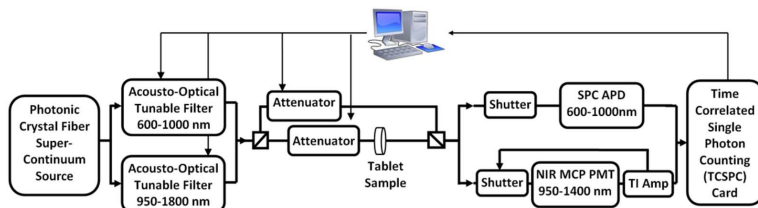
Figure 5.4: *Schematic of the PTOF spectrometer; APD: avalanche photodiode, MCP: micro-channel palate, PMT: photomultiplier tube, TI Amp: trans-impedance amplifier.*

5.3 Application in pharmaceuticals

Generally, PTOF spectroscopy is applied vastly in areas of diffuse optical spectroscopy (DOS). Pharmaceuticals are an example of highly diffuse media. Because of their tightly packed structure, they have highly scattering behaviour i.e., in the range of $200cm^{-1}$ - $600cm^{-1}$. Near-infrared (NIR) spectroscopy (see 5.3.1) is the industry standard technique often utilized to analyse pharmaceuticals. NIR spectroscopic data provides underlying undesired scattering signal with the absorption spectra which often is corrected before any utilization of the data. However, this has also been used to extract information about the physical state of the samples [89, 146]. PTOFS, in contrast, provides separate independent scattering signal for physical parameter extraction which is an added advantage to absorption information and is considered a valuable tool in pharmaceutical analysis [147]. Svensson et. al [140] applied PTOFS on pharmaceuticals upto 1400 nm. In visible spectral regime, light is not absorbed immensely and therefore the most of spectroscopic applications using visible regime are based on evaluation of the scattering properties. For pharmaceuticals and other turbid media where not only structural but chemicals information is of the interest, NIR spectral regime is often used because of the strong absorption signatures or chemicals in this range. PTOFS has an advantage in NIR spectral regime of being able to not only provide information about the chemical compositions with absorption properties but also the structural information with reduced scattering properties. Abrahamsson et. al [148] improved

the quantitative analysis of intact tablets and build new diffusion based model for evaluation for PTOFS. PTOFS has shown the potential to provide an alternative to the conventional NIR spectroscopy. With the progress and advancement of the technique, it not only promises the additional information on structural properties but also the robustness of the quantification models used for predicting drug concentrations in the tablets. Time-resolved spectroscopy has been shown to link the physical parameters like compression force, particle size and density distribution to the measured optical properties [2, 5, 143, 149] in the case of pharmaceuticals. However, the technique has also been used for biomedical applications [150, 151] extensively.

5.3.1 NIR spectroscopy

Near-infrared spectroscopy (NIRS) has, over the last decades, evolved into an important tool in the analysis of pharmaceutical preparations and is a topic of several reviews [84, 86, 98]. Instruments for diffuse optical spectroscopy in time-domain [143, 147], frequency domain [152–155], and spatially resolved steady state [156] have been explored: all of them relying on the isotropic diffusion theory for data evaluation.
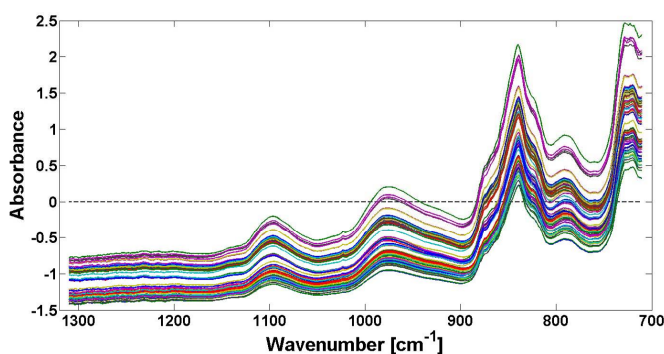
Figure 5.5: *Absorbance spectra of 75 pharmaceutical tablets, measured with NIR spectroscopy, used in Paper* **II**

Absorbance spectra of 75 tablets used in Paper **II** for comparative analysis are presented in Figure 5.5. The observed slope and offset in the spectra is caused due to underlying scattering signal in NIR measurements which requires often some pretreat-

ment for correction. NIRS is used in pharmaceutical industry in both quantitative [155, 157] and qualitative applications [158, 159]. Microstructure is an important parameter in pharmaceutical manufacturing of durable and reliable tablets [86]. A major draw back reported with NIRS for the quantitative measurements is the sensitivity of the methods towards the variations to the raw materials in the tablets of different batches [160]. Application of the various pretreatments even does not ensure that calibration models will work on different sample sets. This sensitivity is a challenge for the robustness of the technique. The variations in the optical path lengths in the investigated samples, either due to the change in the geometry or the microstructure, are a challenge to surpass for NIRS. In Paper **II** we show that this challenge may be eliminated using PTOFS by making more robust models independent of raw material variations [2].

MULTIVARIATE DATA ANALYSIS

This chapter explains the multivariate data analysis used to analyse data from the pharmaceutical tablets, acquired using photon time-of-flight spectroscopy (PTOFS), as presented in Paper **II**. PTOFS was used in a comparative study with near-infrared (NIR) spectroscopy for the analysis of pharmaceuticals. The tablet set was provided by AstraZeneca R&D [161] which was part of a large data manufacturing campaign. Tablets were made out of three ingredients: drug (Ibuprofen), filler (Mannitol) and a lubricant (Magnessium stearate). The tablets were manufactured with variations of drug concentration, also called as active pharmaceutical ingredient (API), drug particle size, filler particle size and the compression force with which the tablets were pressed. API concentrations in these samples were measured using Raman spectroscopy and served as the reference or ground truth concentrations of tablets as a comparative study for two techniques was formulated. The design of the experiment is presented in Figure 6.1. Additionally, spectra for all the tablets measured using NIR spectroscopy, was also provided for comparative analysis, which is a well established technique for analytical chemistry as well as various other fields of science and technology including pharmaceuticals [84, 86, 162]. The broad range of pharmaceutical applications of NIR spectroscopy are summarized by Bogomolov et.al [163].

6.1 PCA

For the data compression and information extraction, Principal Components Analysis (PCA) [164] which provides the most compact orthogonal description of the data, was used. We used PCA for exploratory purpose on the absorption data obtained using PTOFS. Data was preprocessed by mean centring and standard

Exp. number	Tablet Code	API Conc. (%w/w)	Filler Particle size d_{10} (µm)	API Particle size d_{50} (µm)	CF 1 (kN)	CF 2 (kN)	CF 3 (kN)
1	N1	16	91	50	12	14	16
2	N2	16	91	150	12	14	16
3	N3	16	450	50	12	14	16
4	N4	16	450	150	12	14	16
5	N5	18	91	50	12	14	16
6	N6	18	91	150	12	14	16
7	N7	18	450	50	12	14	16
8	N8	18	450	150	12	14	16
9	N9	20	91	50	12	14	16
10	N 10	20	91	150	12	14	16
11	N 11	20	450	50	12	14	16
12	N 12	20	450	150	12	14	16
13	N 13	22	91	50	12	14	16
14	N 14	22	91	150	12	14	16
15	N 15	22	450	50	12	14	16
16	N 16	22	450	150	12	14	16
17	N 17	24	91	50	12	14	16
18	N 18	24	91	150	12	14	16
19	N 19	24	450	50	12	14	16
20	N 20	24	450	150	12	14	16
21	N 21	20	211	100	12	14	16
22	N 22	20	211	100	12	14	16
23	N 23	20	211	100	12	14	16

Figure 6.1: *Factorial Design of experiment presented for manufacturing of tablets with three variables: API concentration, Filler particle size and API particle size. CF: Compression force.*

normal variate (SNV) [165, 166]. The purpose and reasons for the choice of pretreatment are discussed in Section 6.4.

When using PCA on mean centered data, eigenvalues can be interpreted as variance captured by each principle component. As the components in PCA are sorted according to the variance explained by each component, eigenvalues decrease monotonically with the increasing number of principle components. The ratio between consecutive eigenvalues, however, does not. Eigenvalues and eigenvalue ratio for first 20 investigated principle components (PCs) are presented in Figure 6.2.

In Figure 6.2, a slow increase in eigenvalues can be observed with the decreasing number of PCs until 5th PC. At 5th PC, the eigenvalue increase to reach 4th PC is relatively higher. The difference can be visualized in eigenvalues ratio more prominently. This indication is called "Knee" and suggests that 4 PCs may suffice to

explore this data set.

PCA is used to identify the outliers, if any, in the data set. Outliers can be found by looking at Q residuals, Hoteling T^2 and scatter plots of data on PC axis. Q residual is the measure of difference between a sample and its projection into the hyper plane created by PCA with given number of components. Hotelling T^2 is the measure of variation in each sample within the PCA hyper plane. T^2 helps to determine the samples/points with high leverage that can influence the PCs.

Figure 6.3, presents the Q residuals, T^2 values and loadings for first 4 PCs against variables (wavelengths), respectively. Variables above 1350nm have very high Q residuals and T^2 values. This may be due to contribution of cross-talk between optical properties. Loading of PC1 indicate that highest weights are given to the wavelength region above 1350nm which corresponds to high cross-talk region between scattering and absorption(Paper **II**). Also there is a small region close to 1200nm which exhibits cross-talk. Loadings for PCs 3 and 4 also seem to cover the variance caused by the same variables. This suggested removal of wavelengths outside 950 nm - 1350 nm interval used in Paper **II**.

After reducing the variables (950nm - 1350nm) and using PCA again, two components were able to explain much of the variance in the data with major variance explained across API concentration by PC1. PC2 separates the data based on filler particle size (FPS). Scores plot of PCA on first 2 PCs in Figure 6.4 suggested that in absorption spectra, major variance is caused by filler particle size. Figure 6.4 shows that almost all the measured tablet samples lay within the confidence interval with the exception of one outlier. This outlier sample belonged to the API concentration level 16. In current data set, as all the samples are different, any data point outside the confidence interval or laying alone may just as well be due to the fact that the composition of the tablet gave rise to a different optical property.

Ideally, the absorption spectra from PTOFS should be free of any contribution from particle sizes as PTOFS separately provides reduced scattering coefficient, responsible for representation of structural properties of the sample. However, the variance picked up by PC 2 of PCA suggests non-isolated absorption spectra. This is the evidence of cross-talk.

To investigate the contribution of variables towards the filler particle size influence on absorption spectra, loadings of PC1, Figure 6.5(top-left) and PC2, Figure 6.5(bottom-left) are plotted against variables. Figure 6.5(right) also shows scatter plot for variables on two PC axis. The scatter plot shows the groups of variables enclosed in different colour boxes. Contributions from each of these groups can then be cross referenced to PC1 and PC2 loadings. The variables enclosed in red, black and green rectangles are of high importance for PC1 loading. Yellow and blue regions
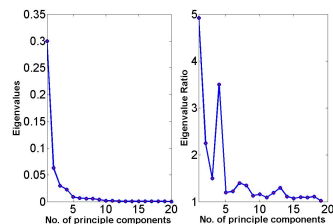
Figure 6.2. *(Left) Eigenvalues and (Right) Eigenvalues ratio for first 20 principle components.*
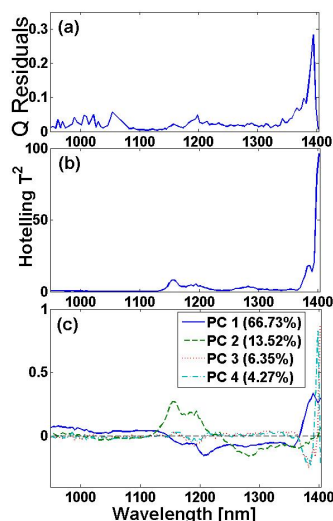
Figure 6.3. *(a)Q residual, (b) T^2 values and (c) loadings for first 4 principle components on all wavelengths.*
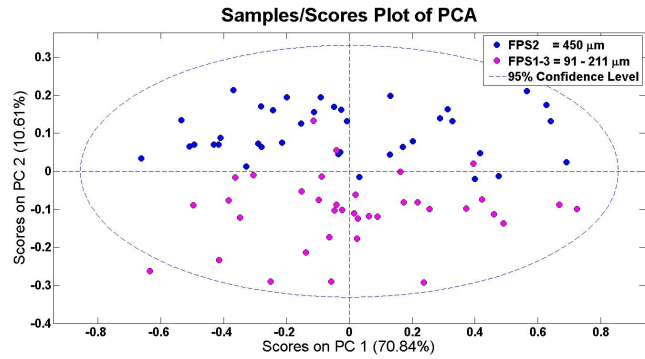
Figure 6.4: *PCA scores plot on PC 1 and 2. Blue dots are samples with filler particle size (FPS) 450μm. Magenta dots represent FPS1(91μm) and FPS3(211μm).*
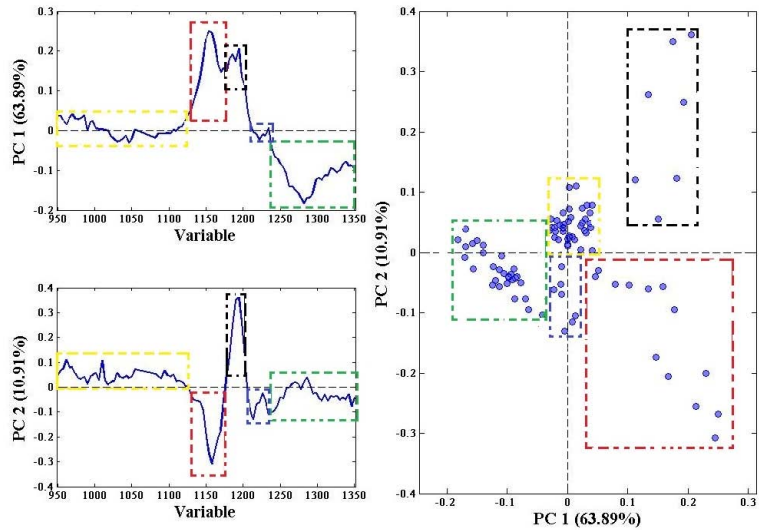
Figure 6.5: *(top-left)Loading of PC 1 and (bottom-left) PC 2. (right)Scatter plot of variables (wavelengths) on PC 1 and PC 2.*

do not have much weight so these wavelength regions do not contribute to PC1 significantly. For PC1 loading, peak in the red box corresponds to the absorption peak of ibuprofen (API) (Paper **II**). The variables in the green box correspond to a small absorption peak between 1250nm and 1300nm for filler (mannitol). PC2 , on the other hand, still shows cross-talk between absorption and scattering as an absorption peak corresponding to the filler is covered by it. PC 2 loading also explains some variance at ibuprofin peak (red box) but additionally, it explains variance close to 1200nm where cross-talk can be observed between scattering and absorption easily because ibuprofen and filler share an absorption peak at that wavelength (1200nm) (Figure 2.4). Also, for both loadings, variables indicated in yellow box appear to be noisy and with no significant weights either. By comparing this result to the Q residual in Figure 6.3, a similar uncorrelated response of the variables before 1050nm can be seen. Ideally, the variable response is expected to be smooth when spectral resolution is high because the absorbance at nearby wavelengths is co-related. Therefore, the first few PCs normally produce a "smooth" response or group the variables sensibly. The variables in yellow box in the Figure 6.5, however, indicate a non physical response for Q residuals: descriptive of noisy variables in the data. That also corresponds to observation that absorption spectra on these wavelengths was very low and noisy. From this analysis, we can conclude that PCA model can be improved by removing these variables as well which resulted with the the choice of wavelength region in Paper **II** for comparative analysis.

From PCA scores plot of Figure 6.4, only one outlier was identified. To decide whether to include or exclude the sample from the analysis, the sample is further investigated. Figure 6.6, shows the T^2 analysis of outlier presenting the contribution from all the variable. The large T^2 values for this sample mainly come from the wavelengths 1185nm - 1202nm (Figure 6.3) as we expected from loading plots as well. This proved that sample outside the confidence interval is not actually an outlier but the result of the possible cross-talk added by the wavelengths between 1185nm - 1202nm.

PCA analysis helped to identify the wavelengths, 1350nm - 1402nm, that were influenced by the cross-talk between absorption and scattering. by removing those wavelengths, we could reduce the number of PCs required to explain the major variance in the data based on API concentration. However, as these wavelengths represent cross-talk, not noise, they might also have the potential to add information towards predictions. Figure 6.7 presents the spectra from both transmission NIR spectroscopy and PTOFS as well as the selected spectral range.

An important point to note is that the factorial design of the experiment inherently introduced sparseness with large number of
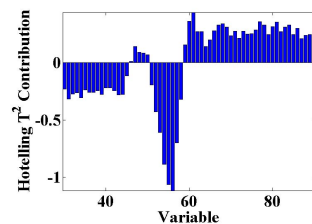
Figure 6.6. *Hotelling T^2 vs variables for outlier sample tablet*
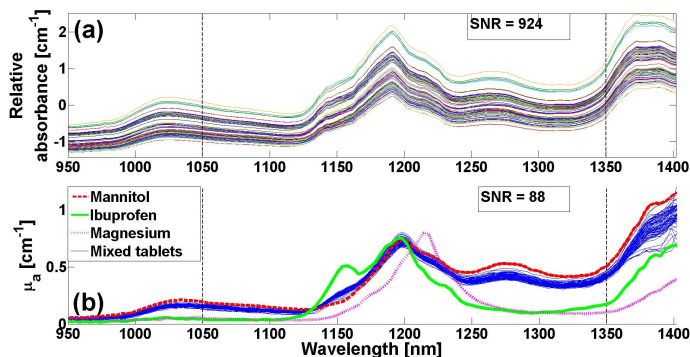
Figure 6.7: *(a) Absorbance spectra of all the sample tablets from transmission NIR spectroscopy and (b) PTOFS absorption spectra including the pure ingredients. SNR = signal to noise ratio and vertical dashed lines enclose the spectral range chosen for analysis. Reported in Paper* **II**

variables. Originally, the experiment was conceptualized to investigate the effects of varying ingredients instead of building chemometrics for the quantification of drug content. The data set used in the study lacked the repetitive measurements necessary to create sufficient variance, which can be easily picked up during multivariate data analysis using PCA and PLS.

Another important data feature is the choice of ingredients. The ingredients chosen for the tablets were targeted for NIR spectroscopy thus providing clear and distinct spectral fingerprints. When measured with PTOFS, the drug and the filler showed an overlap of spectra for a major peak around 1200nm as shown in Figure 6.7. This meant that separating absorption from reduced scattering is a challenge because of the signals over lap. Removing scattering would remove absorption too. This might be the reason that PCA analysis of PTOFS absorption data showed the presence of filler particle influence in Figure 6.4.

6.2 Model selection and validation

API content/concentration prediction is a priority in the pharmaceutical industry for quality control of the tablets. The prediction requires building up of statistical models or chemometrics. For statistical model calibration, the data set is divided into calibration and validation sets. First, the model is calibrated on calibration set and then validated on validation set. Calibration involves training of the model and testing on a pre-set of calibration data. Leave-one-out cross-validation (LOOCV) and k-fold cross-validation (KFCV) methods were used for parameter calibration.

Figure 6.8: *Schematics representation for LOOCV scheme used for calibration and validation of prediction of API concentration. Total samples, n = 75. Modified from [167]*

In LOOCV each sample from training set is used for testing once as shown in Figure 6.8, while in KFCV, calibration set is divided into 'k' number of groups and each group is left out for testing once. Finally the optimized models chosen through calibration process is validated on validation set. Calibration and validation sets are chosen in two different ways.

First, 70% of the samples are chosen as calibration set (n_c) and remaining 30% of the samples as validation set (n_v). For PTOFS data with 75 samples, $n_c = 53$ and $n_v = 22$. Both calibration and validation sets are completely randomly chosen without forcing any structured selection. Second, the data is divided on the basis of average particle size of the tablets. Calibration set included all the tablets except the ones with the smallest average particle size (API = $50\mu m$ + Filler = $91\mu m$). So the structured selection of tablets based on average particle size was introduced in second case.

This choice of 70-30 split is most commonly used statistical choice in large data sets where calibration-prediction models are built. However, we made the choice after extensive data exploration with various options: different ratios for calibration-validation sets, 5 different types of pretreatments, LOOCV and KFCV (5, 7 and 10 fold cross validations). For paper we preferred the group-fold cross-validation [166] on the calibration set because the results showed no significant difference from LOOCV. Calibrated models were then applied to the validation set to predict the API concentration. The two cases discussed above, regarding the data split, were implemented to differentiate between general behaviour of the models and the behaviour based on structured selection of the data. Multivariate regression analysis [164] was performed using partial least squares (PLS) regression [166] to predict the API concentrations from both TNIRS and PTOFS spectra.
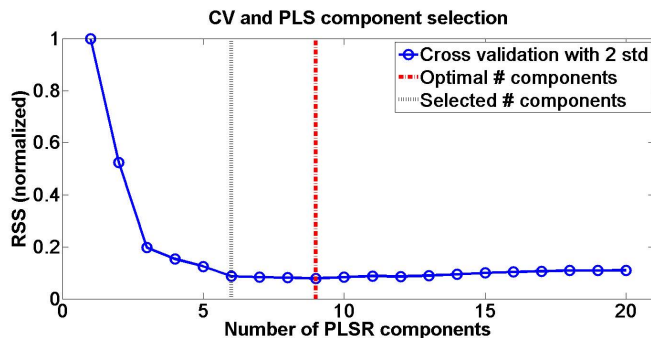
Figure 6.9: *Normalized residual sum of squares (RSS) is plotted against PLSR components. Cross validation (CV) was used on $n_c = 53$ with 20 PLSR components for calibration. Vertical red dotted line shows the optimal number of PLSR components and vertical black dotted line indicates the suggested PLSR components for selection by the modified "1 std error rule".*

6.3 Partial least squares regression (PLSR)

For the prediction of drug content (API concentration) in pharmaceutical tablets, using spectroscopic techniques, multivariate regression analysis is required [164]. Multivariate regression analysis is used for correlating the information in one data matrix ($\mathbf{X}$) to the information in another matrix ($\boldsymbol{y}$) and PLS is one way to perform the multivariate regression. We used PLS regression for the evaluation of absorption data from PTOFS because PLS finds PCs in $\mathbf{X}$ and $\boldsymbol{y}$ in such a way that their score values have maximum covariance i.e, PC1 in $\mathbf{X}$ has maximum covariance with PC1 in $\boldsymbol{y}$. This way, PLS finds the relevant (for $\boldsymbol{y}$) information which makes PLS model suitable for predictions.

For PLSR analysis, number of PLS components to be used in PLSR model were determined by using LOOCV and KFCV on calibration set while minimizing the mean of the residual sum of squares (**RSS**). For the selection of appropriate number of components to be used in PLS regression, modified "1 standard error rule" [166] was used. For minimum **RSS**, 2 standard deviations (**SD**) were calculated and then divided by square root of number of samples in calibration set. This value is added to the minimum **RSS** and the least number of components that fall under this limit are selected. Figure 6.9 shows the optimal number of components selected on bases of minimum **RSS** and selected number of components based on modified "1 std error rule".

After determining the number of PLS components, also known as latent variables (LVs), they were used on calibration set to build the prediction model which was then used on validation set to

predict the API concentration. $\mathbf{R^2}$ is the measure of variation explained in the model and is called "coefficient of determination". $\mathbf{R^2}$ is calculated and defined as:

$$\mathbf{R^2} = 1 - \frac{\mathbf{RSS}}{\mathbf{TSS}} = 1 - \frac{\sum_{n_v}(y - \hat{y})^2}{\sum_{n_v}(y - \frac{1}{n_v}\sum_{n_v} y)^2} \qquad (6.1)$$

where $\mathbf{TSS}$ is the total sum of squares. To evaluate how good the model predicts, the ratio of standard deviation and standard error of prediction, $\mathbf{RPD}$, was calculated. $\mathbf{RPD}$ is the ratio of $\mathbf{SD}$ of original $\boldsymbol{y}$ data (reference values for validation set) and the $\mathbf{SEP}$, which in fact is the root mean square error of prediction ($\mathbf{RMSEP}$).

$$\mathbf{SEP} = \mathbf{RMSEP} = \sqrt{\frac{1}{n_v}\sum_{n_v}(y - \hat{y})^2} \qquad (6.2)$$

$$\mathbf{RPD} = \frac{\mathbf{SD}}{\mathbf{SEP}} \qquad (6.3)$$

If the model is not able to predict accurately, the mean error calculated for prediction will can as large as the standard deviation of the original reference values. Thereby, an $\mathbf{RPD}$ value of 1 is undesirable. As the prediction errors starts becoming smaller and smaller, due to the increase in accuracy of prediction, higher $\mathbf{RPD}$ values are achieved. A satisfactory screening value of $\mathbf{RPD}$ is above 2.5 while values between 5-10 are considered adequate for quality control [167].

The choice of using "1 standard error rule" depends upon whether the generalized selection of optimal number of PLS components is the goal or not. Instead of using a fixed number of components, a generalized rule makes the selection robust. However, then individual PLS components does not hold any physical meaning. In the case of pharmaceutical application, the loading vectors of the PLS components have a physical meaning and each component ideally covers the variation of one single physical quantity under investigation in the tablets. In the case of isolated PTOFS absorption spectra, 1 or 2 components should suffice to cover the variance in absorption data which should, ideally, be due to the contribution of API only. However, we have shown the cross-talk between the optical properties. Absorption signal was not fully isolated as indicated by PCA as well. Therefore, more number of components are required to cover the variance introduced in absorption signal by scattering signal as well as the sparseness of the data set. For this reason, instead of choosing optimal number of components, it is more reasonable to choose **physically meaningful components** which could explain the variance in the data logically. TNIRS provided a clean signal with higher signal to

noise ration thereby 2 PLS components were enough to explain over 98% variance in the data. However, PTOFS showed physically meaningful loadings for four components which could explain the variance covered by each component as reported in Paper **II**. The MVDA scheme presented holds its value for other applications for building models used for quantification of ingredients.

6.3.1 Addition of scattering information

For PTOFS measured absorption spectra, an overlap between the pure drug and pure filler spectra was observed around 1200nm, as shown in Figure 2.4. This overlap possibly introduced an underlying filler signature in absorption spectra of all the tablets around that spectral region. Chemometrics built specifically for absorption spectra would behave biased towards this intrusion and models built using PLS will not be able to handle this information for quantification of drug concentration task adequately. However, PTOFS also provide separately wavelength dependent reduced scattering information related to the filler particle size and quantity in the tablet. That information can separately be analysed using Lorenz-Mie theory by Equation (2.6). This way, we can relate the scattering directly to only two variable: slope and amplitude of spectra. These two variables hold the information pertaining to filler size and quantity which got introduced into absorption spectra around 1200nm. By adding these two additional variable along with the wavelengths, PLS model will be able to perform better by taking into account the fact that absorption was not completely isolated. By introducing this hypothesis, PLS model performance was enhanced in Paper **II**. A very important result was the robustness of predictions on PTOFS data towards the variation in raw materials.

6.4 Importance of pretreatments

Unlike PTOFS, transmission NIR attenuation spectra includes both absorbance and underlying scattering signal from a tablet. Therefore it is essential to have that spectra pretreated for correction of scattering signal. Various techniques have been explored and adapted in the industry for preprocessing of NIR data as summed up by Rinnan et. al [165]. The effect of difference in particle sizes on TNIRS spectra is quantitatively the most important factor. It can either be compensated in post analysis empirically using multiple regression, or using derivatives [168], multiplicative scatter correction (MSC) [169] or standard normal variate [170]. In mean-Centre, the mean of each variable is subtracted from the variable to centre the data at zero. Pareto-scaling was also explored in which the variables are mean centred and then divided

by square root of the standard deviation of each variable. This makes the dominant large changes in variables decrease more than the smaller changes thereby making the large fold changes less dominant compared to clean data. Pareto-scaling can be regarded as intermediate between no scaling and auto-scaling as it assigns each variable a variance numerically equal to its initial standard deviation instead of unit variance [164, 165]. In Paper **II** MSC was used for the preprocessing of the TNIRS spectra because it takes away the slope and offset of the spectra which is the underlying signal for scattering. The spectra were then mean-centered to allow comparison with the mean-centered absorption spectra from PTOFS. Pretreatment is performed separately on calibration and validation sets to ensure that model built on calibration set is tested on completely uncorrelated validation set.

ANALYTICAL MODELLING FOR PTOF SPECTROSCOPY

PTOF spectroscopy is an advanced and powerful analysis tool, well established for discrimination between absorption and reduced scattering properties. Use of MC simulations makes it very reliable and accurate for estimation of optical properties in inverse problem. The technology, however, offers a huge potential to grow in all areas including instrumentation, measurement technique and data analysis. The working principles of PTOFS are discussed in Chapter 5. The technique heavily relies on the pre-calculated MC simulation data bases for solving the inverse problem of retrieving optical properties of a medium from measured light distribution profiles. This is at the expense computational time compared to extremely fast diffusion model which is not always adequate to apply. To expand the applications of PTOFS to wide range of fields and media, one of the major hurdles to overcome was the absence of an universal rapid and fast analytical modelling technique. In this chapter, an analytical solution to the time-dependent radiative transfer equation is discussed which was presented by A. Liemert amd A. Kienle et . al [47], here referred to as LK-model or LKM. The model is presented along with it's implementation [171] which served as the basis for Paper **III**.

7.1   LK model or LKM

The LKM has an analytical dependence on time variable. It is a solution to the time-dependent RTE in an anisotropically scattering medium based on an infinite space Green's function. We can write time-dependent RTE for radiance $I = I(r, \mu, t)$ by internal source density Q in spherically symmetric medium as:

$$\frac{1}{c}\frac{\partial I}{\partial t} + \mu\frac{\partial I}{\partial r} + \frac{1-\mu^2}{r}\frac{\partial I}{\partial \mu} + \sigma_t I = \sigma_s A I + \frac{Q}{4\pi} \qquad (7.1)$$

where A is scattering operator which incorporated rotationally invariant phase function $f(\hat{s} \cdot \hat{s}')$, $\sigma_t = \sigma_a + \sigma_s$ is total interaction coefficient, σ_a is absorption coefficient, σ_s is scattering coefficient and μ is the directional cosine vector between propagation direction $\hat{s}$ and unit position vector $\hat{r}$. The source term for impulse response in space and time is:

$$Q(r,t) = \frac{\delta(r)}{4\pi r^2}\delta(t) \qquad (7.2)$$

$f(\hat{s} \cdot \hat{s}')$ can be expanded in Legendre Polynomials P_l with expansion coefficients f_l and by using plane wave decomposition in spherical coordinates and using spherical harmonics, radiance can be written in terms of Legendre polynomial series

$$I(r,\mu,t) = \sum_{l=0}^{\infty} \frac{2l+1}{4\pi}I_l(r,t)P_l(\mu) \qquad (7.3)$$

where $I_l(r,t)$ is the radial dependent kernal and has a form of an inverse spherical Hankel forward transform:

$$I_l(k,t) = 4\pi(-j)^l \int_0^\infty I_l(r,t)j_l(kr)r^2 dr \qquad (7.4)$$

j_l denotes spherical Bessel function fo first kind. Using Equation (7.4) with series representation leads to a linear and time invariant system (LTI system)

$$\frac{1}{c}\frac{dI_l(k,t)}{dt} + \frac{I}{2l+1}jkI_{l-1}(k,t) + \sigma_l I_l(kt) + ...$$

$$\frac{l+1}{2l+1}jkI_{l+1}(k,t) = \delta(t)q_l \qquad (7.5)$$

where $\sigma_l = \sigma_a + (1 - f_l)\sigma_s$ and $q_l = \delta_{l0}$. One side Lalpace transform can provide time-dependent impulse response of a LTI system with zero initial conditions. Set of linear equations can be formed from LTI system and with some matrix manipulation and inverse Laplace transform, a simple power series solution is achieved. To make it computationally effective Eigenvalue decomposition, is used and matrix diagonals are solved to get time dependent moods needed for Equation (7.3).

For numerical evaluation, limits on Equation (7.4) are replaced for a large sphere with radius R and wave number k becomes a

discrete value ξ_{kl} dependent on transform order l. Then alternative inverse transform for the integral representation on an inverse spherical Hankel transform becomes

$$I_l(r,t) = \frac{j^l}{2\pi R^3} \sum_{\xi_{lk}>0} I_{kt}(t) \frac{j_l(\xi_{lk}r)}{j_{l+1}^2(\xi_{lk}R)} \qquad (7.6)$$

R is the radius of a sphere assumed around the source to define space. The solution is fast convergent. For the evaluation of fluence, required roots are given by positive zeros of sine function $\xi_{k0} = k\pi/R$. For every root, system of linear equations is solved by eigenvalue decomposition of formed matrix. Thus the simple form of fluence given by lowest order coefficent $I_0(r,t)$ becomes

$$\Phi(r,t) = \frac{l}{2rR^2} \sum_{k=1}^{\infty} k I_{k0}(t) sin(\xi_{k0}r) \qquad (7.7)$$

7.2 Limitations

Analytical solutions are often prepared for particular geometries or cases and are not as universal as MCS. This LKM model is a solution for an infinite anisotropic medium only where boundary effects are not considered. The assumption of the fluence in a sphere of an appropriate radius depends on the choice of g. For lower values of g, fluence estimation is far from perfect but it stabilizes for $g > 0.6$. For any finite geometries, boundary conditions are a must to get exact solution. Another limit to the model is the application in the estimation of fluence only. It has not been expanded to include the radiance as well. Although there are no assumptions made in the derivation of the solution, numerical estimation requires approximations of the order of series expansion to get good acceptable agreement to MCS.

7.3 Fiber geometry considerations

The LKM is a point source model which does not take into account the finite geometry of the optical fibers used for delivering and collecting photon packets. Thereby leaving it for post-processing of the fluence profiles generated by the LKM. Considerations of the optical fiber geometry are important especially at small fiber separations. Larger distances render geometry effects minimal because of ratio of fiber separation to the fiber diameter.

Fiber geometry effects can be introduced simply by the process of convolution or integral multiplication. For the geometry consideration, we assumed that both the source and detector fiber have same radius R_f. Another assumption was for the fibers to have a top hat emission profile i.e, source fiber transmitted the same amount of light regardless of the position on the fiber tip.
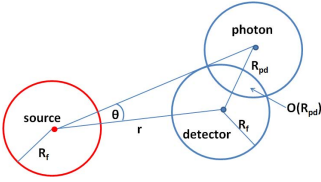
Figure 7.1. *Adapted from [139]. An illustration of the source and a single photon packet, before convolution, as points, and after convolution with the source fiber irradiance distribution, solid circles. R_d is the fiber separation and θ is the angle. R_{pd} is the detector-photon distance and $O(R_{pd})$ is the area of overlap between the detector fiber and the photon (convoluted with the source fiber irradiance response). r is the separation between source and detector and R_f is the radius of both the source and detector fiber.*
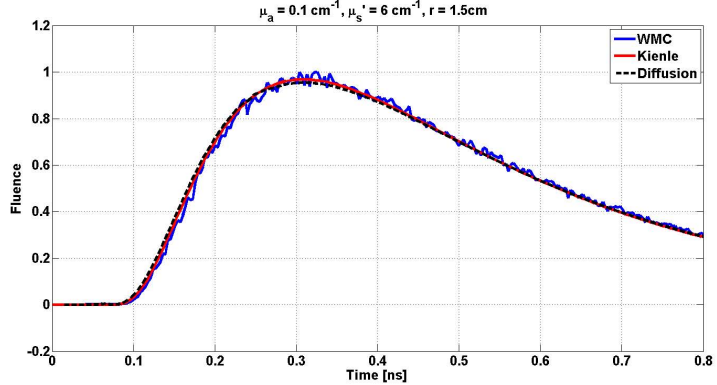
Figure 7.2: *PTOFS profiles in diffuse regime where DM is valid.*

Figure 7.1 illustration the necessary notations for considerations of fiber geometry. To use the circular symmetry around the source, the overlap function O is integrated over all angles, θ, removing the need to store any spatial information but R_p for each photon packet detection event [139].

The normalized overlap function for two circles[1] of the same size at distance R_{pd} from each other is:

$$O(R_{pd}) = \frac{2}{R_f^2}(R_f^2 arccos(\frac{R_{pd}}{2R_f}) - \frac{R_{pd}}{2}\sqrt{R_f^2 - \frac{R_{pd}^2}{4}}) \qquad (7.8)$$

This overlap function is calculated at 16 points on the surface of the fiber tip to get the weights for the fiber irradiance on surface when convolved with LKM fluence response. The final LKM profile for PTOFS data is of the form:

$$LKM(r,t) = \int_a^b O(R_{pd})\Phi(r,t)rd_r \qquad (7.9)$$

7.4 Results beyond diffusion approximation

Break down of the diffusion model is described in Section 2.4.4. Here, the simulation results are presented for the region where diffusion is valid as well as beyond the diffusion validity. With the fiber geometry considerations included in the LKM, the performance of the analytical solution can be compared to WMC and diffusion model (DM). Figure 7.2 shows the PTOFS generated fluence curves for the LKM and DM in comparison to WMC. As the optical properties used are adequate for the use of DM, a perfect agreement between all modalities can be observed.

---

[1]http://mathworld.wolfram.com/Circle-CircleIntersection.html
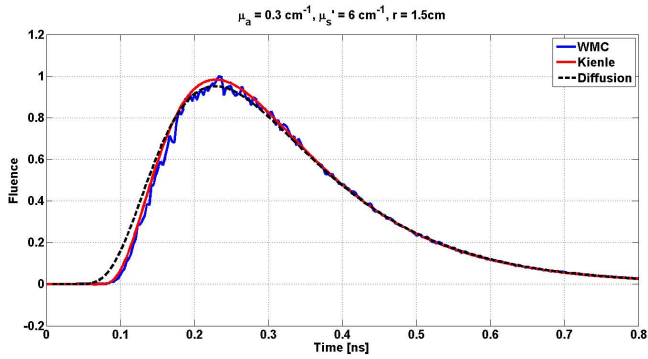
Figure 7.3: *PTOFS profiles when absorption starts to increase. DM is approaching it's limit for validity.*
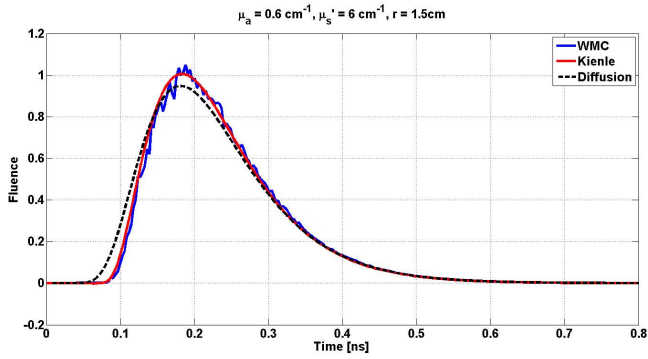
Figure 7.4: *PTOFS profiles for high absorption when it becomes comparable to reduced scattering beyond diffusion approximation.*
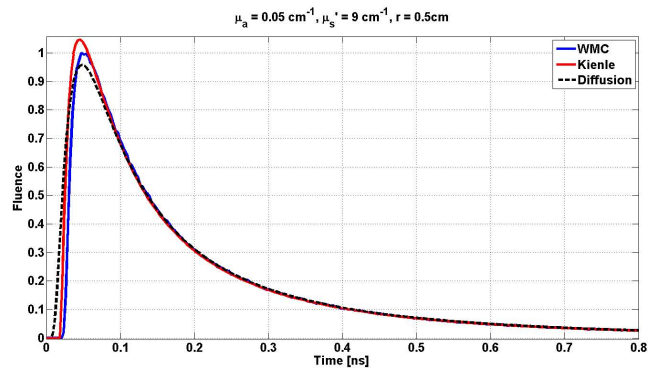
Figure 7.5: *PTOFS fluence profiles for very short fiber separations of 5mm*

Increasing the absorption of the medium, while keeping the reduced scattering and fiber separation fixed, starts shifting the DM profile away from the expected WMC simulated curve. This effect is reported in Paper **III** in comparison to LKM and WMC. Figure 7.3 illustrates the optical regime pushing the limits of the diffusion model and Figure 7.4 shows a significant divergence of the DM from WMC indicating that the DM is no longer adequate to be used with given optical properties. In comparison, LKM model produced consistently accurate results.

In Figure 7.5 the boundaries are even pushed where the LKM starts experiencing deviation from WMC curve. However, it is still better than DF at a very close fiber separation distance. This could be explained by the modelling of fiber geometry and in no way suggests the limitation of the analytical solution. The LKM has proven to be a valuable advancement in terms of analytical solutions and also helped demonstrate that PTOFS instrument used in Paper **III** is capable of producing robust estimation of the optical properties with implementation of an analytical solution as well. The chance to replace WMC data bases was a positive sign as it not only significantly reduced the computation time by eliminating the need of pre-calculations used in WMC but also opened doors to more applications of the PTOFS technology. Indeed the claimed precision and computational simplicity of the LKM would enable high accuracy real-time DOS measurements for the range of optical parameters typical for biological tissue and numerous common food products. Furthermore the LKM has claimed to facilitate measurements at small source to detector separations, which could be highly suitable for development of miniature probes for medical and cost-efficient industrial applications [172]. In Paper **III**, investigated dynamic range of optical properties showed the validity of this model, robust estimation of optical properties by PTOF system and independence of the instrument.

CONCLUSIONS

The research conducted in this thesis is focused on accurate, fast and reliable estimation of the optical properties in different consumable turbid media. Dairy products, i.e., milk and yoghurt, and pharmaceuticals were investigated for the application of two different diffuse optical spectroscopic techniques. The Ph.D. work has focused first on adaptation and development of a steady-state continuous-wave measurement technique applied for measuring the structural differences between milk and yoghurt. The technique was later further analysed with monte carlo simulations to investigate its sensitivity. Then a time-domain technique was applied for the quality control in pharmaceuticals by quantifying the drug content. Finally with the use of analytical modelling, the time-domain measurement system was investigated for the potential increase in its future application industries.

The first scientific contribution of the Ph.D. came from adaptation and improvement of a diffusion based measurement technique, oblique incidence reflectometry (OIR), for the structural characterization of the optical properties of milk and yoghurt. This required the ability to resolve the optical interactions that happen on scales of optical path lengths relevant to the milk and yoghurt samples from visible to NIR regime. Research conducted lead to the construction of a non-contact, non-invasive, versatile measurement platform for broadband characterization of the optical properties. As the fundamental interactions are the same, the knowledge is transferable to the wide range of applications and spectral regions. The design considerations for a camera based non-invasive system discussed in the thesis can serve as a tool to build an application specific instrument as presented in Paper **I**.

The diffusion based models are an approximation to RTE but can provide a good estimate of optical properties in the

multiple scattering regime. With broad band characterization, few wavelengths used with physical based modelling could discriminate between diffuse reflectance profiles of varying particle concentrations and the effective size. Precision of the measurements is of rather great relevance as opposed to very high spectral resolution. To measure the accuracy of the current system and explore the OIR technique, sensitivity analysis was conducted which showed the possible limitations and reasoning for errors in the OIR results. The sensitivity analysis not only demonstrated the system requirements in terms of resolution and field of view, which vary depending upon the dynamic range of optical properties measured, but also highlights the significance of a priori knowledge of g for accurate estimations. This work resulted in a scientific contribution as summed up in Paper **IV**.

In future, the precision of non-contact measurement system used with physical based models could be improved, as the technique has shown promise in the inspection of structural changes in the dairy products.

Another major contribution came from the application and analysis of PTOF spectroscopy on pharmaceuticals. PTOF spectroscopy is an established technique for quantifying the absorption and reduced scattering properties of light scattering samples. First time a new advanced broadband PTOF spectrometer was applied in a large data set study of tablets to quantify the active pharmaceutical ingredient in the tablets. This thesis presents how the multivariate data analysis for building chemometrics can be used. PTOF was used in the wavelength range of 1050nm to 1350nm and not only the drug concentrations were adequately quantified but the structural properties and the process parameters could be well separated as well. Time-domain spectroscopy could provide important insights into both structural and chemical composition of the tablets separately, and establish the link between optical and physical parameters in rather meaningful way as presented in Paper **II**.

In future, a well designed data set could prove PTOFS potential rather more clearly. The use of more advanced multivariate data analysis techniques could improve further on quantification. An effort to eliminate the cross-talk could increase precision.

The final contribution is the result of testing and verification of a new analytical solution to RTE. In PTOF spectroscopy, modelling choice was limited to diffusion model or MC simulations: first is limited to diffuse media and the second is time inefficient. The first experimental verification of the new analytical solution not only promised the wider applications of PTOFS but validated

the robustness of the technique shown in the linearity study of the liquid optical phantoms presented in Paper **III**. The advance spectrometer used in the study showed the independence of the instrument that, with analytical modelling, is suitable for the use in biomedicine as well industrial applications.

The quality of the dairy products is associated with the structural properties of the medium while in pharmaceuticals, the drug concentration is equally important. Cost effective, non-contact, non-invasive inspection techniques are desirable in food industry while pharmaceutical industry is motivated by the robustness of a non-destructive technology. This thesis presents a versatile sample characterization technique for dairy industry along with a robust, non-destructive method as a choice for pharmaceutical industry. Finally, the prospects of the application increase with the use of analytical modelling in PTOFS is presented. This enables research into both instrumentation and methodology for the techniques.

COMMENTS ON THE PAPERS

I **Non-invasive assessment of dairy products using spatially resolved diffuse reflectance spectroscopy**

Otto H. A. Nielsen, Faisal Kamran, Anders B. Dahl, Jacob L. Skytte, Frederik D. Nielsen, Carsten L. Thomsen, Peter E. Andersen, Rasmus Larsen, Jeppe R. Frisvad

Measuring the microstructural development of dairy products is highly important as it affects the optical properties. We present a rapid non-contact non-invasive technology that quantifies reduced scattering and absorption of samples and is suitable for in-line inspection. Hyperspectral images of diffuse reflectance are captured in the range of 470 nm - 1020 nm for obliquely incident laser light on sample. The technique is experimentally validated with measurements on milk and yoghurt which clearly discriminate their reduced scattering caused by microstructure. Procedure to deal with number challenges in proposed analysis technique is also presented.

I participated in the formulation of the idea for the publication and conducted the first measurement campaign with milk samples. I helped in determination of optical elements for laser delivery to the sample and participated in writing of the paper.

II **Transmission near-infrared and photon time-of-flight spectroscopy in a comparative analysis of pharmaceuticals**

Faisal Kamran, Otto H. A. Nielsen, Anders Sparén, Olof Svensson, Jonas Johansson, Stefan Andersson-Engels, Peter E. Andersen, Dmitry Khoptyar

A comprehensive study of PTOF spectroscopy applied for evaluation of pharmaceuticals in the range of 1050 nm - 1350 nm is presented. PTOFS is compared with transmission NIR spectroscopy, the industry standard. Multivariate data analysis is used to evaluate absorption spectra for the prediction of drug content. We show that analysis based on PTOFS spectra is more robust. Additionally, PTOFS provides reduced scattering spectra which is analysed separately. Results show PTOFS potential to differentiate not only between different methods used to manufacture filler material for tablets but also process parameter like compression force. We present PTOFS as a viable alternative for pharmaceutical analysis.

I participated in the planning of the work, and was responsible for the whole measurements campaign and data analysis. I participated in drawing conclusions from the analysis and wrote the manuscript.

III Computational effective solution of the inverse problem in time-of-flight spectroscopy

Faisal Kamran, Otto H. A. Abildgaard, Arman A. Subash, Peter E. Andersen, Stefan Andersson-Engels, Dmitry Khoptyar

This article presents the experimental validation of a newly proposed time-domain analytical solution for radiative transfer equation. A. Liemert and A. Kienle proposed a model (LKM) beyond diffusion approximation. We use photon time-of-flight spectroscopy and liquid phantoms to validate the model by comparing the evaluated results with MC simulations and diffusion model. This validation promises a significant increase in PTOFS application by replacing the need of MC data bases by a fast analytical model in certain cases.

I participated in the formulation of the idea for the publication, designed the experiments with liquid phantoms, conducted the measurement, performed the analysis and participated in writing of the paper.

IV Sensitivity analysis for Oblique incidence reflectometry using Monte Carlo simulations.

Faisal Kamran, Peter E. Andersen

In this manuscript, we show that OIR is an advantageous spectroscopic technique but limited by its implementation. Although, being a technique based on diffusion model, it inherits certain limitations, yet can be a reliable method for estimation of optical properties in turbid media if right imaging system is used. In this article we present the importance of a priori knowledge of anisotropy of the medium, resolution and field of view requirements of imaging system depending in varying dynamic range of optical properties and the effects these choices have on evaluation of experimental data. We use monte carlo simulations for analysis and compare the results with experimental data acquired with OIR on milk samples with varying fat content.

I participated in the formulation of the idea for the publication, performed the analysis setting up Monte Carlo simulations, interpreted the results and drafted the manuscript.

References

[1]. O. H. A Nielsen, F. Kamran, A. L. Dahl, J. L. Skytte, F. D. Nielsen, C. L. Thomsen, P. E. Andersen, R. Larsen and J. Frisvad. *Non-invasive assessment of dairy products using spatially resolved diffuse reflectance spectroscopy.* Submitted to Applied Specroscopy **-**, – (2014).

[2]. Faisal Kamran, Otto Højager Attermann Nielsen, Anders Sparén, Olof Svensson, Jonas Johansson, Stefan Andersson-Engels, Peter Andersen and Dmitry Khoptyar. *Spectroscopic analysis of pharmaceuticals in the close NIR range using PToF spectroscopy.* Applied Spectroscopy **69**, 389–397 (2015).

[3]. F. Kamran, O. H. A. Nielsen, Abildgaard, A. A. Subash, P. E. Andersen, S. Andersson-Engels and D. Khoptyar. *Computational effective solution of the inverse problem in time-of-flight spectroscopy.* Submitted to Journal of Biomedical Optics **-**, – (2014).

[4]. F. Kamran and P. E. Andersen. *Sensitivity analysis for Oblique incidence reflectometry using Monte Carlo simulations.* to be submitted to Journal of Biomedical Optics **-**, – (2014).

[5]. Faisal Kamran, Otto Højager Attermann Nielsen, Stefan Andersson-Engels and Dmitry Khoptyar. *Broadband photon time of flight spectroscopy: advanced spectroscopic analysis for ensuring safety and performance of pharmaceutical tablets.* In *Asia Communications and Photonics Conference* pp AF3K–4. Optical Society of America (2013).

[6]. D. Khoptyar, F. Kamran, O. H. A Nielsen, A. Sparén, J. Johansson, O. svensson and S. Andersson-Engels. *Broadband photon time of flight spectroscopy: advanced spectroscopic tool for PAT in pharmaceutical and dairy industries.* In *EuroPACT* pp pp–. - (2014).

[7]. J Michael Hollas. *Modern spectroscopy.* John Wiley & Sons (2004).

[8]. Joseph R Lakowicz. *Principles of fluorescence spectroscopy.* Springer (2007).

[9]. Alberto Diaspro et al. *Confocal and two-photon microscopy: foundations, applications, and advances* vol. 1. Wiley-Liss New York (2002).

[10]. JOHN C FISHER. *Photons, physiatrics, and physicians: a practical guide to understanding laser light interaction with living tissue, part I.* Journal of clinical laser medicine & surgery **10**, 419–426 (1992).

[11]. Michael I Mishchenko. *Gustav Mie and the fundamental concept of electromagnetic scattering by particles: a perspective.* Journal of Quantitative Spectroscopy and Radiative Transfer **110**, 1210–1222 (2009).

[12]. John William Strutt Baron Rayleigh. *On the light from the sky, its polarization and color.* Itek Corporation (1966).

[13]. Gustav Mie. *Beiträge zur Optik trüber Medien, speziell kolloidaler Metallösungen.* Annalen der physik **330**, 377–445 (1908).

[14]. Chandrasekhara Venkata Raman and Kariamanikkam Srinivasa Krishnan. *A new type of secondary radiation.* Nature **121**, 501–502 (1928).

[15]. L Brillouin. *Diffusion of light in transparent homogenous solid due to vibrations of thermal origin.* Ann. Phys. Ser **9**, 17–88 (1922).

[16]. RY Chiao, CH Townes and BP Stoicheff. *Stimulated Brillouin scattering and coherent generation of intense hypersonic waves.* Physical Review Letters **12**, 592 (1964).

[17]. Sune Svanberg. *Atomic and molecular spectroscopy: basic aspects and practical applications; with 14 tables.* Springer (2004).

[18]. Craig F Bohren and Donald R Huffman. *Absorption and scattering of light by small particles.* John Wiley & Sons (2008).

[19]. Akira Ishimaru. *Wave propagation and scattering in random media* vol. 2. Academic press New York (1978).

[20]. John W Strutt. *XV. On the light from the sky, its polarization and colour.* The London, Edinburgh, and Dublin Philosophical Magazine and Journal of Science **41**, 107–120,274–279 (1871).

[21]. SL Jacques, CA Alter and SA Prahl. *Angular dependence of HeNe laser light scattering by human dermis.* Lasers Life Sci **1**, 309–333 (1987).

[22]. Mark R Arnfield, J Tulip and MS McPhee. *Optical propagation in tissue with anisotropic scattering.* Biomedical Engineering, IEEE Transactions on **35**, 372–381 (1988).

[23]. S.L Jacques and S.A Prahl. optical properties. http://omlc.ogi.edu/education/ (2012). [Online; accessed 01-Dec-2013].

[24]. Louis G Henyey and Jesse L Greenstein. *Diffuse radiation in the galaxy.* The Astrophysical Journal **93**, 70–83 (1941).

[25]. T Tarvainen, V Kolehmainen, A Pulkkinen, M Vauhkonen, M Schweiger, SR Arridge and JP Kaipio. *An approximation error approach for compensating for modelling errors between the radiative transfer equation and the diffusion approximation in diffuse optical tomography.* Inverse Problems **26**, 015005 (2010).

[26]. R Graaff, JG Aarnoudse, Jaap R Zijp, PMA Sloot, FFM De Mul, Jan Greve and MH Koelink. *Reduced light-scattering properties for mixtures of spherical particles: a simple approximation derived from Mie calculations.* Applied optics **31**, 1370–1376 (1992).

[27]. Judith R Mourant, Tamika Fuselier, James Boyer, Tamara M Johnson and Irving J Bigio. *Predictions and measurements of scattering and absorption over broad wavelength ranges in tissue phantoms.* Applied Optics **36**, 949–957 (1997).

[28]. Steven L Jacques. *Optical properties of biological tissues: a review.* Physics in medicine and biology **58**, R37 (2013).

[29]. S.L Jacques and S.A Prahl. Mie calculator. http://omlc.ogi.edu/calc/ (2012). [Online; accessed 01-Dec-2013].

[30]. August Beer. *Bestimmung der Absorption des rothen Lichts in farbigen Flüssigkeiten.* Annalen der Physik **162**, 78–88 (1852).

[31]. D ˍ T Delpy, M Cope, Pi Van der Zee, S Arridge, Susan Wray and J Wyatt. *Estimation of optical pathlength through tissue from direct time of flight measurement.* Physics in medicine and biology **33**, 1433 (1988).

[32]. Angelo Sassaroli and Sergio Fantini. *Comment on the modified Beer–Lambert law for scattering media.* Physics in Medicine and Biology **49**, N255 (2004).

[33]. A Schuster. *Radiation through a foggy atmosphere.* The Observatory **26**, 379–381 (1903).

[34]. Arthur Schuster. *Radiation through a foggy atmosphere.* The astro-

physical journal **21**, 1 (1905).

[35]. Subrahmanyan Chandrasekhar. *Radiative transfer*. Courier Dover Publications (2013).

[36]. Kenneth M Case and Paul F Zweifel. *Linear transport theory* vol. 196. Addison-Wesley Reading, Mass. (1967).

[37]. CL Longmire and MN Rosenbluth. *Diffusion of charged particles across a magnetic field*. Physical Review **103**, 507–510 (1956).

[38]. Larry Reynolds, C Johnson and Akira Ishimaru. *Diffuse reflectance from a finite blood medium: applications to the modeling of fiber optic catheters*. Applied Optics **15**, 2059–2067 (1976).

[39]. RL Longini and R Zdrojkowski. *A note on the theory of backscattering of light by living tissue*. Biomedical Engineering, IEEE Transactions on pp 4–10 (1968).

[40]. Ashley J Welch, Martin JC Van Gemert and Willem M Star. *Definitions and overview of tissue optics*. Springer (2011).

[41]. AJ Welch and MJC van Gemert. *Optical-Thermal Response of laser Irradiated Tissue*. Plenum Press (1995).

[42]. Simon R Arridge and Martin Schweiger. *Image reconstruction in optical tomography*. Philosophical Transactions of the Royal Society of London. Series B: Biological Sciences **352**, 717–726 (1997).

[43]. Marvin L Adams and Edward W Larsen. *Fast iterative methods for discrete-ordinates particle transport calculations*. Progress in nuclear energy **40**, 3–159 (2002).

[44]. Kuan Peng, Xinbo Gao, Xiaochao Qu, Nunu Ren, Xueli Chen, Xiaowei He, Xiaorei Wang, Jimin Liang and Jie Tian. *Graphics processing unit parallel accelerated solution of the discrete ordinates for photon transport in biological tissues*. Applied optics **50**, 3808–3823 (2011).

[45]. ED Aydin, CRE De Oliveira and AJH Goddard. *A finite element-spherical harmonics radiation transport model for photon migration in turbid media*. Journal of Quantitative Spectroscopy and Radiative Transfer **84**, 247–260 (2004).

[46]. S Wright, M Schweiger and SR Arridge. *Reconstruction in optical tomography using the PN approximations*. Measurement Science and Technology **18**, 79 (2007).

[47]. André Liemert and Alwin Kienle. *Analytical solution of the radiative transfer equation for infinite-space fluence*. Physical Review A **83**, 015804 (2011).

[48]. André Liemert and Alwin Kienle. *Analytical Green's function of the radiative transfer radiance for the infinite medium*. Physical Review E **83**, 036605 (2011).

[49]. Alexander D Klose and Edward W Larsen. *Light transport in biological tissue based on the simplified spherical harmonics equations*. Journal of Computational Physics **220**, 441–470 (2006).

[50]. Martin Frank, Axel Klar, Edward W Larsen and Shugo Yasuda. *Time-dependent simplified¡ i¿ P¡/i¿¡ sub¿ N¡/sub¿ approximation to the equations of radiative transfer*. Journal of Computational Physics **226**, 2289–2305 (2007).

[51]. Michael Chu, Karthik Vishwanath, Alexander D Klose and Hamid Dehghani. *Light transport in biological tissue using three-dimensional frequency-domain simplified spherical harmonics equations*. Physics in medicine and biology **54**, 2493 (2009).

[52]. Jorge Bouza Domínguez and Yves Bérubé-Lauzière. *Diffuse light propagation in biological media by a time-domain parabolic simplified spherical harmonics approximation with ray-divergence effects*. Applied op-

tics **49**, 1414–1429 (2010).

[53]. Yves Bérubé-Lauzière, Vivian Issa and Jorge Bouza Dominguez. *Simplified spherical harmonics approximation of the time-dependent equation of radiative transfer for the forward problem in time-domain diffuse optical tomography.* In *SPIE BiOS: Biomedical Optics* pp 717403–717403. International Society for Optics and Photonics (2009).

[54]. Andre Liemert and Alwin Kienle. *Analytical solutions of the simplified spherical harmonics equations.* Optics letters **35**, 3507–3509 (2010).

[55]. John Michael Hammersley and David Christopher Handscomb. *Monte carlo methods* vol. 1. Springer (1964).

[56]. Edward A Bucher. *Computer simulation of light pulse propagation for communication through thick clouds.* Applied Optics **12**, 2391–2400 (1973).

[57]. BC Wilson and G Adam. *A Monte Carlo model for the absorption and flux distributions of light in tissue.* Medical Physics **10**, 824–830 (1983).

[58]. Lihong Wang, Steven L Jacques and Liqiong Zheng. *MCML—Monte Carlo modeling of light transport in multi-layered tissues.* Computer methods and programs in biomedicine **47**, 131–146 (1995).

[59]. Yuxuan Zhan, Adam T Eggebrecht, Joseph P Culver and Hamid Dehghani. *Image quality analysis of high-density diffuse optical tomography incorporating a subject-specific head model.* Frontiers in neuroenergetics **4** (2012).

[60]. Linda Persson, Elias Kristensson, Lisa Simonsson and Sune Svanberg. *Monte Carlo simulations related to gas-based optical diagnosis of human sinusitis.* Journal of biomedical optics **12**, 054002–054002 (2007).

[61]. SA Prahl, M Keijzer, SL Jacques and AJ Welch. *A Monte Carlo model of light propagation in tissue.* Dosimetry of laser radiation in medicine and biology **5**, 102–111 (1989).

[62]. Steven L Jacques and Lihong Wang. *Monte Carlo modeling of light transport in tissues.* In *Optical-thermal response of laser-irradiated tissue* pp 73–100. Springer (1995).

[63]. Lihong Wang and Steven L Jacques. *Monte Carlo modeling of light transport in multi-layered tissues in standard C.* The University of Texas, MD Anderson Cancer Center, Houston (1992).

[64]. Lihong V Wang and Hsin-i Wu. *Biomedical optics: principles and imaging.* John Wiley & Sons (2012).

[65]. Caigang Zhu and Quan Liu. *Review of Monte Carlo modeling of light transport in tissues.* Journal of biomedical optics **18**, 050902–050902 (2013).

[66]. T Binzoni, TS Leung, AH Gandjbakhche, D Rüfenacht and DT Delpy. *The use of the Henyey–Greenstein phase function in Monte Carlo simulations in biomedical optics.* Physics in medicine and biology **51**, N313 (2006).

[67]. Norbert S Żołek, Adam Liebert and Roman Maniewski. *Optimization of the Monte Carlo code for modeling of photon migration in tissue.* Computer methods and programs in biomedicine **84**, 50–57 (2006).

[68]. Alwin Kienle and Michael S Patterson. *Determination of the optical properties of turbid media from a single Monte Carlo simulation.* Physics in medicine and biology **41**, 2221 (1996).

[69]. Antonio Pifferi, Paola Taroni, Gianluca Valentini and Stefan Andersson-Engels. *Real-time method for fitting time-resolved reflectance and transmittance measurements with a Monte Carlo model.* Applied optics **37**, 2774–2780 (1998).

[70]. Erik Alerstam, Stefan Andersson-Engels and Tomas Svensson. *White Monte Carlo for time-resolved photon migration.* Journal of biomedical optics **13**, 041304–041304 (2008).

[71]. Philippe Thueler, Igor Charvet, Frederic Bevilacqua, M St Ghislain, G Ory, Pierre Marquet, Paolo Meda, Ben Vermeulen and Christian Depeursinge. *In vivo endoscopic tissue diagnostics based on spectroscopic absorption, scattering, and phase function properties.* Journal of biomedical optics **8**, 495–503 (2003).

[72]. Erik Alerstam, Stefan Andersson-Engels and Tomas Svensson. *Improved accuracy in time-resolved diffuse reflectance spectroscopy.* Opt. Express **16**, 10440–10454 (2008).

[73]. S.L Jacques and S.A Prahl. 3D MCML model. http://omlc.ogi.edu/software/ (2012). [Online; accessed 01-Dec-2013].

[74]. André Liemert and Alwin Kienle. *Exact and efficient solution of the radiative transport equation for the semi-infinite medium.* Scientific reports **3** (2013).

[75]. Hendrik Christoffel van de Hulst. *Light scattering by small particles.* Courier Dover Publications (2012).

[76]. James J Duderstadt and William Russell Martin. *Transport theory.* Transport theory., by Duderstadt, JJ; Martin, WR. Chichester (UK): John Wiley & Sons, 10+ 613 p. **1** (1979).

[77]. T Durduran, AG Yodh, B Chance and DA Boas. *Does the photon-diffusion coefficient depend on absorption?* JOSA A **14**, 3358–3365 (1997).

[78]. Steven L Jacques and Brian W Pogue. *Tutorial on diffuse light transport.* Journal of Biomedical Optics **13**, 041302–041302 (2008).

[79]. Koichi Furutsu and Yukio Yamada. *Diffusion approximation for a dissipative random medium and the applications.* Physical Review E **50**, 3634 (1994).

[80]. Michele Bassani, Fabrizio Martelli, Giovanni Zaccanti and Daniele Contini. *Independence of the diffusion coefficient from absorption: experimental and numerical evidence.* Optics letters **22**, 853–855 (1997).

[81]. T Nakai, G Nishimura, K Yamamoto and M Tamura. *Expression of optical diffusion coefficient in high-absorption turbid media.* Physics in medicine and biology **42**, 2541 (1997).

[82]. R Graaff and JJ Ten Bosch. *Diffusion coefficient in photon diffusion theory.* Optics letters **25**, 43–45 (2000).

[83]. Romain Pierrat, Jean-Jacques Greffet and Rémi Carminati. *Photon diffusion coefficient in scattering and absorbing media.* JOSA A **23**, 1106–1110 (2006).

[84]. M Blanco, J Coello, H Iturriaga, S Maspoch and C De La Pezuela. *Near-infrared spectroscopy in the pharmaceutical industry.* Analyst **123**, 135R–150R (1998).

[85]. Yves Roggo, Pascal Chalus, Lene Maurer, Carmen Lema-Martinez, Aurélie Edmond and Nadine Jent. *A review of near infrared spectroscopy and chemometrics in pharmaceutical technologies.* Journal of Pharmaceutical and Biomedical Analysis **44**, 683–700 (2007).

[86]. Gabriele Reich. *Near-infrared spectroscopy and imaging: basic principles and pharmaceutical applications.* Advanced drug delivery reviews **57**, 1109–1143 (2005).

[87]. Mafalda Cruz Sarraguça and Joao Almeida Lopes. *Quality control of pharmaceuticals with NIR: From lab to process line.* Vibrational Spectroscopy **49**, 204–210 (2009).

[88]. Lihong V Wang and Steven L Jacques. *Source of error in calculation*

of optical diffuse reflectance from turbid media using diffusion theory.
Computer methods and programs in biomedicine **61**, 163–170 (2000).

[89]. Yaqin Chen, Liji Cao and Liqun Sun. *Asymmetric diffusion model for oblique-incidence reflectometry.* Chinese Optics Letters **9**, 101701 (2011).

[90]. Roger J Zemp. *Phase-function corrected diffusion model for diffuse reflectance of a pencil beam obliquely incident on a semi-infinite turbid medium.* Journal of biomedical optics **18**, 067005–067005 (2013).

[91]. N. Joshi, C. Donner and H.W. Jensen. *Noninvasive measurement of scattering anisotropy in turbid materials by nonnormal incident illumination.* Optics letters **31**, 936–938 (2006).

[92]. CC Fagan, M. Leedy, M. Castillo, FA Payne, CP O'Donnell and DJ O'Callaghan. *Development of a light scatter sensor technology for on-line monitoring of milk coagulation and whey separation.* Journal of Food Engineering **83**, 61–67 (2007).

[93]. Da-Wen Sun. *Infrared spectroscopy for food quality analysis and control.* Academic Press (2009).

[94]. L Čurda and O Kukačková. *NIR spectroscopy: a useful tool for rapid monitoring of processed cheeses manufacture.* Journal of Food Engineering **61**, 557–560 (2004).

[95]. Haibo Huang, Haiyan Yu, Huirong Xu and Yibin Ying. *Near infrared spectroscopy for on/in-line monitoring of quality in foods and beverages: A review.* Journal of Food Engineering **87**, 303–313 (2008).

[96]. Bart M Nicolaï, Katrien Beullens, Els Bobelyn, Ann Peirs, Wouter Saeys, Karen I Theron and Jeroen Lammertyn. *Nondestructive measurement of fruit and vegetable quality by means of NIR spectroscopy: A review.* Postharvest Biology and Technology **46**, 99–118 (2007).

[97]. Marzena Jamrógiewicz. *Application of the near-infrared spectroscopy in the pharmaceutical technology.* Journal of pharmaceutical and biomedical analysis **66**, 1–10 (2012).

[98]. J Luypaert, DL Massart and Y Vander Heyden. *Near-infrared spectroscopy applications in pharmaceutical analysis.* Talanta **72**, 865–883 (2007).

[99]. Turgut Durduran, Regine Choe, WB Baker and AG Yodh. *Diffuse optics for tissue monitoring and tomography.* Reports on Progress in Physics **73**, 076701 (2010).

[100]. Paola Taroni, Antonio Pifferi, Giovanna Quarto, Lorenzo Spinelli, Alessandro Torricelli, Francesca Abbate, Anna Villa, Nicola Balestreri, Simona Menna, Enrico Cassano et al. *Noninvasive assessment of breast cancer risk using time-resolved diffuse optical spectroscopy.* Journal of biomedical optics **15**, 060501–060501 (2010).

[101]. Davide Contini, Lucia Zucchelli, Lorenzo Spinelli, Matteo Caffini, Rebecca Re, Antonio Pifferi, Rinaldo Cubeddu and Alessandro Torricelli. *Review: Brain and muscle near infrared spectroscopy/imaging techniques.* Journal of Near Infrared Spectroscopy **20**, 15–27 (2012).

[102]. Antonio Pifferi, Andrea Farina, Alessandro Torricelli, Giovanna Quarto, Rinaldo Cubeddu and Paola Taronia. *Review: Time-domain broadband near infrared spectroscopy of the female breast: a focused review from basic principles to future perspectives.* Journal of Near Infrared Spectroscopy **20**, 223–235 (2012).

[103]. Martin Wolf, Marco Ferrari and Valentina Quaresima. *Progress of near-infrared spectroscopy and topography for brain and muscle clinical applications.* Journal of biomedical optics **12**, 062104–062104 (2007).

[104]. Buhong Li, Zhihai Qiu and Zheng Huang. *Advanced optical techniques for monitoring dosimetric parameters in photodynamic therapy.* In

Photonics Asia pp 85530F–85530F. International Society for Optics and Photonics (2012).

[105]. Satoru Tsuchikawa. *A review of recent near infrared research for wood and paper.* Applied Spectroscopy Reviews **42**, 43–71 (2007).

[106]. Satoru Tsuchikawa and Manfred Schwanninger. *A review of recent near-infrared research for wood and paper (part 2).* Applied Spectroscopy Reviews **48**, 560–587 (2013).

[107]. RAJ Groenhuis, H.A. Ferwerda and J.J.T. Bosch. *Scattering and absorption of turbid materials determined from reflection measurements. 1: Theory.* Applied Optics **22**, 2456–2462 (1983).

[108]. S.T. Flock, M.S. Patterson, B.C. Wilson and D.R. Wyman. *Monte Carlo modeling of light propagation in highly scattering tissues. I. Model predictions and comparison with diffusion theory.* Biomedical Engineering, IEEE Transactions on **36**, 1162–1168 (1989).

[109]. Thomas J Farrell, Michael S Patterson and Brian Wilson. *A diffusion theory model of spatially resolved, steady-state diffuse reflectance for the noninvasive determination of tissue optical properties invivo.* Medical physics **19**, 879–888 (1992).

[110]. F. Martelli and G. Zaccanti. *Calibration of scattering and absorption properties of a liquid diffusive medium at NIR wavelengths. CW method.* Optics express **15**, 486–500 (2007).

[111]. U.J. Netz, I. Gersonde, J. Toelsner and G. Illing. *Frequency domain diffuse fluorescence tomography for detection of deep lesions.* In *European Conference on Biomedical Optics.* Optical Society of America (2011).

[112]. J. Stott and D.A. Boas. *A practical comparison between time-domain and frequency-domain diffusive optical imaging systems.* In *Biomedical Topical Meeting.* Optical Society of America (2002).

[113]. Vasilis Ntziachristos and Britton Chance. *Accuracy limits in the determination of absolute optical properties using time-resolved NIR spectroscopy.* Medical physics **28**, 1115 (2001).

[114]. Skytte J.L. *2D Static Light Scattering for Dairy Based Applications.* PhD thesis, Denmark Technical University (2014).

[115]. C.L. Crofcheck, F.A. Payne and M.P. Mengüç. *Characterization of milk properties with a radiative transfer model.* Applied optics **41**, 2028–2037 (2002).

[116]. D. Álvarez, M. Castillo, YL Xiong and FA Payne. *Prediction of beef meat emulsion quality with apparent light backscatter extinction.* Food Research International **43**, 1260–1266 (2010).

[117]. Jianwei Qin and Renfu Lu. *Measurement of the absorption and scattering properties of turbid liquid foods using hyperspectral imaging.* Applied spectroscopy **61**, 388–396 (2007).

[118]. J. Qin and R. Lu. *Monte Carlo simulation for quantification of light transport features in apples.* Computers and electronics in agriculture **68**, 44–51 (2009).

[119]. Lihong Wang and Steven L Jacques. *Use of a laser beam with an oblique angle of incidence to measure the reduced scattering coefficient of a turbid medium.* Applied optics **34**, 2362–2366 (1995).

[120]. G. Marquez and LH Wang. *White light oblique incidence reflectometer for measuring absorption and reduced scattering spectra of tissue-like turbid media.* Opt. Express **1**, 454–460 (1997).

[121]. Shao-Pow Lin, Lihong Wang, Steven L Jacques and Frank K Tittel. *Measurement of tissue optical properties by the use of oblique-incidence optical fiber reflectometry.* Applied optics **36**, 136–143 (1997).

[122]. Kung-Bin Sung and Hsi-Hsun Chen. *Enhancing the sensitivity to scattering coefficient of the epithelium in a two-layered tissue model by oblique optical fibers: Monte Carlo study.* Journal of biomedical optics **17**, 107003–107003 (2012).

[123]. Janaka C Ranasinghesagara and Roger J Zemp. *Combined photoacoustic and oblique-incidence diffuse reflectance system for quantitative photoacoustic imaging in turbid media.* Journal of biomedical optics **15**, 046016–046016 (2010).

[124]. Alejandro Garcia-Uribe, Karthik Chinna Balareddy, Jun Zou and Lihong V Wang. *Micromachined fiber optical sensor for in vivo measurement of optical properties of human skin.* Sensors Journal, IEEE **8**, 1698–1703 (2008).

[125]. Alejandro Garcia-Uribe, Elizabeth B Smith, Jun Zou, Madeleine Duvic, Victor Prieto and Lihong V Wang. *In-vivo characterization of optical properties of pigmented skin lesions including melanoma using oblique incidence diffuse reflectance spectrometry.* Journal of biomedical optics **16**, 020501–020501 (2011).

[126]. H.C. Van De Hulst. *Multiple light scattering. Vols. _1_and_2.* Multiple light scattering. Vols. _1_and_2., by van de Hulst, HC. New York, NY (USA): Academic Press, 739 p. **1** (1980).

[127]. Jacob Lercke Skytte, Otto Højager Attermann Nielsen, Ulf Andersen, Jens Michael Carstensen, Anders Lindbjerg Dahl, Rasmus Larsen, Flemming Møller, Faisal Kamran and Jeppe Revall Frisvad. *Decomposition of Diffuse Reflectance Images-Features for Monitoring Structure in Turbid Media.* In *InsideFood Symposium* ().

[128]. Sara Sharifzadeh, Jacob L Skytte, Line H Clemmensen and Bjarne K Ersboll. *DCT-based characterization of milk products using diffuse reflectance images.* In *Digital Signal Processing (DSP), 2013 18th International Conference on* pp 1–6. IEEE (2013).

[129]. Nielsen O.H.A. *Broadband optical characterization of material properties.* PhD thesis, Denmark Technical University (2014).

[130]. Tobias Lindbergh, Marcus Larsson, Ingemar Fredriksson and Tomas Strömberg. *Reduced scattering coefficient determination by non-contact oblique angle illumination: methodological considerations.* In *Biomedical Optics (BiOS) 2007* pp 64350I–64350I. International Society for Optics and Photonics (2007).

[131]. Jorge Ripoll, Doreen Yessayan, Giannis Zacharakis and Vasilis Ntziachristos. *Experimental determination of photon propagation in highly absorbing and scattering media.* JOSA A **22**, 546–551 (2005).

[132]. Jeppe Revall Frisvad, Niels Jørgen Christensen and Henrik Wann Jensen. *Predicting the Appearance of Materials Using Lorenz–Mie Theory.* In *The Mie Theory* pp 101–133. Springer (2012).

[133]. J.R Frisvad. Lorenz-Mie theory based calculation. http://www.imm.dtu.dk/~jerf/code/ (2012). [Online; accessed 01-Dec-2013].

[134]. AJ Jääskeläinen, K-E Peiponen and JA Räty. *On reflectometric measurement of a refractive index of milk.* Journal of dairy science **84**, 38–43 (2001).

[135]. Otto Højager Attermann Nielsen, Arman Ahamed Subash, Frederik Donbæk Nielsen, Anders Bjorholm Dahl, Jacob Lercke Skytte, Stefan Andersson-Engels and Dmitry Khoptyar. *Spectral characterisation of dairy products using photon time-of-flight spectroscopy.* Journal of Near Infrared Spectroscopy **21**, 375–383 (2013).

[136]. Srinivasa G Narasimhan, Mohit Gupta, Craig Donner, Ravi Ramamoorthi, Shree K Nayar and Henrik Wann Jensen. *Acquiring scattering properties of participating media by dilution.* ACM Transactions on

Graphics (TOG) **25**, 1003–1012 (2006).

[137]. Tomas Svensson, Romolo Savo, Erik Alerstam, Kevin Vynck, Matteo Burresi and Diederik S Wiersma. *Exploiting breakdown of the similarity relation for diffuse light transport: simultaneous retrieval of scattering anisotropy and diffusion constant.* Optics letters **38**, 437–439 (2013).

[138]. Erik Alerstam and Tomas Svensson. *Observation of anisotropic diffusion of light in compacted granular porous materials.* Physical Review E **85**, 040301 (2012).

[139]. Alerstam E. *Optical spectroscopy of turbid media: time-domain measurements and accelerated Monte Carlo modelling.* PhD thesis, LUND University (2011).

[140]. Tomas Svensson, Erik Alerstam, Dmitry Khoptyar, Jonas Johansson, Staffan Folestad and Stefan Andersson-Engels. *Near-infrared photon time-of-flight spectroscopy of turbid materials up to 1400 nm.* Review of scientific instruments **80**, 063105–063105 (2009).

[141]. Svensson. T. *Pharmaceutical and Biomedical Applications of Spectroscopy in the Photon Migration Regime.* PhD thesis, LUND university. (2008).

[142]. Abrahamsson. C. *Time-Resolved Spectroscopy for Pharmaceutical Applications.* PhD thesis, LUND university. (2005).

[143]. Dmitry Khoptyar, Arman Ahamed Subash, Sören Johansson, Muhammad Saleem, Anders Sparén, Jonas Johansson and Stefan Andersson-Engels. *Broadband photon time-of-flight spectroscopy of pharmaceuticals and highly scattering plastics in the VIS and close NIR spectral ranges.* Optics Express **21**, 20941–20953 (2013).

[144]. Becker & Hickl Gmbh. *The bh TCSPS Handbook.* Berlin, Germany, 5 ed., (2012).

[145]. Otto Højager Attermann Nielsen, Frederik Donbæk Nielsen, Carsten Lilholt Thomsen, Stefan Anderson-Engels and Dmitry Khoptyar. Evaluation of the ID220 single photon avalanche diode for extended the spectral range of photon time-of-flight spectroscopy. Technical report Technical University of Denmark (2014).

[146]. Makoto Otsuka. *Comparative particle size determination of phenacetin bulk powder by using Kubelka–Munk theory and principal component regression analysis based on near-infrared spectroscopy.* Powder technology **141**, 244–250 (2004).

[147]. Jonas Johansson, Staffan Folestad, Mats Josefson, Anders Sparén, Christoffer Abrahamsson, Stefan Andersson-Engels and Sune Svanberg. *Time-resolved NIR/Vis spectroscopy for analysis of solids: Pharmaceutical tablets.* Applied spectroscopy **56**, 725–731 (2002).

[148]. Christoffer Abrahamsson, Jonas Johansson, Stefan Andersson-Engels, Sune Svanberg and Staffan Folestad. *Time-resolved NIR spectroscopy for quantitative analysis of intact pharmaceutical tablets.* Analytical chemistry **77**, 1055–1059 (2005).

[149]. Dmitry Khoptyar, AA Subash, M Saleem, O H Attermann Nielsen and Stefan Andersson-Engels. *Wide-bandwidth photon time of flight spectroscopy for biomedical and pharmaceutical applications.* In *16th International Conference on Near Infrared Spectroscopy* pp 661–665 (2013).

[150]. Tomas Svensson, Erik Alerstam, Margrét Einarsdóttír, Katarina Svanberg and Stefan Andersson-Engels. *Towards accurate in vivo spectroscopy of the human prostate.* Journal of Biophotonics **1**, 200–203 (2008).

[151]. M Mazurenka, L Di Sieno, G Boso, D Contini, A Pifferi, A Dalla Mora, A Tosi, H Wabnitz and R Macdonald. *A non-contact time-domain scanning brain imaging system: first in-vivo results.* In *European Con-*

ferences on Biomedical Optics pp 87990L–87990L. International Society for Optics and Photonics (2013).

[152]. Huabei Jiang, Joseph Pierce, Jeffrey Kao and Eva Sevick-Muraca. *Measurement of particle-size distribution and volume fraction in concentrated suspensions with photon migration techniques.* Applied optics **36**, 3310–3318 (1997).

[153]. SM Richter and EM Sevick-Muraca. *Characterization of concentrated colloidal suspensions using time-dependent photon migration measurements.* Colloids and Surfaces A: Physicochemical and Engineering Aspects **172**, 163–173 (2000).

[154]. Sarabjyot Singh Dali, John C Rasmussen, Yingqing Huang, Ranadhir Roy and Eva M Sevick-Muraca. *Particle sizing in dense suspensions with multiwavelength photon migration measurements.* AIChE journal **51**, 1116–1124 (2005).

[155]. Tianshu Pan, Don Barber, David Coffin-Beach, Zhigang Sun and Eva M Sevick-Muraca. *Measurement of low-dose active pharmaceutical ingredient in a pharmaceutical blend using frequency-domain photon migration.* Journal of pharmaceutical sciences **93**, 635–645 (2004).

[156]. Zhenqi Shi and Carl A Anderson. *Scattering orthogonalization of near-infrared spectra for analysis of pharmaceutical tablets.* Analytical chemistry **81**, 1389–1396 (2009).

[157]. Rajesh R Shinde, GV Balgi, SL Nail and EM Sevick-Muraca. *Frequency-domain photon migration measurements for quantitative assessment of powder absorbance: A novel sensor of blend homogeneity.* Journal of pharmaceutical sciences **88**, 959–966 (1999).

[158]. SE Torrance, Z Sun and EM Sevick-Muraca. *Impact of excipient particle size on measurement of active pharmaceutical ingredient absorbance in mixtures using frequency domain photon migration.* Journal of pharmaceutical sciences **93**, 1879–1889 (2004).

[159]. Zhigang Sun, Sharnay Torrance, Fraser K McNeil-Watson and Eva M Sevick-Muraca. *Application of frequency domain photon migration to particle size analysis and monitoring of pharmaceutical powders.* Analytical chemistry **75**, 1720–1725 (2003).

[160]. M Blanco, J Coello, H Iturriaga, S Maspoch and N Pou. *Influence of the procedure used to prepare the calibration sample set on the performance of near infrared spectroscopy in quantitative pharmaceutical analyses.* Analyst **126**, 1129–1134 (2001).

[161]. A Sparén, O Svensson, M Hartman, M Fransson and J Johansson. *Matrix Effects in Quantitative Assessment of Pharmaceutical Tablets, Using Transmission Raman and NIR Spectroscopy.* Applied Spectroscopy **69**, pp (2015).

[162]. Heinz W Siesler, Yukihiro Ozaki, Satoshi Kawata and H Michael Heise. *Near-infrared spectroscopy: principles, instruments, applications.* Wiley. com (2008).

[163]. Andrey Bogomolov. *Multivariate process trajectories: capture, resolution and analysis.* Chemometrics and Intelligent Laboratory Systems **108**, 49–63 (2011).

[164]. L Eriksson, E Johansson, N Kettaneh-Wold and S Wold. *"PCA" and "PLS". Multi-and Megavariate Data Analysis using projection methods (PCA and PLS). Sweden: Umetrics AB. 1999. Pp. 41-108* ().

[165]. Åsmund Rinnan, Frans van den Berg and Søren Balling Engelsen. *Review of the most common pre-processing techniques for near-infrared spectra.* TrAC Trends in Analytical Chemistry **28**, 1201–1222 (2009).

[166]. Trevor Hastie, Robert Tibshirani, Jerome Friedman and James Franklin. *The elements of statistical learning: data mining, inference*

and prediction. The Mathematical Intelligencer **27**, 83–85 (2005).

[167]. MartinGeorg Ljungqvist, OttoHøjagerAttermann Nielsen, Stina Frosch, MichaelEngelbrecht Nielsen, LineHarder Clemmensen and BjarneKjær Ersbøll. *Hyperspectral imaging based on diffused laser light for prediction of astaxanthin coating concentration.* Machine Vision and Applications **25**, 327–343 (2014).

[168]. Abraham Savitzky and Marcel JE Golay. *Smoothing and differentiation of data by simplified least squares procedures.* Analytical chemistry **36**, 1627–1639 (1964).

[169]. P Geladi, D MacDougall and H Martens. *Linearization and scatter-correction for near-infrared reflectance spectra of meat.* Applied spectroscopy **39**, 491–500 (1985).

[170]. RJ Barnes, MS Dhanoa and Susan J Lister. *Standard normal variate transformation and de-trending of near-infrared diffuse reflectance spectra.* Applied spectroscopy **43**, 772–777 (1989).

[171]. André Liemert and Alwin Kienle. *Infinite space Green's function of time-dependent radiative transfer equation.* Journal of Physics A: Mathematical and General (2011).

[172]. JCC Day, R Bennett, B Smith, C Kendall, J Hutchings, GM Meaden, C Born, S Yu and N Stone. *A miniature confocal Raman probe for endoscopic use.* Physics in medicine and biology **54**, 7077 (2009).

Paper I

Non-invasive assessment of dairy products using spatially resolved diffuse reflectance spectroscopy

Otto H. A. Nielsen, Faisal Kamran, Anders B. Dahl, Jacob L. Skytte, Frederik D. Nielsen, Carsten L. Thomsen, Peter E. Andersen, Rasmus Larsen, Jeppe R. Frisvad.

₁ **Non-invasive Assessment of Dairy Products Using Spatially Resolved Diffuse**
₂ **Reflectance Spectroscopy**

₃ Otto H. A. Abildgaard,[1] Faisal Kamran,[2] Anders B. Dahl,[1] Jacob L. Skytte,[1] Frederik D.
₄ Nielsen,[3] Carsten L. Thomsen,[3] Peter E. Andersen,[2] Rasmus Larsen,[1] and Jeppe R. Frisvad[1, *]

₅ [1]*Department of Applied Mathematics and Computer Science,*
₆ *Technical University of Denmark, 2800 Kgs. Lyngby, Denmark*
₇ [2]*Department of Photonics Engineering, Technical University of Denmark, 4000 Roskilde, Denmark*
₈ [3]*NKT Photonics A/S, Blokken 84, 3460 Birkerød, Denmark*

₉ **ABSTRACT**

₁₀ **The quality of a dairy product is largely determined by its microstructure which also**
₁₁ **affects its optical properties. In this way, an assessment of the optical properties during pro-**
₁₂ **duction may be part of a feedback system for ensuring the quality of the production process.**
₁₃ **In this paper, we investigate the use of a camera based measurement technology which allows**
₁₄ **quantification of both the reduced scattering coefficient and absorption coefficient. We base**
₁₅ **our measurements on hyperspectral images of diffuse reflectance in the wavelength range**
₁₆ **of 470 nm - 1020 nm. We measure the optical properties of commercial available milk and**
₁₇ **yoghurt products with three different levels of fat content which constitute a relevant range**
₁₈ **of products at a dairy plant. The measured reduced scattering properties of the samples**
₁₉ **are presented, and show a clear discrimination between levels of fat contents as well as fer-**
₂₀ **mentation. Our measurement technique and method of analysis is thus suitable for a rapid,**
₂₁ **non-contact and non-invasive inspection that can deduce physically interpretable properties.**
₂₂ **Because the measurements are performed without the need for sample extraction and di-**
₂₃ **lution the inspection technology is suitable for in-line inspection during production of milk**
₂₄ **gels, for example.**

₂₅ Index Headings: **Oblique incidence; Diffuse reflectance; Absorption; Reduced scattering;**
₂₆ **Milk; Yoghurt; Fermentation; Non-invasive; Dairy.**

INTRODUCTION

₂₈ Monitoring microstructures in food and beverages is a key to enhancing manufacturing pro-
₂₉ cess flexibility and efficiency, while also improving the quality and safety of the products.[1,2] For
₃₀ yoghurt products, the microstructure, as defined by Bijnen et al.,[1] is a central component in con-
₃₁ sumers' perception of mouthfeel and thus their acceptance of the product.[3] The microstructure is
₃₂ formed from an aggregation of protein during the fermentation process.[4] It is known that reduced
₃₃ scattering properties,[5] scattering phase function[6] and the speckle characteristics[7–9] are affected
₃₄ by the microstructure. Inspection tools which quantify any of these effects may therefore reduce
₃₅ manufacturing costs and improve product quality.[10,11]

₃₆ The reduced scattering properties can be calculated from steady-state diffuse reflectance mea-
₃₇ surements as demonstrated by Farrell et al.[12] This enables measurement of the reduced scattering

[*] Corresponding author: jerf@dtu.dk

C.1 Low dynamic intensity range of the captured images.[20,21]

C.2 Estimating the entry point.[20,21]

C.3 Laser speckle.[20]

C.4 Estimating the diffusion centre.[20,21]

C.5 Image size calibration.[21]

C.6 Image vignetting.[20]

C.7 Fitting the diffusion model.[15,21]

Table I. **Challenges in the use of camera-based OIR measurement reported in the literature.**

and absorption properties. However, this requires measurement of absolute intensities which is infeasible for in-line measurements.[13] To solve this problem, the technique has been modified by Wang and Jacques[14] into oblique incidence reflectometry (OIR). The requirement of absolute intensities is avoided by instead resolving both single and multiple scattering of the light. The drawback of using OIR is that the range of optical properties which can be inspected, is limited directly by the finite spatial resolution and the field of view of the detector system. This limits the ability to resolve optically dense or dilute media.

OIR has mainly been used for inspection of tissues, which span a relatively small range of optical properties.[15–18] Tissue measurements are obtained using a fibre probe. Such probes are convenient for measuring the skin properties of live subjects, but also limited to the small range of optical properties of skin. To make the measurement of a milk fermentation process more feasible, we must cover a wider range of optical properties.[5] This is most feasible with camera-based measurements which has a much higher spatial resolution, typically a few thousand detectors along the diagonal of a modern charged coupled device (CCD) in comparison to 12 for fibre probes.[18] The original OIR technique[14] was camera-based and demonstrated the potential of the technique for measuring the reduced scattering μ_s'. Measurement of the absorption coefficient μ_a and the spectral dependencies was not introduced until after the shift to systems based on fibre probes.[15,19] Some work has been done in camera-based OIR,[20,21] where the challenges summarised in Table I were identified. We refer to these using the markers **C.1** to **C.7**.

Our objective in this paper is to demonstrate an inspection tool for quantifying the reduced scattering properties as well as the absorption properties of dairy products suitable for in-line process inspection. To ensure industrial relevance, our inspection tool is applied to commercial available milk and yoghurt products with three different levels of fat content. In comparison to previous camera-based instruments for measuring OIR, ours provide spectrally resolved measurements. We describe how the challenges listed above occur in our measurement method and how they are solved. We handle the challenges in a sample independent manner, so that they are directly transferable to other applications. Finally, the reduced scattering properties that we measure show a clear distinction between fermented and commercial milk which is promising for future in-line inspection of the milk fermentation process.
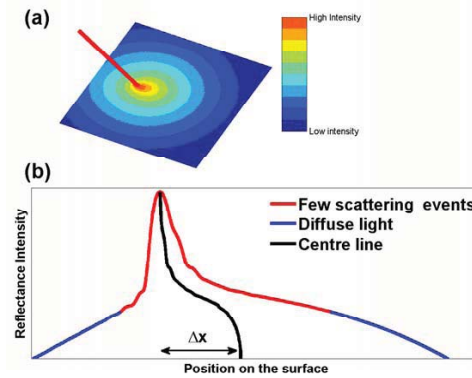
3

Figure 1. Illustration of measurement principle in OIR. **(a)** Illustrates reflectance intensity from a sample's surface illuminated by a laser beam (red line). **(b)** Illustration of the reflectance from the sample along the entry direction and through the entry point. The profile is asymmetric and shifts by a distance Δx from top to bottom.

RELATED WORK

The measurement principle of OIR is illustrated in Figure 1. In Figure 1 (a), the light beam is obliquely incident on the sample surface. Inside the sample the light is scattered in different directions, and some emerge from the surface as diffuse reflectance. The highest intensity is closest to the entry point, and the intensity declines further away. Most of the reflectance can be described as two components, and this is illustrated in Figure 1 (b). Here, a profile of the reflectance values is illustrated; the line goes through the entry point in the direction of the incident beam. The first component (red) is most intense. This is a region where light has only experienced a few scattering events. The second component (blue) is the low-intensity contribution far from the entry point. This is the region where the reflectance may be described by a diffusion process. Because light enters the sample at an oblique angle the reflectance profile is elongated, more light is emitted from the forward direction. This is seen from the so-called centre line between the two sides of the reflectance profile, marked by a black line in Figure 1 (b). The centre line is the geometrical centre of the reflectance profile for different intensity levels. At high intensities, the line is located at the entry point, and at low intensities the line is shifted forward towards a new location. The displacement of the two symmetry points for the reflectance profile is denoted Δx.

In OIR the relation between Δx and the light transport diffusion coefficient D is modelled as follows:[15]

$$D = \frac{\Delta x}{3 \sin \theta_t} = \frac{n \Delta x}{3 \sin \theta_i} \quad , \tag{1}$$

where θ_t is the angle of refraction, and this depends on the angle of incidence θ_i and the relative index of refraction n as specified by the law of refraction (Snell's law). The relative index of refraction is $n = n_{\text{sample}}/n_{\text{ambient}}$. In the present work, the surrounding medium is air ($n_{\text{ambient}} = 1$)
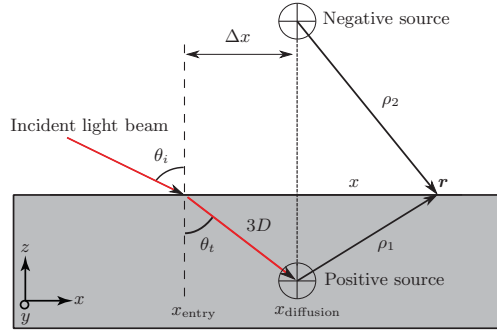
4

Figure 2. Schematic presentation of OIR. The incoming light is refracted at the sample surface. The model describes the emergent intensity of light at the point **r** as a sum of contributions from a positive and a negative point source at distances ρ_1 and ρ_2. The two point sources are shifted horizontally by a distance Δx from the entry point of the light.

89 and the refractive index of milk is assumed to be 1.347.[22] D may also be related to the transport
90 mean free path (mfp') as $3D \approx 1$mfp', which gives the simple interpretation that light on average
91 travels this distance into the sample before being scattered.[15]

It has been found, by comparison with Monte Carlo models,[15] that the diffusion coefficient can be expressed as

$$D \approx \frac{1}{3(\mu_s' + 0.35\mu_a)} \quad . \tag{2}$$

92 Here μ_s' and μ_a are the reduced scattering coefficient and the absorption coefficients respectively,
93 and this provides the first parametrisation of the optical properties. Equation 2 can be considered
94 a simplification of the expression for D reported by Ripoll et al.[23]

The light becomes diffuse as we move away from the point of entry. Therefore, the light is modelled using a displaced diffusion dipole as illustrated in Figure 2. We use the expression by Farrell et al.[12] but now with the dipole (the positive and negative point sources) shifted horizontally by the distance Δx and shifted toward the sample surface according to the modified expression for D. The diffuse reflectance at a point $\mathbf{r} = (x, y, z = 0)$ on the surface then becomes[15]

$$R(\mathbf{r}) = 3D\left(\mu_{\text{eff}}\rho_1 + 1\right)\frac{e^{-\rho_1\mu_{\text{eff}}}}{4\pi\rho_1^3}$$
$$+ (3D + 4AD)\left(\mu_{\text{eff}}\rho_2 + 1\right)\frac{e^{-\rho_2\mu_{\text{eff}}}}{4\pi\rho_2^3} \quad , \tag{3}$$

where ρ_1 and ρ_2 are the distances from the positive source and the negative source to the location **r** on the sample surface, μ_{eff} is the effective transport coefficient. These sources are positioned at vertical distances of $z_1 = 3D\cos\theta_t$ and $z_2 = z_1 + 4AD$. The parameter A corrects the position of the negative source to account for internal reflection from the boundary back into the sample. It is

5

approximated by[12]

$$A = \frac{1+F}{1-F} \qquad (4)$$

$$F = 0.0636n + 0.668 + 0.710n^{-1} - 1.440n^{-2} \quad . \qquad (5)$$

To measure the optical properties, we first find the diffusion coefficient D by estimating the distance between the entry point and the diffusion centre (Equation 1). We insert D in Eq. 3 and find μ_{eff} by a nonlinear least squares fit of the equation to measured data. Combining this, the optical properties may be deduced[15]:

$$\mu_{\text{a}} = D\mu_{\text{eff}}^{2} \qquad (6)$$

$$\mu_{\text{s}}' = (3D)^{-1} - 0.35\mu_{\text{a}} \quad . \qquad (7)$$

The technique thus imposes two criteria on the detection in relation to the optical properties of the sample

1. The reflectance profile must be resolved with sufficiently high resolution to expose the horizontal shift Δx.

2. The field of view must be sufficiently wide such that the light becomes diffuse enough to match the diffusion expression (3).

The range of optical properties that can be quantified robustly are therefore dependent on the detector system. One important aspect of the data collection is therefore that the reflectance profiles are completely resolved without saturated pixels. To accomplish this, together with a low noise measurement of the diffused light, the original implementation used two images of the reflectance. One images was taken with a neutral density filter to avoid saturation of the pixels close to the entry point. This had the undesirable side effect of shifting the position of the beam on the sample surface, which caused a systematic measurement error. Sun et al.[21] used only one image with no filter applied to the source. This limits the range of the optical properties which can be measured, as highly scattering samples may saturate the CCD and low scattering causes a low with noise.

With an image of the reflectance profile recorded, the calculation the of the light's entry point has been handled in different ways. In the original OIR technique,[14] the entry point is identified as the pixel of highest intensity. The pixel with highest intensity may however be a noisy estimate, especially in the presence of speckle which arises in narrow bandwidth systems. To improve the measurement precision, Sun et al.[21] used a weighted centre of mass of all pixels above the average intensity. Lindbergh et al.[20] used the most intense pixel, but after a convolution with a Gaussian filter. To reduce noise even further, the average value of five repetitive measurements was used.

Similarly, different approaches have been taken for calculation of the diffusion centre. It was originally estimated as the position at which the centre line for the reflectance profile converged,[14] see illustration in Figure 1 (b). For each point in the reflectance profile, the corresponding position on the other side is calculated by linear interpolation on a logarithmic scale of two points with the closets intensities above and below. The centre of the two positions, on opposite sides of the entry point, is added to the reflectance line. In this way, the centre line gives an estimation of the reflectance centre at different intensity levels of the profile. The diffusion centre is at the location where the centre line converges. However, camera based data requires a smoothing of this otherwise noisy profile. To improve the estimate of the diffusion centre, Sun et al.[21] used an iterative method. The location of the diffusion centre was moved as well as the region of the

image for which the diffusion fit was evaluated. Both were sequentially updated until a minimum change in the deduced optical properties was reached. The diffusion centre was calculated as the symmetry point for the reflectance profiles of two intervals positioned symmetrically around the previous diffusion centre. This iterative approach involves an additional nested loop for deducing the optical properties, and is thus slow. Lindbergh et al.[20] computed a number of threshold-filtered images, where the thresholds were different percentages of the maximum intensity. The diffusion centre was calculated as the evenly weighted centre of mass for the pixel above the threshold. The intensity levels are only used if the light is sufficiently diffuse. This was quantified by the ratio of two second order moments for pixels above the threshold. Working on the entire images with iterative or multiple thresholds is time expensive, and scales with the camera resolution to the power of two.

METHOD

In this section we describe our suggested solutions to the challenges of camera-based OIR (see the list of challenges in Table I).

Camera intensity range (C.1). To fully resolve the profiles we use high dynamic range imaging.[24] This means that we take several images of different exposure times and combine them into a single high dynamic range (HDR) image. We use the procedure described by Nielsen et al.[25] To ensure a linear response of the pixel value from the light intensity, the most intense pixels are interpreted as saturated. The actual value in these pixels is instead measured at a shorter exposure time using the HDR imaging.

Entry point and laser speckle (C.2 and C.3). To obtain an accurate estimate, we deduce a temporary centre position as the median coordinate of pixels above 40% of the maximum image intensity. Subsequently, we extract the reflectance profile along the direction of incidence for analysis. The angle of the horizontal axis in the image plane with the direction of incidence is measured during the assembly of the instrument, and the line is marked with black in Figure 3. Reflectance values along this line and the most intense pixel is the entry point. To reduce the noise of this estimate further, we use the average position over all wavelengths.

Estimating the diffusion centre (C.4). As in the work of Lin et al.[15] we use a single profile in the image rather than processing the entire image. However, due to the noise properties of the CCD, we found that it is necessary to extend Lin's work so that we can handle non-monotonously decreasing data. To obtain a high accuracy estimate of the diffusion centre, we capture the overall development of the centre line using a regularized quadratic spline. Splines are advantageous as they do not enforce a specific shape of centre lines as opposed to a closed expression. The regularisation ensures robustness against noise in the image data. Finally, due to the quadratic nature, its derivatives are smooth, which is ideal for estimating the convergence of the profiles towards the location of the diffusion centre. We calculate the diffusion centre as the position of the spline at which its derivative as function of intensity is zero. If the derivative is zero in more than one position, the one of the highest image intensity is chosen.

Examples of calculated centre lines as a function of intensity depth are presented in Figure 4 (a) each together with its associated spline marked with black. Considering that the centre lines consist of roughly 3.5 thousand points, the development as a function of intensity is fairly well defined. The derivative of the splines used for estimating the convergence is seen in Figure 4 (b). The diffusion centre is evaluated as the point at which the derivative of the spline first crosses zero. At lower intensity values, the centre line may be more subject to experimental factors such as sample roughness and unintended tilt between surface normal and camera axis.
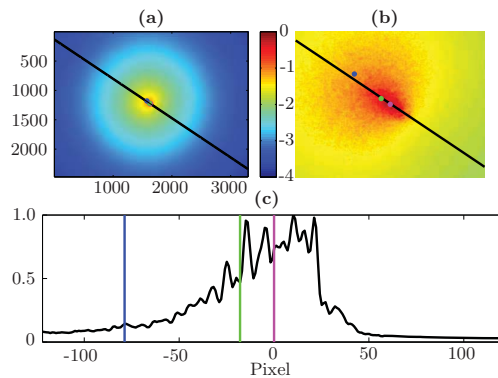
Figure 3. The centre estimation and line extracted from a HDR image of Arla Lærkevang® 1.5% fat at 750 nm. Intensity is normalised and the colormap uses a logarithmic scale. **(a)** HDR image, the blue marker is the centre determined with the method by Sun et al.,[21] and the green shows the results of using the method by Lindbergh et al.[20] The black line is the extracted line we use for estimation of the entry point marked with magenta. **(b)** Zoom in on the beams entry point in **(a)**. **(c)** The extracted reflectance profile together with the projected entry points from **(b)**.

CCD pixel calibration and vignetting (C.5 and C.6). As OIR relies on intensity and shape it is essential to characterise both lens distortion and vignetting. To quantify lens distortion, we place a calibration grid on top of a homogeneous scattering sample. The light beam illuminates the sample similar to a measurement. The diffuse reflectance effectively provides a background illumination of the grid as seen in Figure 5 (a). The image of the grid was enhanced by removing the smooth and diffuse part of the reflectance profile. This is done using a local noise normalization and dynamic range reduction of the image. From this the grid is annotated manually and the distance between points was fitted with a linear model. An example of the fit residual is presented in Figure 5 (b). This procedure is carried out at 480 nm, 650 nm and 970 nm. From this, it was found that the image distortion is less than two pixels across the entire field of view, which causes changes significantly below the measurement precession. Therefore we do not need any additional correction for lens distortion. The chromatic aberration, causing a wavelength-dependant image magnification, is quantified as less than 1%.

This approach is advantageous as it provides hyper spectral information and enables quantification of not only average pixel size but also possible image distortion.

To quantify the vignetting of the imaging system, an image is captured of a white paper poster smoothly illuminated by sunlight. The poster was positioned at a distance of around 1.5 meters from the lens so that it was completely out of focus. This measurement shows a drop of transmission through the lens to about 80 % toward the peripheral parts of the image. Traces of the vignetting signal are presented in Figure 5 (c). It is used to correct all images captured to measure optical properties.

Fitting the diffusion model (C.7). The last unanswered question for the evaluation of the fit is the area excluded around the entry point and diffusion centre. The reflected light in this area is interpreted as being insufficiently diffuse to be described by the diffusion equation. As noted by
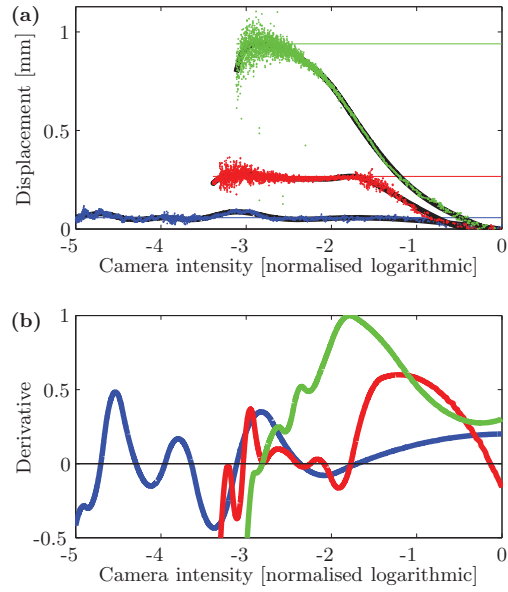
Figure 4. *Calculation of diffusion centres for Arla A38® 3.5% at 500 nm (blue), Arla Lærkevang® 1.5% at 970 nm (red) and Arla Lærkevang® 0.5% at 970 nm (green). (a) The measured diffusion centre lines presented as dots and a spline presented as the black line through each. The position of the diffusion centre is marked as a vertical line. (b) The normalised derivative of the spline from the centre lines, these are used to calculate the convergence of the lines*

Lin et al.[15] an advantage of OIR is that the area may be quantified in units of the mfp', calculated from Δx (see Figure 2). Lin et al.[15] reports that the measured optical properties for low scattering samples are especially sensitive to this excluded area, and they used an area with a radius of 1.5 mfp'. Their work was based on fibre probes, which limited the possibility of a more general analysis. We have the means to do this due to the high spatial resolution of our camera-based instrumentation. The analysis is important in two regards:

K.I The previously suggested value may not be optimal

K.II How does the width of the excluded region affect the de-
duced optical properties?

Table II. **Objectives off investigating the data selection, previously refereed to as the foot print of the model.**[26]

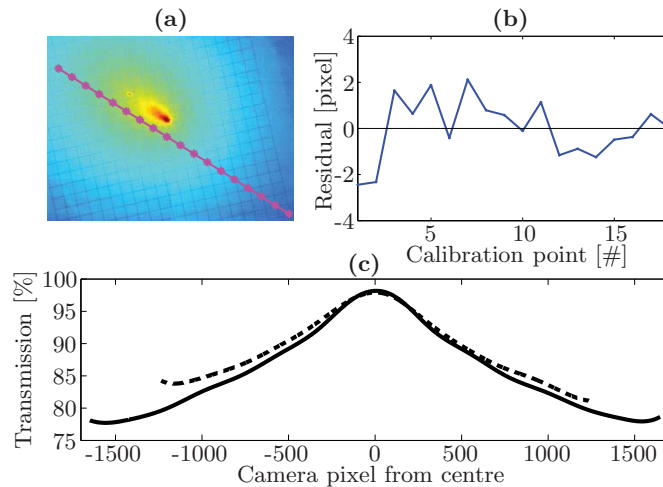We exclude the part of the reflectance profile which is too close to either the entry point or dif-

Figure 5. **(a)** Image of the calibration grid on a logarithmic scale. **(b)** Residual in pixel distance from the model. **(c)** Vignetting along the two camera axes through the centre.

fusion centre to be modelled as a diffusion process. This requirement is quantified in the following criterion:

$$\max \left(|x - x_{\text{Entry}}|, |x - x_{\text{Diffusion}}| \right) < \left(\kappa \cdot \text{mfp'} + 1.5 \cdot \omega_{\text{beam}} \right) \tag{8}$$

Here, x is a point along the line extracted from the image data as seen in Figure 3. The beam waist is denoted by ω_{beam}, and κ is the number of mfp', which is excluded and quantifies the width of the reflectance profiles not described by the diffusion approximation.

Measurement of the effective attenuation. The second parameter used for determining the optical properties is the effective attenuation (μ_{eff}), which is deduced from the shape of the diffused light by Eq. 3. The implementation by Lin et al.[27] report a minimization of the following expression, though without the beam convolution

$$\chi = \frac{1}{N} \sum_{n=1}^{N} \left(\frac{\int_{3 \cdot w_{\text{beam}}}^{-3 \cdot w_{\text{beam}}} R(x_n - x) dx - y_n}{y_n} \right)^2. \tag{9}$$

Here N denotes the number of points along the line of incidence, marked in black in Figure 3, which fulfil the criterion (8). R denotes the diffuse reflectance intensity calculated by Eq. 3, and is evaluated in position x_n. The integral over x is a convolution due to the finite beam size with waist w_{beam}. Lastly y_n denotes intensity at a given pixel. Using this expression, each pixel only contributes with an error relative to the magnitude of the intensity. The two optimal values are determined by minimization using the Levenberg-Marquardt algorithm.

Interpretation of optical properties. For the reduced scattering coefficients, the wavelength dependence is fitted with an approximation derived from Lorenz-Mie theory and presented by
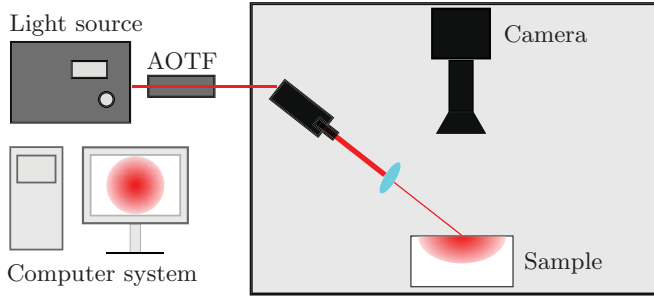
Figure 6. Illustration of our diffuse reflectance instrument. The supercontinuum laser generates a broad spectral light profile and the specific wavelengths transmitted are selected using an acousto optical filter (AOTF). The beam, is focused onto the sample using an achromat. Images are captured of the light reflectance profile by a CCD camera mounted above the sample.

Graaff et al.[28] We do this by fitting the model

$$\mu'_s = A\lambda^{-\beta} \tag{10}$$

Here λ is the wavelength in nm, A and β are fitted coefficients. The fitted amplitude coefficient A indicates the concentration of the scatterers and their scattering cross-section, and the decay rate β reflects the size parameter of the scatterers. In this way, wavelength resolved measurements of the reduced scattering coefficients enable discrimination between an increase in scattering particles density (A) from their size (β).

For the wavelength dependence of the absorption coefficients, we refer to the spectrum of water reported by Hale and Querry[29] and for milk fat reported by Michalski et al.[30]

MATERIALS

Hyperspectral imaging system. Figure 6 illustrates our instrument for OIR measurements. The instrument is based on acousto optical filtering of a broadband supercontinuum light source (SuperK Extreme EXW-12, NKT Photonics A/S, Birkerød, Denmark). The supercontinuum light source generates a beam throughout the spectral range from 450 nm to 2400 nm and for the present work, the acousto optical filter (SuperK SELECT, NKT Photonics A/S, Birkerød, Denmark) was equipped with a crystal that enables wavelength selection in the spectral range from 475 nm - 1020 nm. The optical bandwidth changes linearly from around 3.5 nm to roughly 16 nm. To accomplish this broad spectral range, the filtering amplitude is lowered in the wavelength range above 900 nm. The acousto optically filtered light is coupled into a fibre delivery system (VIS-nIR FDS, NKT Photonics A/S, Birkerød, Denmark). The combined instrument produces a collimated single mode beam with a tunable wavelength which is ideal for OIR.

The FDS provides a collimated beam, and the beam size is reduced further using a lens. To keep the lens and its mounting equipment outside the camera field of view, the beam is focus on the sample surface using a 38 mm focal length achromatic lens (Edmund Optics Inc., Barrington, New Jersey, USA). The waist of the beam is wavelength-dependent and grows from approximately

120 μm at 480 nm to 200 μm at 1000 nm; this includes the effect of the angular projection. The incidence angle of the beam is $\theta_i = 52°$, which was found as a compromise between increasing the diffusion displacement (Equation 1) while keeping the projected beam small and having transmission into the sample. A more detailed considerations for incidence angle and polarizations direction is provided by Abildgaard.[31]

Images of the reflectance profiles are captured using a 12-bit CCD camera (AM-800GE, JAI, Miyazaki, Japan) with a pixel resolution of 3296×2472. The imaging objective is a 50 mm focal length lens (LM50XC, Kowa Company Ltd., Nagoya, Japan), mounted to provide an image with a resolution of 3.2 μm per pixel of the sample surface. The shutter on the objective was set to F7 and magnification to 2. To calibrate the imaging system we used a calibration grid (R1L3S3p , Thorlabs, Gothenburg, Sweden).

Dairy samples. We evaluate the measurement technique based on a series of dairy products. This series contains commercially available milk and yoghurt with three different fat levels. The names of the products and key informations on their composition are presented in Table III. All products were purchased during December 2013 in Copenhagen, Denmark. The yoghurt products are fermented with the bacteria culture L. *acidophilus*. The milk and yoghurt products have very different structural properties, because the casein protein in yoghurts contain a gel network rather than being suspended individual micelles. The chemical composition in terms of fat and protein contents is largely unchanged, especially for the 1.5% products where the difference only is caused in the microstructure of the protein gel.

Products name	Fat		Protein	
	(g / 100g)	Mode (μm)	(g / 100g)	Mode (μm)
Arla Lærkevang® Sødmælk	3.5	0.99	3.5	0.046
Arla Lærkevang® Letmælk	1.5	0.99	3.5	0.046
Arla Lærkevang® Minimælk	0.5	0.99	3.5	0.052
Arla A38® naturel 3.5%	3.5		3.5	
Arla A38® naturel 1.5%	1.5		4	
Arla A38® naturel 0.5%	0.5		4.5	

Table III. **Product information for the dairy products. The size parameters are typical values and measured by a Mastersizer 3000 (Malvern, United Kingdom) evaluated with a refractive index of 1.529, the instrument does not support multiple constituents as is the case for milk. The corresponding values are not available on fermented milks as the necessary sample dilution destroys the gel network.**[32]

By inspecting the samples presented in Table III the instrument sensitivity is evaluated as the discrimination between the deduced optical properties of similar milk and yoghurt products. The measurement precision of all dairy products was quantified as the standard deviation between five repetitive measurements. To further investigate the correlation between the deduced scattering and absorption coefficient, the optical properties of Arla Lærkevang® 1.5% fat was measured 19 times and deduced using a value of $\kappa = 2$. The measurement series was performed with only 11 spectral bands.
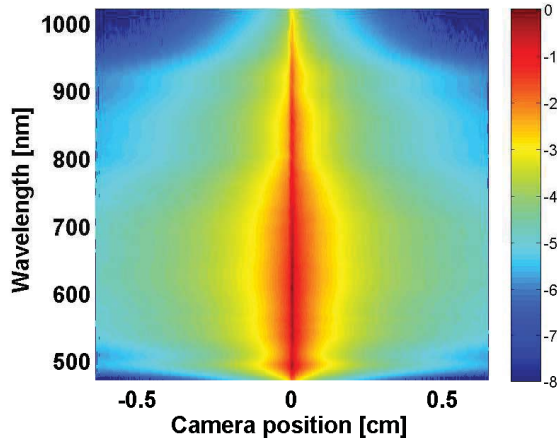
Figure 7. Combined spectrograph image of the reflectance profiles for Arla A38® naturel 3.5%. Colormap shows the reflectance intensity on 10 base logarithmic scale.

RESULTS

266

Hyperspectral imaging system (C.1). An example HDR image is presented in Figure 3 (a) which shows a smoothly changing profile across regions acquired with different exposure times. The HDR technique has previously been presented.[25] Lindbergh et al.[20] use a similar approach, but instead calibrate the response function to obtain HDR reflectance images. The data acquisition time is 1.9 seconds per wavelength for an HDR image. Since we deduce the optical properties from a line through the image, the entire hyperspectral information used to estimate the optical properties may be illustrated as a spectrograph image, see Figure 7. The image data is normalised to the most intense pixel over the entire spectrum. Spectrograph images may be used to assess the dynamic of the instrument, where it is seen that the signal is preserved throughout the entire spectrum. It also shows that the dynamic range of intensities for this dairy product spans 80 dB. The broad dynamic range can not be covered by any CCD chip and the measurements are only possible due to the HDR procedure.

Estimating the entry point (C.2 and C.3). For the present instrument and samples the speckle structure seen in Figure 3 surrounds the entry point. The entry points estimated with the methods proposed Lindberg et al.[15] and Sun et al.[21] are presented in Figure 3 together with the result of our method. It is evident that previous proposed methods overshoot along the incidence direction and is a general effect on our measurements of dairy products. This is because the previously proposed methods rely on estimating the centres of symmetric distributions. This causes an underestimation of Δx and leads to an overestimation of the scattering coefficient and underestimation of the absorption coefficient.

Fitting the diffusion model (C.7). It has previously been reported that the deduced optical properties depend on the range of the fit interval.[15] To investigate the significance of this effect on

13
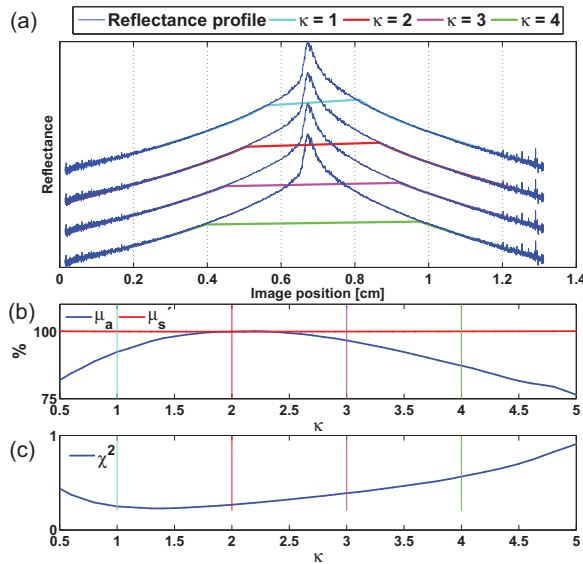
Figure 8. Example of how the foot print affects the fit for Arla A38® naturel 0.5% at 970 nm. **(a)** Examples of the fitted profiles in colour. **(b)** Deduced absorption coefficient (red) and reduced scattering (blue). **(c)** Fit residuals.

the dairy samples, we quantify the deduced optical properties and the fit residual when altering the width of the excluded data during the fit to Eq. 9. The value of κ is varied in the range $0.5 - 5$ and the effect on both the deduced optical properties and fit residual is investigated. An example is presented in Figure 8.

Measurement reproducibility. A scatter plot of the deduced optical properties is presented in Figure 9 for a single wavelength.

Spectra for dairy samples. To investigate the performance of the combined instrument and analysis technique in characterising the optical properties of dairy products, we measure the optical properties of the samples in Table III. The resulting curve fits for some of the most diverse reflectance profiles of the dairy products are presented in Figure 10, together with their respective fits. This gives an impression of how well the data is modelled with the proposed measurement technique. Measurement of all products was repeated 5 times, and the mean and standard deviation of the deduced optical properties are summarised in Figure 11. We continue to use $\kappa = 2$.

14
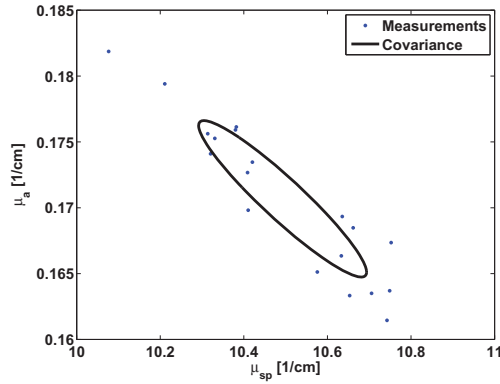
Figure 9. Scatterplot of the estimated optical properties of 19 repetitive measurements of milk 1.5 % fat at 930 nm, the ellipsoid shows the circle span by the eigenvalue decomposition of the data's covariance.
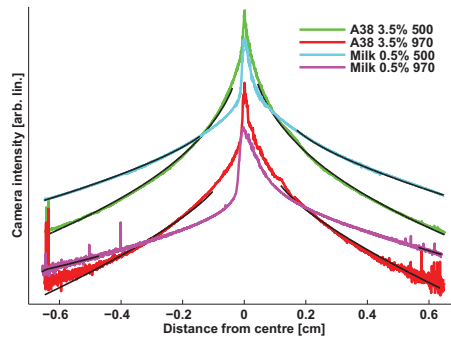
Figure 10. Examples of reflectance profiles and their fitted effective attenuation (black lines).

DISCUSSION

Hyperspectral imaging system (C.1). Our measurement procedure satisfies two important properties for an in-line inspection system. The measurement can be obtained through a cover slip, thus compatible with the hygiene requirements in dairy production. Another important aspect of the measurement technique is that the optical properties are measured in reflection mode, as opposed to transmission, which allows inspection of large volumes such as milk fermentation tanks. Furthermore, to the best of our knowledge, our instrument has the broadest spectral and spatial range presented so far in diffuse reflectance spectroscopy.[15,20,33]

With respect to data acquisition, the data acquisition at present time is 1.9 seconds per wavelengths, but may be reduced as the same shutter times are used for all wavelength and samples.

15
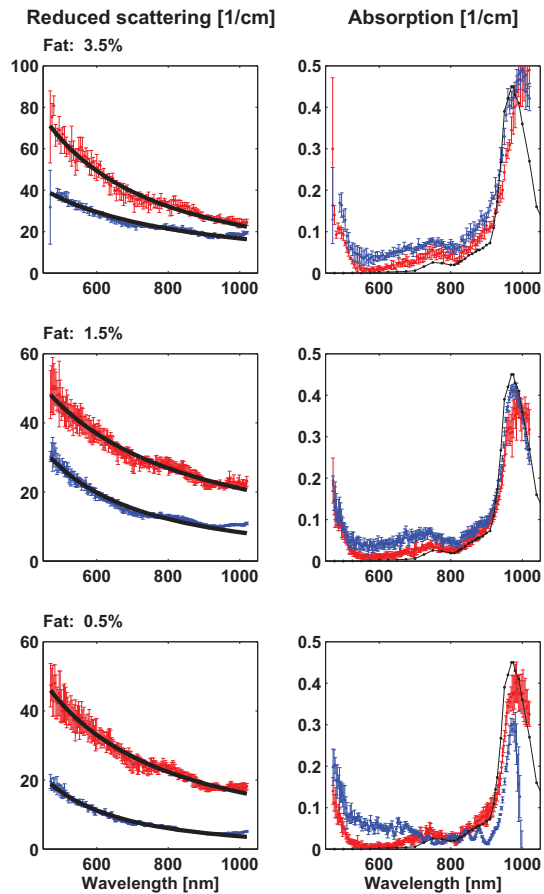
Figure 11. Measured optical properties for dairy products with 5 repetitive measurements showing the standard deviation at each wavelength. Red data is for fermented milk products, blue is for milk. For the reduced scattering coefficients, the black lines are fit to Eq. 10. For the absorption measurements, the black line is the absorption of water.[29]

From the spectrograph images as presented in Figure 7 it is evident that some of the long exposure shutter time for the wavelength range $550 - 900$ nm could be skipped as the signal for these is stronger. The short shutter time may be omitted for spectra in the blue and NIR range. Similarly the long shutter times could be omitted in the $500 - 800$ nm range. The measurement technique may also be carried out using an imaging spectrograph as conducted by Lin et al.[33] and Garcia-

Uribe et al.[16] In this way, the wavelength filtering is performed on the source side, avoiding the repetitive image acquisition with different wavelengths. Such a system can provide the full spectrogram image such as presented in Figure 7 in a single HDR image. Finally, the image may be used to identify absorption bands from the raw data directly. Absorption gives contraction of the reflectance profile over a short wavelength range, in Figure 7 an absorption band is present from around 950 nm and upwards. In comparison, the scattering causes a slow monotonous decay.

Estimating the entry point (C.2 and C.3). The speckle pattern shifts the location of the most intense pixel in two directions of the images, centred on the entry point. For the present measurement, the location of the most intense pixel shifts around by approximately 15 pixels. Previous methods for reducing the effects of the speckle rely on a symmetric shape of the reflectance and overshoot in the present data, see Figure 3 (c). This may in part be visible in our measurements because we investigate images of reflectance with such divers optical properties or because the milk samples are highly forward scattering. In any case, our method only searches for the most intense pixel along the line of incidence which reduces noise. Still, using the most intense point along this line is an estimation with high variance which is further reduced by averaging across wavelength. In this way, we obtain an unbiased estimate of the entry point in comparison to previous work.

Estimating the diffusion centre (C.4). By determining the diffusion centre from a single line of reflectance values instead of the entire image we gain two advantages. Firstly, it increases the range of optical properties which may be estimated. For samples with little scattering and absorption the asymmetric area of the reflectance is larger and 2D methods rely on convergence of the asymmetry within the image. The methods are thus limited by the field of view along the shortest side of the image. This limit was acknowledged by Lindbergh et al.[20] who excluded samples due to lack of dynamic range. The 1D method further extends the range, because the measurements may be conducted with the line of incidence along the diagonal of the image, which increases the number of pixels along the line. Secondly, the computation speed is significantly faster and scales better with the camera resolution.

Fit and foot print of the diffusion model (C.5 - C.6). The fit residual for a camera calibration presented in Figure 5 (b) clearly shows that the image distortion is not causing systematic dependence of the optical properties on the fit region presented in Figure 8. Nevertheless, a high precision method which we demonstrate for spectral characterization of the lens distortion is a necessary validation. Concerning the image vignetting, this effect is normalised after the images are captured. Nevertheless, the effect may be reduced by replacing the existing lens with a more expensive telecentric lens.

Fitting the diffusion model (C.7). With respect to fitting the diffusion model from Eq. 3 to the reflectance measurements, a disagreement has been reported by Chitchian and Fried.[34] This disagreement is not experienced on the measurements of the dairy samples, which exhibit a good visual agreement for different values of κ as shown in Figure 8 and for the most diverse dairy products in Figure 10.

Concerning the fit range of the diffusion model, it has previously been reported that the optical properties depend on this.[15,21] As stated in **K.I** Table II, it is of interest to investigate whether a proper value for κ may be deduced. The visual agreement between fit and selected data from our results does not, however give clear indication of which value to choose; this is seen from the example in Figure 8. All values of κ seem to give a decent description of the data. Thus, we continue to investigate the dependence of κ as described in **K.II** Table II. The results show that the dependence on κ is not trivial. As seen from the example presented in Figure 8 the deduced absorption and fit residual do not converge at large values of κ. Neither does a single value of κ exist at which the fit residual is minimised and absorption maximized, this might otherwise be a

₃₆₅ criterion for finding an optimal value of κ.

₃₆₆　　As seen from Figure 8 (b), the deduced absorption coefficient depends on the region where
₃₆₇ the data is fitted. The deduced absorption changes smoothly, and reaches maximum at κ = 2.2.
₃₆₈ The reduced scattering on the other hand is largely unchanged. Concerning the fit residual, the
₃₆₉ corresponding dependences on κ is presented in Figure 8 (C). It is noteworthy that the minimum
₃₇₀ fit error occurs at κ = 1.4, which is different from where the absorption peaks. These effects
₃₇₁ have been investigated across wavelength and sample. In general it was found that the reduced
₃₇₂ scattering coefficient is independent of κ, as seen on Figure 8. The deduced absorption coefficient
₃₇₃ does, however, depend on κ, but does not in general have a maximum.

₃₇₄　　One reason for these dependencies on the fit region is the analytical expression (Equation 3)
₃₇₅ which is known to break down in two regimes: highly anisotropic scattering phase function[35,36]
₃₇₆ and high absorption.[37] Recently, corrections have been proposed to include phase function depen-
₃₇₇ dencies by Zemp.[26] In addition, an improved analytical solution to the radiative transfer equation
₃₇₈ for a semi-infinite medium has recently been proposed by Liemert et al.[38] These two approaches
₃₇₉ may individually reduce the coupling between the optical properties. A combination of these ap-
₃₈₀ proaches may provide a more general and adequate numerical model that describes the optical
₃₈₁ properties.

₃₈₂　　A final remark on the dependence on fit range (κ) is that the specific value mainly influences
₃₈₃ the absorption coefficient which is important when the measurements are used for chemometric
₃₈₄ evaluation of the sample constituent. For the purpose of quantifying the reduced scattering co-
₃₈₅ efficient, and hence the particle size distribution which are change during milk fermentation, the
₃₈₆ specific value of κ is not essential.

₃₈₇　　**Measurement reproducibility.** The results are presented in Figure 9. Here it is seen that the
₃₈₈ noise contribution in scattering and absorption is highly correlated. The correlation coefficient is
₃₈₉ −0.94, which indicates high correlation. We believe that the systematic variations are largely in-
₃₉₀ duced through the estimation of the diffusion displacement. This error then propagates on through
₃₉₁ the curve fitting procedure, where the estimated effective attenuation compensates for the error in
₃₉₂ mean free path estimation. This strong correlation between the optical properties is commonly
₃₉₃ recognised.[37,39] The results suggests, that the method can become a high precision method for es-
₃₉₄ timation of the optical properties if the source of error in mean free path estimation can be reduced
₃₉₅ further.

₃₉₆　　**Spectra for dairy products.** Firstly, the fit results presented in Figure 10 demonstrate the fit
₃₉₇ performance for the investigated dairy products. These results show a fairly good characterisation
₃₉₈ of the reflectance profiles across both the diverse milk and yoghurt samples and the wavelength
₃₉₉ range from blue to NIR. However, it is evident that the amount of data to fit the diffusion model
₄₀₀ with milk 0.5 % is somewhat limited.

₄₀₁　　The measured reduced scattering coefficient, shown in Figure 11, increases as a function of fat
₄₀₂ contents. This is as expected since fat particles are the main cause for scattering. Similar results
₄₀₃ have been reported for other measurement techniques.[5,33]

₄₀₄　　Concerning the discrimination of the structural difference between milk and fermented milk
₄₀₅ products, the evaluated optical properties of the dairy samples are compared directly in Figure
₄₀₆ 11. From this, it is seen that the reduced scattering properties provide a clear distinction between
₄₀₇ the two products. Furthermore, it is seen that the values are in agreement with the approximate
₄₀₈ development derived from Lorenz-Mie theory and previously reported by Nielsen et al.[5] The mea-
₄₀₉ surement precision of the fermented products is in general lower than the milk products, this is
₄₁₀ due to their deflation and slightly curved surface.

₄₁₁　　The measured absorption spectra, three peaks are present throughout all the measurements.

18

The first peak is around 520 nm and has previously been reported for milk fat,[30] the presence of a weak peak at 750 nm and a stronger peak at 970 nm have previously been observed for water.[29] In general, the results show a reduction of the measured absorption for the fermented products. This effect may be a result of the scattering phase function of the samples. This induces a cross-talk between the absorption and scattering properties. We believe the improved models for radiative transfer by Liemert et al.[38] or phasefunction corrected diffusion by Zemp[26] may be a solution. Lastly, with respect to the range of optical properties which may be covered, it is seen that the limited field of view for the present system reduces the absorption estimate for the Arla Lærkevang® Minimælk 0.5 % fat.

CONCLUSION

The development of new optical characterization techniques is of great interest for the dairy industry. In the present work, a camera based instrument for quantifying the optical properties of milk and fermented milk has been demonstrated. Measurements are performed by only quantifying light reflection from the sample surface, this makes it feasible for in-line measurements, despite large sample volume as in a milk fermentation tank. In addition, the technique enables a non-contact and non-invasive measurement, which is important for avoiding contamination and accomplishing an automated measurement system.

The instrument covers the broad spectral range from 470 nm - 1020 nm and thus covers the absorption bands of both milk fat and water together with the reduced scattering properties of the samples. The optical properties of commercially available milk and fermented milk has been reported and show strong capabilities of discriminating between initial and final state of fermented milk products by their reduced scattering coefficient. Simultaneously, the absorption coefficient clearly marks the presence of both fat and water but also a correlation to the scattering levels.

As future work, the in-line measurement of these optical properties during milk fermentation will be a high priority. In addition, we would like to continue the development of measurement precision using more advanced models for the reflectance profile. These can improve the instrument's suitability for material inspection in general.

ACKNOWLEDGEMENTS

---

1. F. G. C. Bijnen, H. van Aalst, P. Baillif, J. C. G. Blonk, D. Kersten, F. Kleinherenbrink, R. Lenke, and M. M. vander Stappen, "In-line structure measurement of food products," Powder Technology **124**, 188–194 (2002).
2. W. Labs, "Inline monitoring aids in food safety and quality: What you don't measure could kill your brand," Food Engineering Magazine **85**, 51–52, 54, 56–59 (2013).
3. T. Janhøj, C. B. Petersen, M. B. Frøst, and R. Ipsen, "Sensory and rheological characterization of low-fat stirred yogurt," Journal of Texture Studies **37**, 276–299 (2006).

4. M. Auty, M. Fenelon, T. Guinee, C. Mullins, and D. Mulvihill, "Dynamic confocal scanning laser microscopy methods for studying milk protein gelation and cheese melting," Scanning **21**, 299–304 (1999).

5. O. H. A. Nielsen, A. A. Subash, F. D. Nielsen, A. B. Dahl, J. L. Skytte, S. Andersson-Engels, and D. Khoptyar, "Spectral characterisation of dairy products using photon time-of-flight spectroscopy," Journal of Near Infrared Spectroscopy **21**, 375–383 (2013).

6. B. M. Agrawal and M. Mengüç, "Forward and inverse analysis of single and multiple scattering of collimated radiation in an axisymmetric system," International Journal of Heat and Mass Transfer **34**, 633 – 647 (1991).

7. M. Alexander and D. Dalgleish, "Dynamic light scattering techniques and their applications in food science," Food Biophysics **1**, 2–13 (2006).

8. S. Sharifzadeh, J. Skytte, L. Clemmensen, and B. Ersboll, "DCT-based characterization of milk products using diffuse reflectance images," in "The 18th International Conference on Digital Signal Processing (DSP)," (2013), pp. 1–6.

9. J. L. Skytte, O. H. A. Nielsen, U. Andersen, J. M. Carstensen, A. L. Dahl, R. Larsen, F. Møller, F. Kamran, and J. R. Frisvad, "Decomposition of diffuse reflectance images - features for monitoring structure in turbid media," Proceedings of the InsideFood Symposium 2013 (2013).

10. M. Navrátil, C. Cimander, and C.-F. Mandenius, "On-line multisensor monitoring of yogurt and filmjölk fermentations on production scale," Journal of Agricultural and Food Chemistry **52**, 415–420 (2004).

11. C. Soukoulis, P. Panagiotidis, R. Koureli, and C. Tzia, "Industrial yogurt manufacture: Monitoring of fermentation process and improvement of final product quality," Journal of Dairy Science **90**, 2641–2654 (2007).

12. T. J. Farrell, M. S. Patterson, and B. Wilson, "A diffusion theory model of spatially resolved, steady-state diffuse reflectance for the noninvasive determination of tissue optical properties in vivo," Medical Physics **19**, 879–888 (1992).

13. Y. Peng and R. Lu, "An lctf-based multispectral imaging system for estimation of apple fruit firmness. part 2. selection of optimal wavelengths and development of prediction models." Transactions of the ASAE **49**, 269–275 (2006).

14. L. Wang and S. L. Jacques, "Use of a laser beam with an oblique angle of incidence to measure the reduced scattering coefficient of a turbid medium," Applied Optics **34**, 2362–2366 (1995).

15. S.-P. Lin, L. Wang, S. L. Jacques, and F. K. Tittel, "Measurement of tissue optical properties by the use of oblique-incidence optical fiber reflectometry," Applied Optics **36**, 136–143 (1997).

16. A. Garcia-Úribe, J. Zou, M. Duvic, J. H. Cho-Vega, V. G. Prieto, and L. V. Wang, "*In vivo* diagnosis of melanoma and nonmelanoma skin cancer using oblique incidence diffuse reflectance spectrometry," Cancer Research **72**, 2738–2745 (2012).

17. A. Garcia-Úribe, K. Balareddy, J. Zou, and L. Wang, "Micromachined fiber optical sensor for in vivo measurement of optical properties of human skin," IEEE Sensors Journal **8**, 1698–1703 (2008).

18. A. Garcia-Úribe, E. B. Smith, J. Zou, M. Duvic, V. Prieto, and L. V. Wang, "In-vivo characterization of optical properties of pigmented skin lesions including melanoma using oblique incidence diffuse reflectance spectrometry," Journal of Biomedical Optics **16**, 020501–020501–3 (2011).

19. G. Marquez and L. Wang, "White light oblique incidence reflectometer for measuring absorption and reduced scattering spectra of tissue-like turbid media," Optics Express **1**, 454 (1997).

20. T. Lindbergh, M. Larsson, I. Fredriksson, and T. Strömberg, "Reduced scattering coefficient determination by non-contact oblique angle illumination: methodological considerations," Proceedings of SPIE, Optical Interactions with Tissue and Cells XVIII **6435**, 64350I–64350I–12 (2007).

21. P. Sun, X. Cao, R. Yang, F. Xie, J. Ding, and F. Zhang, "Basic research on determining optical properties of tissues in vivo by measuring diffuse reflectance with a charge-coupled device," Optica Applicata **3**, 541–555 (2011).

22. A. J. Jääskeläinen, K.-E. Peiponen, and J. A. Räty, "On reflectometric measurement of a refractive index of milk," Journal of Dairy Science **84**, 38–43 (2001).

23. J. Ripoll, D. Yessayan, G. Zacharakis, and V. Ntziachristos, "Experimental determination of photon propagation in highly absorbing and scattering media," Journal of the Optical Society of America A **22**, 546–551 (2005).

24. P. E. Debevec and J. Malik, "Recovering high dynamic range radiance maps from photographs," in "Proceedings of SIGGRAPH 97," (1997), pp. 369–378.

25. O. H. A. Nielsen, A. L. Dahl, R. Larsen, F. Møller, F. D. Nielsen, C. L. Thomsen, H. Aanæs, and J. M. Carstensen, "In depth analysis of food structures, hyperspectral subsurface laser scattering," in "Proceesings of Scandinavian Workshop on Imaging Food Quality, Ystad, Sweden," (2011), pp. 27–32.

26. R. J. Zemp, "Phase-function corrected diffusion model for diffuse reflectance of a pencil beam obliquely incident on a semi-infinite turbid medium," Journal of Biomedical Optics **18**, 067005–067005 (2013).

27. S.-P. Lin, "Oblique-incidence fiber-optic reflectometry for measuring absorption and scattering in turbid media," Master's thesis, Rice University (1996).

28. R. Graaff, J. G. Aarnoudse, J. R. Zijp, P. M. A. Sloot, F. F. M. de Mul, J. Greve, and M. H. Koelink, "Reduced light-scattering properties for mixtures of spherical particles: a simple approximation derived from mie calculations," Applied Optics **31**, 1370–1376 (1992).

29. G. M. Hale and M. R. Querry, "Optical constants of water in the 200-nm to 200-μm wavelength region," Applied Optics **12**, 555–563 (1973).

30. M.-C. Michalski, V. Briard, and F. Michel, "Optical parameters of milk fat globules for laser light scattering measurements," Le Lait **81**, 787–796 (2001).

31. O. H. A. Abildgaard, "Broadband optical characterization of material properties," Ph.D. thesis, Technical University of Denmark (2014).

32. W. J. Lee and J. A. Lucey, "Formation and physical properties of yoghurt," Asian-Aust. J. Anim. Sci. **23**, 1127–1136 (2010).

33. J. Qin, R. Lus, and Qin, "Measurement of the absorption and scattering properties of turbid liquid foods using hyperspectral imaging," Applied Spectroscopy **61**, 388–396 (2007).

34. S. Chitchian and N. M. Fried, "Near-ir optical properties of canine prostate tissue using oblique-incidence reflectometry," Photonic Therapeutics and Diagnostics VI **7548**, 75480Z–75480Z–6 (2010).

35. L. V. Wang and S. L. Jacques, "Source of error in calculation of optical diffuse reflectance from turbid media using diffusion theory," Computer Methods and Programs in Biomedicine **61**, 163 – 170 (2000).

36. A. Kienle, F. K. Forster, and R. Hibst, "Influence of the phase function on determination of the optical properties of biological tissue by spatially resolved reflectance," Optics Letters **26**, 1571–1573 (2001).

37. F. Martelli, S. Del Bianco, A. Ismaelli, and G. Zaccanti, *Light propagation through biological tissue and other diffusive media: theory, solutions, and software* (SPIE Press Bellingham, 2010).

38. A. Liemert and A. Kienle, "Exact and efficient solution of the radiative transport equation for the semi-infinite medium," Scientific Reports **3**, 1–7 (2013).

39. L. V. Wang and H.-I. Wu, *Biomedical Optics: Principles and Imaging* (Wiley, 2007).

Transmission near-infrared and photon time-of-flight spectroscopy in a comparative analysis of pharmaceuticals

Faisal Kamran, Otto H. A. Nielsen, Anders Sparén, Olof Svensson, Jonas Johansson, Stefan Andersson-Engels, Peter E. Andersen, Dmitry Khoptyar.

Transmission Near-Infrared (NIR) and Photon Time-of-Flight (PTOF) Spectroscopy in a Comparative Analysis of Pharmaceuticals

Faisal Kamran,[a,]* Otto H.A. Abildgaard,[b] Anders Sparén,[c] Olof Svensson,[c] Jonas Johansson,[c] Stefan Andersson-Engels,[d] Peter E. Andersen,[a,]* Dmitry Khoptyar[d]

[a] *Department of Photonics Engineering, Technical University of Denmark, Frederiksborg 399, 4000 Denmark*
[b] *Department of Informatics and Mathematical Modelling, DTU, Asmussens All 321, 2800 Denmark*
[c] *Department of Pharmaceutical Development, AstraZeneca R&D, Mölndal, SE-431 83, Sweden*
[d] *Department of Physics, Lund University, P. O. Box 118, Lund SE-221 00, Sweden*

We present a comprehensive study of the application of photon time-of-flight spectroscopy (PTOFS) in the wavelength range 1050–1350 nm as a spectroscopic technique for the evaluation of the chemical composition and structural properties of pharmaceutical tablets. PTOFS is compared to transmission near-infrared spectroscopy (NIRS). In contrast to transmission NIRS, PTOFS is capable of directly and independently determining the absorption and reduced scattering coefficients of the medium. Chemometric models were built on the evaluated absorption spectra for predicting tablet drug concentration. Results are compared to corresponding predictions built on transmission NIRS measurements. The predictive ability of PTOFS and transmission NIRS is comparable when models are based on uniformly distributed tablet sets. For non-uniform distribution of tablets based on particle sizes, the prediction ability of PTOFS is better than that of transmission NIRS. Analysis of reduced scattering spectra shows that PTOFS is able to characterize tablet microstructure and manufacturing process parameters. In contrast to the chemometric pseudo-variables provided by transmission NIRS, PTOFS provides physically meaningful quantities such as scattering strength and slope of particle size. The ability of PTOFS to quantify the reduced scattering spectra, together with its robustness in predicting drug content, makes it suitable for such evaluations in the pharmaceutical industry.

Index Headings: **Spectroscopy; Scattering measurements; Turbid media; Multiple scattering; Spectroscopy, condensed matter.**

INTRODUCTION

The manufacturing process of pharmaceutical materials involves high-quality requirements to ensure efficiency and patient safety. Process analytical technology has been defined by the United States Food and Drug Administration as a mechanism to design, analyze, and control pharmaceutical manufacturing processes.[1] Near-infrared spectroscopy (NIRS) is a powerful spectroscopic technique widely employed in the pharmaceutical industry to monitor different stages of the production process and to analyze the final products.[2–5] Since its successful online implementation by major pharmaceutical companies, NIRS has been widely used in critical stages of the pharmaceutical process for the characterization of raw materials, drying, blending, and tableting.[6]

Near-infrared spectroscopy allows relatively cheap, rapid, easy, and non-destructive measurements, without the need for sample preparation.[7] Its analytical power has been demonstrated in a number of qualitative and quantitative pharmaceutical applications.[8] Chemometric methods have been applied to NIR spectroscopic data by the pharmaceutical industry to determine drug contents,[9] polymorphic content,[10] and particle sizes of powders.[11,12] The key challenge in NIRS is to develop methods that not only are accurate enough to determine analytical parameters, such as content uniformity between different tablets, but also have an inherent robustness such that the prediction of concentration is insensitive to variations in, e.g., raw material particle size and batch quality.[13] The inherent high correlation of spectral shapes and thus difficulty and inability to distinguish the contributions from such parameters in NIRS spectra[14,15] require the development and maintenance of extensive calibration databases. NIRS transmission spectra depend on both the structural and chemical properties of the medium. Elastic scattering of near-infrared light in a pharmaceutical tablet dominates over absorption by several orders of magnitude. Thus, the NIR spectra are strongly susceptible to parameters related to light scattering. This makes independent determination of particle size of major importance.[16] Abrahamsson et al. have shown that predictions based on NIRS data were improved by correcting for scattering effects in the measured spectra.[17] A method that is insensitive to variations in the scattering properties of the medium is highly desirable. It is widely recognized[18] that reduced scattering coefficient can be significantly changed by variation in microstructure of turbid media. To correct for the influence of structural properties, NIR transmission spectra normally have to be preprocessed before they can be analyzed.[19,20]

Photon time-of-flight spectroscopy (PTOFS)[17] is a spectroscopic technique in which the temporal distribution of photon propagation times through samples is measured. It provides less interdependent information on reduced scattering (influenced by the structural properties) and absorption (influenced by the chemical composition) of a turbid medium. PTOFS is becoming increasingly popular in broadband instruments.[21–23] The technique has been used specifically for the inspection
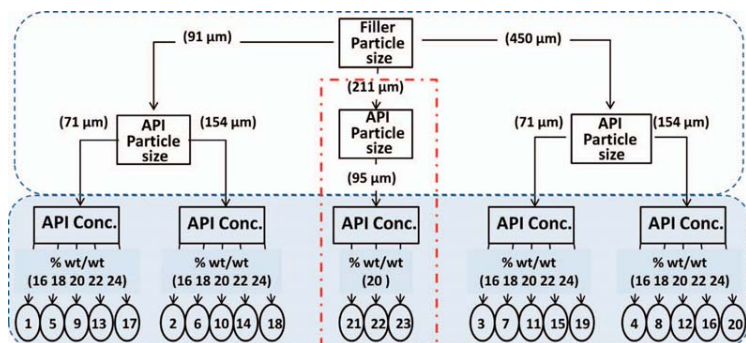
FIG. 1. Overview of the experimental design of the study. The upper section shows the various particle sizes, and the lower shaded section the variation in API concentration. The red rectangle indicates tablets with the center points introduced for the factors studied. Here 1–23 denote the combinations of factors.

of tablets[24–26] and powders.[27] Khoptyar et al.[26] have recently shown feasibility of spectroscopic evaluation of tablet concentration on the basis of their PTOFS absorption spectra. Because of the small number of investigated tablets, it was impossible to consider robustness of the technique and its sensitivity to large scattering variation due in part to varying scatterer size and different tablet compaction force. So far, little has been done to systemically study the potential and limitations of the new generation of broadband PTOFS system for tablet spectroscopic analysis.

In this paper, we demonstrate that PTOFS provides a valuable addition to spectroscopic analysis of pharmaceuticals in the wavelength range 1050–1350 nm. Broadband PTOFS was applied in a comprehensive study of 75 tablets in which the drug concentration, filler, and API particle size and compression force were varied. The ability of PTOFS to measure drug concentration was investigated in terms of the prediction ability. The results obtained were compared to those obtained with continuous-wave, transmission NIRS. The robustness of PTOFS toward particle size variation is investigated and compared to transmission NIRS. Finally, it is shown that PTOFS reduced scattering spectra can be used to determine particle form, size, and compression force, without a chemometric calibration model.

MATERIALS AND METHODS

Materials. The 75 tablets used in this study were composed from three components: mannitol, ibuprofen, and magnesium stearate. The active pharmaceutical ingredient (API) in the tablets was ibuprofen, and mannitol was used as the filler. Magnesium stearate is a lubricant added to facilitate tablet compression. The tablets were made by mixing the ingredients according to the experimental design shown in Fig. 1. The experiment was designed to investigate individual and interdependent variation by varying the following factors: filler particle size (FPS), API particle size, API concentration, and filler particle manufacturing method. The complete set of combinations consists of 23 unique

samples, denoted 1 to 23, spanning a wide range of material compositions. The FPSs (mass median diameter) used in the design were 91, 211, and 450 μm, respectively.[28] The average particle diameters of ibuprofen used in the design were 71, 95, and 154 μm, respectively, and the average concentration was varied at five levels; 16, 18, 20, 22, and 24 (%w/w), respectively. Properties for different filler sizes and the manufacturing methods are presented in Table I.

All the tablets were pressed with a single punch press (Korsch EK 0, Korsch AG, Berlin, Germany) equipped with flat, round 10 mm punches. The compression force (CF) was set manually to 8, 12, and 16 kN denoted CF1, CF2, and CF3, respectively, for all powder blends resulting in 3×23 different tablet types (batches). Single-component tablets were compressed in a manual tablet press (Specac, Oprington, UK) using a CF of approximately 20 kN. All tablets had a uniform diameter of 10 mm, with a thickness of ~3 mm and weight of ~300 mg. The tablets were manufactured at AstraZeneca R&D Mölndal, Sweden, for another study.[29]

Transmission Near-Infrared Spectroscopy. Transmission NIRS spectra were recorded for all the tablets using a Fourier transform NIR spectrometer (MB160, ABB-Bomem Inc., Canada), in transmission mode.[29] The spectra were recorded as the average of 32 scans for each tablet, and the resolution was set to 16 cm^{-1} corresponding to ~2 nm at 1200 nm. For a more direct comparison between transmission NIRS and PTOFS the wavelength region from 1050 to 1350 nm was used. For comparative study, the API concentrations in the samples were determined using Raman spectroscopy.[29]

TABLE I. Properties of the different filler particle sizes (FPSs).[28]

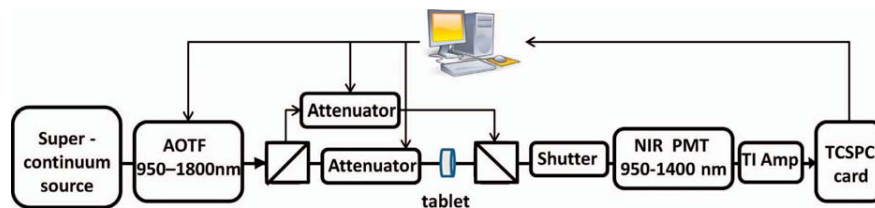| Particle size (μm)	Method	BD (g/ml)	Comp. (%)
FPS1 (91)	Spray dried	0.57	6.9
FPS2 (450)	Granular	0.71	4.5
FPS3 (211)	Spray dried	0.50	9.9

BD = bulk density; Comp. = compressibility.

Fɪɢ. 2.   Schematic showing the set up used for PTOFS. AOTF: acousto-optical tunable filter; PMT: photomultiplier tube; TI Amp: transimpedance amplifier; TCSPC card: time-correlated single-photon counting card.

Photon Time-of-Flight Near-Infrared Spectroscopy. In PTOFS, the time-distribution of photons transmitted through a sample is evaluated with picosecond time resolution. A schematic of the PTOFS system is shown in Fig. 2. A photonic crystal fiber supercontinuum source (SuperK Extreme EXW 12, NKT Photonics A/S, Birkerød, Denmark) was used in combination with an AOTF (SuperK Select, NKT 384 Photonics A/S, Birkerød, Denmark) to generate tunable probe pulses with which to irradiate the tablet. A small fraction of the pulse power is split off prior to the sample and routed directly to the detector for timing reference to increase measurement accuracy.[26] A photomultiplier tube (Hamamatsu, model R3809U-68) is used for detection. The signal is fed to a time-correlated single-photon counting (TCSPC) electronics (Becker&Hickl, model SPC-130) for high-precision measurements of the PTOF distribution.[26] Data acquisition is carried out using an automated measurement sequence implemented in C#. The measurement routine involves setting up the TCSPC module and setting the wavelength and amplitude of the light source. The attenuation of the light intensity through samples was adjusted to obtain a count rate up to 50 kHz during data acquisition. A total photon count of more than 50 000 was considered sufficient for each data point, yielding a recording time of ~30 s per measurement. Tablet spectra were scanned in the spectral range 950–1400 nm with 4 nm resolution. The sequence in which tablets were investigated was also randomized in order to avoid any bias.

The shape of the PTOF distribution is affected by the absorption and scattering of light, which are directly influenced by the chemical and structural composition of the medium. The optical properties, i.e., absorption and reduced scattering, were evaluated from the PTOF distribution at each wavelength with Matlab, using a Levenberg–Marquardt-based fitting algorithm with the diffusion approximation model developed by Contini and Martelli et al.[30] Black-printed office paper is used as a sample to get instrument response function.[21] The instrument response function was in all subsequent evaluations convolved with the fitted diffusion model to take into account the light dispersion in the optical fibers and finite detector response time. The estimated absorption coefficient, μ_a, is normally used for the analysis of the chemical constituents and the composition of the tablet. The reduced scattering coefficient, $\mu_s' = \mu_s(1-g)$, is generally correlated to the structural properties, where

μ_s is scattering and g is called the anisotropy of the medium.

The signal-to-noise ratio (SNR) for both transmission NIRS and PTOFS was calculated by fitting a polynomial to a section of each spectrum, using the expression:

$$\text{SNR} = \text{mean}\left[\frac{\text{spectra}}{|\text{Polynomial fit} - \text{spectra}|}\right] \quad (1)$$

DATA ANALYSIS

Multivariate regression analysis[31] was performed using partial least squares regression[32] to predict the API concentrations from transmission NIRS and PTOF spectra, respectively. Calibration models for the API content were constructed by dividing the data into calibration and validation sets. Group-fold cross-validation[32] and manual selection were used to determine the number of latent variables in the calibrations models. The calibrations were then applied to the validation set to predict the API concentration. In the first case, 70% of the samples were randomly chosen as the calibration set, and the remaining 30% served as the validation set. In the second case, the data were divided based on the average particle size of the tablets.

Analysis of Transmission Near-Infrared Spectra. Near-infrared spectra often require pretreatment for underlying scattering signal.[19] The effect of difference in particle sizes on TNIRS spectra is quantitatively the most important. It can partly be corrected using mean centered data,[31] derivatives,[33] multiplicative scatter correction (MSC),[34] or standard normal variate.[35] We used MSC for the preprocessing of the transmission NIRS spectra.

Analysis of Photon Time-of-Flight Data. The PTOFS technique provided spectra of absorption and reduced scattering as described above. Principal component analysis (PCA) was used in evaluating the absorption spectra, as this provides the most compact orthogonal description of the data.[31] Reduced scattering spectra were modeled with an approximation from Lorentz–Mie theory as explained later.

RESULTS AND DISCUSSION

Measurement Stability and Noise. Bias-variance tests were carried out to determine the stability of the PTOFS system. Figure 3a shows the absorption coefficients of a tablet estimated at three wavelengths close to
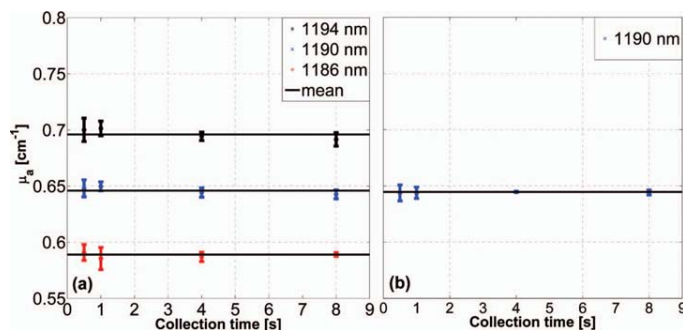
FIG. 3. Estimated absorption coefficient, μ_a, as a function of the data acquisition time of the PTOFS distribution. (**a**) Bias-variance test and (**b**) test for uniform ingredient distribution by measuring on both sides of a tablet. The error bars indicate the SD from three measurements. Mean values for each wavelength are also plotted.

the absorption peak, as a function of data acquisition time. Error bars are the result of repetitive measurements. The acquisition time for the PTOF distribution was varied in these measurements between 0.5 and 8 s at each wavelength. The evaluated absorption for each measurement is within the standard deviation (SD) from the mean of all measurements at that wavelength. The absorption coefficients obtained are constant within 1%, showing that no bias was introduced by altering the acquisition time. Similar tests were performed to check the variation in the distribution of ingredients inside the tablets. A tablet was measured twice from both sides, and the system showed reliable and reproducible results, as can be seen in Fig. 3b.

Evaluated Absorption and Active Pharmaceutical Ingredient Concentrations. Absorbance and absorption spectra from both the transmission NIRS and PTOFS technique are presented in Fig. 4a and 4b, respectively. The transmission NIRS attenuation spectra are plotted in the same wavelength range as the PTOFS spectra, and it can be seen that there is, in general, good agreement between the two methods. The influence of the scattering

properties of the samples can be visualized by a prominent offset shift in the transmission NIRS spectra. The SNR, calculated from Eq. 1, was more than 10 times higher in the transmission NIRS spectra than in the PTOFS spectra. Spectra of pure ingredients are also shown in Fig. 4b, which indicates an overlap of mannitol and ibuprofen spectra at 1200 nm.

Figure 5 shows the scatter plot resulting from the PCA applied to PTOFS absorption spectra for the first two principal components. Ideally separated absorption spectra from reduced scattering spectra will not show any influence from the particle size. If labeled for an uncompressed FPS, no data grouping will be observed. However, the scatter plot shows that tablets with larger filler particles cluster separately from the others, indicating that absorption is not completely separated from reduced scattering. This correlation can be explained by the crosstalk between the optical properties[36] and requires further investigation. For the PTOFS data the first two principal components explain more than 80% of the variance. The results of PCA also suggested that the wavelength region between 1050 and 1350 nm
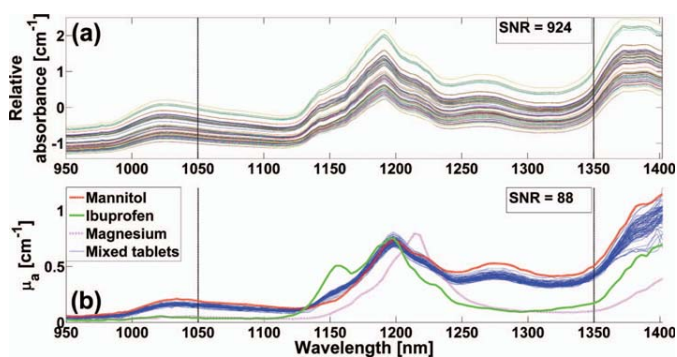

FIG. 4. (**a**) Transmission NIRS absorbance spectra for all 75 mixed tablets and (**b**) PTOFS absorption spectra for all pure and mixed tablets. The dashed vertical lines indicate 1050–1350 nm used for analysis. The signal-to-noise ratio (SNR) is given in each case.
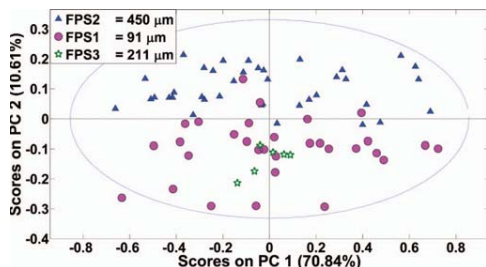
Fig. 5. PCA scatter plot for tablets with different FPSs (before compression) on the first two principal components (PC) for PTOFS absorption spectra. The dashed ellipse indicates 95% confidence interval.

was suitable for prediction of API content since the variation in concentration could be clearly seen in the first principal component.

To predict the API concentrations from both transmission NIRS and PTOFS spectra, partial least squares regression was used, relating the variance to the desired output. The prediction is achieved by extracting a set of orthogonal factors called latent variables from the predictors (wavelengths) that have the best predictive power. The contribution toward variance by predictors for each latent variable is called loading, which can explain how variance may relate to the predictions. Loadings of the first six latent variables of partial least squares for transmission NIRS and PTOFS spectra are shown in Fig. 6a and 6b, respectively. Out of those six, physically meaningful information is contained in only two for transmission NIRS and four for PTOFS. In the case of transmission NIRS, two latent variables are necessary to describe ibuprofen concentrations. For PTOFS, not only ibuprofen concentration and mannitol amplitude is explained, but the crosstalk by scattering as well is captured, requiring comparatively complex models (four variables). Therefore, two and four latent variables are used for transmission NIRS and PTOFS predictions, respectively.

Predictive models are built on tablets in a calibration set and then validated on tablets in a validation set.
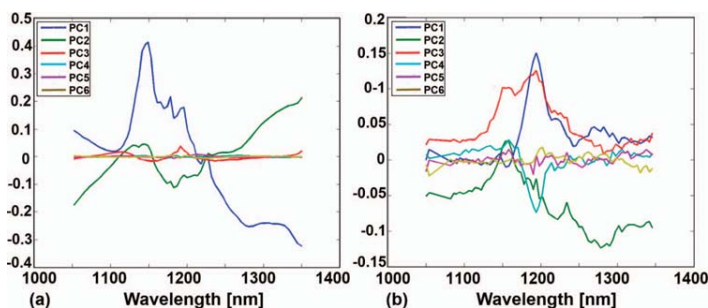
Tablet data are first split into 70–30% sets for calibration and validation, respectively. The prediction performance was then compared to well-structured classification of data. Table II presents the average results of a 100 random set of calibration and validation samples. Ratio of performance to deviation (RPD) is a measure of the usefulness of models, and a value more than three is considered useful for screening.[37] Four latent variables for the PTOFS data produced RPD = 3 and root mean square error of prediction,[38] RMSEP = 0.92. These should be compared with RPD = 2.77 and RMSEP = 1.03 when using two latent variables for the transmission NIRS data. Variance explained by latent variables (R^2) in both cases is comparable. The reasons for PTOFS higher model complexity are the inherent sparseness of the experimental design of the tablet data set and the crosstalk between optical properties.

To compare the robustness of the two techniques the models are challenged by selecting a validation set based on different FPSs than those of the calibration set. The purpose of challenging the models in this way is to see if PTOFS is less sensitive toward variations in raw material than transmission NIRS. Table III presents the prediction results. The models were calibrated using data sets with large FPS, and the predictions were validated on data sets with a small FPS. Model complexities are kept similar to the previous case. Compared to results in Table II, models based on PTOFS spectra improved the RPD value to 3.42 and reduced the RMSEP to 0.84. Models on transmission NIRS data, however, showed higher sensitivity to variations in particle sizes, thus making predictions more difficult. The difference in RMSEP values for transmission NIRS (1.12) and PTOFS (0.84) is statistically significant.

The prediction accuracy of both techniques is comparable when the models are based on uniformly distributed particle sizes. However, when the models are based on the data set using one particle size and the predictions are made for different particle sizes, the prediction error for PTOFS is smaller than that with transmission NIRS. PTOFS thus showed less sensitivity to the variations in raw filler material than transmission NIRS. It can therefore be concluded that the analysis using PTOFS is more robust toward changes in particle sizes.

Fig. 6. Loadings of the first six latent variables of partial least squares for (**a**) transmission NIRS data and (**b**) PTOFS data.

TABLE II. Results of partial least squares regression using group-fold cross-validation for API concentration prediction from transmission NIRS and PTOFS data. The average values over 100 runs are given for the random 70–30% split of the data. The same spectral region, 1050–1350 nm, was considered for both techniques.[a]

Method	Cal. set (%)	Val. set (%)	Pretreat.	LVs	R^2 cal.	R^2 pred.	RMSEC	RMSEP	SD	RPD
Transmission NIRS	70	30	MSC+mean centered	2	0.92	0.81	0.83	1.03	0.34	2.77
PTOFS	70	30	Mean centered	4	0.92	0.88	0.81	0.92	0.12	3.00

[a] Cal. = calibration; Val. = validation; Pretreat. = pretreatment; LVs = latent variables; R2 = Variance explained; RMSEC = root mean square error of calibration; RMSEP = root mean square error of prediction; SD = standard deviation; RPD = ratio of performance to deviation.

TABLE III. Results of partial least squares regression using group-fold cross-validation for API concentration prediction from transmission NIRS and PTOFS data. Model generalization tested on structured selection of calibration and validation sets based on average particle sizes.

Method	Cal. set	Val. set	Pretreat.	LVs	R^2 cal.	R^2 pred.	RMSEC	RMSEP	SD	RPD
Transmission NIRS	Large particles	Small particles	MSC+mean centered	2	0.92	0.86	0.85	1.12	–	2.57
PTOFS	Large particles	Small particles	Mean centered	4	0.93	0.90	0.77	0.84	–	3.42

Photon Time-of-Flight Spectroscopy Reduced Scattering. Figure 7 presents PTOFS reduced scattering spectra for pure ingredients and mixed tablets, respectively. Although the absorption and reduced scattering have different origins, they are often correlated[36] due to crosstalk as a result of finite bandwidth, modeling inaccuracies, or data-gathering procedures. The reduced scattering spectra from mixed tablets indicate a correlation with absorption peaks around 1200 nm and after 1350 nm (see Fig. 4). All the mixed tablets exhibit higher wavelength dependence of the scattering slope and scattering amplitudes than ibuprofen and magnesium stearate. This indicates that mannitol is mainly responsible for scattering inside the mixed tablets. The reduced scattering coefficient is defined as[39]

$$\mu'_s = \rho Q_s \frac{\pi d^2}{4}(1-g) \tag{2}$$

where ρ is the average particle number density, Q_s is size-dependent scattering efficiency of the particle, d is diameter of the scatterer, and g is the anisotropy of the medium. The scattering efficiency Q_s tends to approach a value of 2 for large pure scatterers, for $\pi d/\lambda \gg 1$, where λ is the wavelength of the light. The empirically observed

scattering behavior for small and intermediate sized particles is relatively well modeled using Rayleigh and Mie theories:[40]

$$\mu'_s = A(\lambda/\lambda_0)^{-\beta} \tag{3}$$

Equation 3 is a relatively good approximation for scattering behavior of pharmaceuticals in the NIR spectral regime. A is the reduced scattering coefficient at the reference wavelength λ_0, and β is the slope of the fit versus wavelength. For Rayleigh scattering, the size parameter, $\pi d/\lambda$, is much less than 1, and the scattering is dependent on λ^{-4}. For larger particles than the Rayleigh limit, β varies from 4 to 0 depending on the size parameter. The large particle limit is $\beta = 0$, where $Q_s = 2$. At such size parameters μ'_s will be independent of wavelength. According to Lorentz–Mie scattering calculations, the filler particles would approach this limit for all three FPSs. However, the reduced scattering of mannitol is highly dependent on wavelength, indicating an effective size parameter being much smaller than for the original mannitol particles used for the production of the tablets. Figure 8 shows scanning electron microscopy images of original filler particles with three different FPS used in the tablets, where it can be seen that they
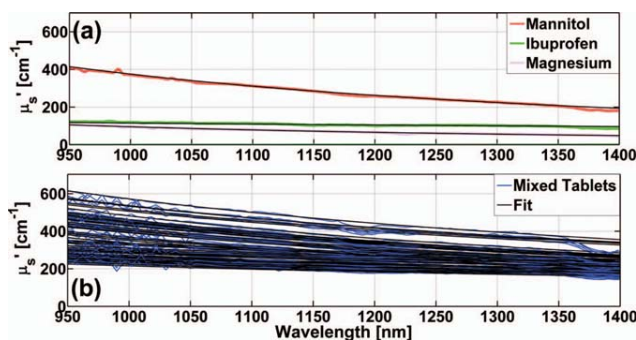

Fig. 7. (**a**) Reduced scattering spectra (μ'_s) for pure ingredients and (**b**) mixed tablets. The black curves are the predictions based on Eq. 3.
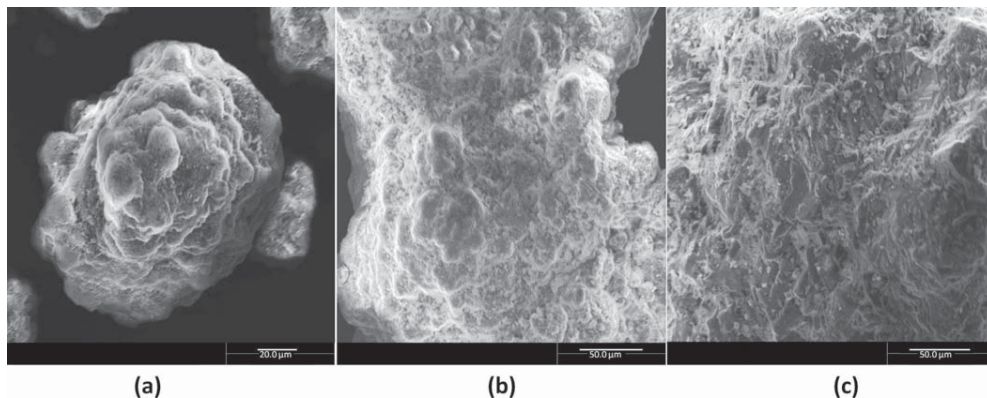
Fɪɢ. 8.   Scanning electron microscopy images of filler particles (mannitol) with sizes of (**a**) 91 µm, (**b**) 211 µm, and (**c**) 450 µm.

are irregularly shaped and exhibit surface roughness. When compression is applied to form a tablet, these irregularities can lead to voids between surfaces that act as scatterers.[41,42] Compared to the original particles, these voids are small enough to create wavelength-dependent scattering of the light.

Effects of Filler Particle Size and Compression Force. The scattering amplitude is plotted against the scattering slope in Fig. 9 for three different compression forces. The cluster of data for lower β values presents tablets with FPS2 = 450 µm, clearly distinguishable from FPS1 and FPS3, clustered at higher β values. This illustrates the ability of PTOFS to directly differentiate between FPS and CF.

To have a better visualization of different groups of data, a relative scale image is presented in Fig. 10a. Subtracting the fitted equation for CF1 from all fitted equations gives a clear separation of groups on the y-axis. Tablets with FPS2 = 450 µm are indicated by filled

symbols and FPS1 = 91 µm by open symbols; the green stars show FPS3 = 211 µm. Using PCA provides a similar way to explore these effects in transmission NIRS data. Figure 10b shows the PCA scatter plot for transmission NIRS data for first two principal components, explaining more than 98% variance (compared to 80% in the PTOFS data; see Fig. 5). It is interesting that the tablets made with FPS3 = 211 µm and FPS1 = 91 µm are located together in both figures. The reason is believed to be the smaller final size of the filler particles after tableting. The compression force affects the internal structure of the tablet depending on the properties of the particles. Thus, particle size is not the only relevant factor; particle density also affects scattering. Harder particles may not collapse as easily as softer particles under an external force. Larger particles, 450 µm, were made by granulation while the smaller particles were spray dried. This may explain why the tablets made with FPS3 = 211 µm
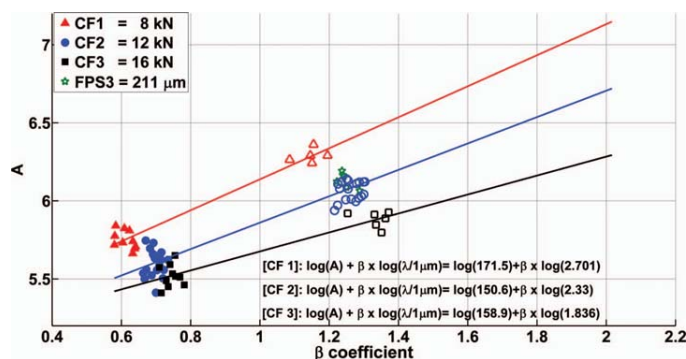

Fɪɢ. 9.   Plot of A vs. β from Eq. 3. The solid lines are the linear fits to data from tablets made with the same compression force (CF). Filled markers represent FPS2 = 450 µm, and hollow markers represent FPS = 91 µm, except green stars, presenting FPS3 = 211 µm. Inset: Equations for solid lines through each CF.
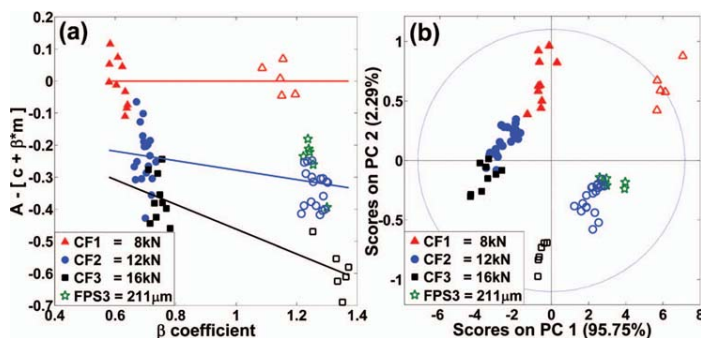
FIG. 10. (**a**) Rescaled plot of "A" vs. "β" from Eq. 3 with the CF1 fit subtracted. "c" is the offset and "m" is the slope of the fit. (**b**) PCA scatter plot of transmission NIRS data on first two principal components.

particles coincide with the particle cluster representing FPS1 = 91 μm.

Principal component analysis as applied to the transmission NIRS data also shows a clear dependence on FPS and compression force. However, to be able to use this information in a productive manner, multivariate data analysis techniques are required for interpretation and predictions. The same information can easily be obtained from the reduced scattering coefficient of PTOFS. The effects of the production method of filler particle, particle size after compression, and compression force used during tablet production are evident in the wavelength dependence and amplitude of the PTOFS scattering spectra. Measuring the reduced scattering with PTOFS enables a direct relation to be established between particle size and the coefficient β. In this study, we observed that as the FPS increases, the effects of the compression force become less distinguishable. However, compression effects are well distinguished for tablets with lower FPSs. PTOFS can directly differentiate between filler particles made with different manufacturing processes.

CONCLUSIONS

A comprehensive study of pharmaceutical tablets has been carried out in the close NIR spectral regime 1050–1350 nm using PTOFS and the results compared to those obtained with traditional transmission NIR spectroscopy. Chemometric models were built to predict the ibuprofen concentration from the PTOFS absorption spectra and transmission NIRS spectra. Transmission NIRS and PTOFS were found to have comparable prediction ability when the models were based on uniformly distributed data sets. When the models were trained on tablets with larger filler particle size and challenged with test sets consisting of tablets with a smaller filler particle size, the prediction ability of transmission NIRS was significantly reduced. However, corresponding models based on PTOFS data showed better prediction ability. Models based on PTOFS absorption spectra for the prediction of drug concentrations are less sensitive to variations in

filler particle size, making PTOFS a comparatively robust technique.

We showed that the amplitude and slope of reduced scattering spectra not only distinguish between manufacturing processes of filler material, but also characterize the process parameters, like compression force. PTOFS thus provides physically meaningful parameters without chemometric models. Transmission NIRS, on the other hand, provides chemometric pseudo-variables that can be difficult to interpret. The steep scattering slopes observed suggest that scattering occurs from much smaller scatterers than the original filler particles and that the observed tablet scattering spectra cannot be directly explained by the original particle size of the ingredients.

1. J. Munson, C.F. Stanfield, B. Gujral. "A Review of Process Analytical Technology (PAT) in the U.S. Pharmaceutical Industry". Curr. Pharm. Anal. 2006. 2(4): 405-414.
2. M. Blanco, J. Coello, H. Iturriaga, S. Maspoch, C. de la Pezuela. "Near-Infrared Spectroscopy in the Pharmaceutical Industry". Analyst (Cambridge, UK). 1998. 123: 135R-150R.
3. B.F. MacDonald, K.A. Prebble. "Some Applications of Near-Infrared Reflectance Analysis in the Pharmaceutical Industry". J. Pharm. Biomed. Anal. 1993. 11(11-12): 1077-1085.
4. M. Blanco, M. Alcala. "Use of Near-Infrared Spectroscopy for Off-Line Measurements in the Pharmaceutical Industry". In: K. Bakeev, editor. Process Analytical Technology. Oxford: Blackwell, 2005. Pp. 362-391.
5. Y. Roggo, P. Chalus, L. Maurer, C. Lema-Martinez, A. Edmond, N. Jent. "A Review of Near Infrared Spectroscopy and Chemometrics in Pharmaceutical Technologies". J. Pharm. Biomed. Anal. 2007. 44(3): 683-700.
6. R.C. Lyon, D.S. Lester, E.N. Lewis, E. Lee, X.Y. Lawrence, E.H. Jefferson, A.S. Hussain. "Near-Infrared Spectral Imaging for Quality Assurance of Pharmaceutical Products: Analysis of Tablets to Assess Powder Blend Homogeneity". AAPS PharmSciTech. 2002. 3(3): 1-15.

7. T. De Beer, A. Burggraeve, M. Fonteyne, L. Saerens, J.P. Remon, C. Vervaet. "Near Infrared and Raman Spectroscopy for the In-Process Monitoring of Pharmaceutical Production Processes". Int. J. Pharm. 2011. 417(1-2): 32-47.

8. A. Bogomolov. "Multivariate Process Trajectories: Capture, Resolution and Analysis". Chemom. Intell. Lab. Syst. 2011. 108(1): 49-63.

9. E. Otsuka, H. Abe, M. Aburada, M. Otsuka. "Nondestructive Prediction of the Drug Content of an Aspirin Suppository by Near-Infrared Spectroscopy". Drug Dev. Ind. Pharm. 2010. 36(7): 839-844.

10. M. Otsuka, F. Kato, Y. Matsuda. "Determination of Indomethacin Polymorphic Contents by Chemometric Near-Infrared Spectroscopy and Conventional Powder X-Ray Diffractometry". Analyst. 2001. 126(9): 1578-1582.

11. J.P. Higgins, S.M. Arrivo, G. Thurau, R.L. Green, W. Bowen, A. Lange, A.C. Templeton, D.L. Thomas, R.A. Reed. "Spectroscopic Approach for On-Line Monitoring of Particle Size During the Processing of Pharmaceutical Nanoparticles". Anal. Chem. 2003. 75(8): 1777-1785.

12. M. Otsuka. "Comparative Particle Size Determination of Phenacetin Bulk Powder by Using Kubelka–Munk Theory and Principal Component Regression Analysis Based on Near-Infrared Spectroscopy". Powder Technol. 2004. 141(3): 244-250.

13. R.R. Shinde, G.V. Balgi, S.L. Nail, E.M. Sevick-Muraca. "Frequency-Domain Photon Migration Measurements for Quantitative Assessment of Powder Absorbance: A Novel Sensor of Blend Homogeneity". J. Pharm. Sci. 1999. 88(10): 959-966.

14. B.G. Osborne. "Near-Infrared Spectroscopy in Food Analysis". In: R.A. Meyers, editor. Encyclopedia of Analytical Chemistry. Hoboken, NJ: John Wiley & Sons, 2006. Online ed. doi: 10.1002/9780470027318.a1018.

15. E. Wolfrum, C. Payne, T. Stefaniak, W. Rooney, N. Dighe, B. Bean, J. Dahlberg. Multivariate Calibration Models for Sorghum Composition Using Near-Infrared Spectroscopy. Golden, CO: National Renewable Energy Laboratory, 2013.

16. Z. Sun, S. Torrance, F.K. McNeil-Watson, E.M. Sevick-Muraca. "Application of Frequency Domain Photon Migration to Particle Size Analysis and Monitoring of Pharmaceutical Powders". Anal. Chem. 2003. 75(7): 1720-1725.

17. C. Abrahamsson, A. Löwgren, B. Strömdahl, T. Svensson, S. Andersson-Engels, J. Johansson, S. Folestad. "Scatter Correction of Transmission Near-Infrared Spectra by Photon Migration Data: Quantitative Analysis of Solids". Appl. Spectrosc. 2005. 59(11): 1381-1387.

18. O.H.A. Nielsen, A.A. Subash, F.D. Nielsen, A.B. Dahl, J.L. Skytte, S. Andersson-Engels, D. Khoptyar. "Spectral Characterization of Dairy Products Using Photon Time-of-Flight Spectroscopy". J. Near Infrared Spectrosc. 2013. 21(5): 375-383.

19. Å. Rinnan, F. van den Berg, S.B. Engelsen. "Review of the Most Common Pre-Processing Techniques for Near-Infrared Spectra". Trends Anal. Chem. 2009. 28(10): 1201-1222.

20. J. Mi, L. Zhang, L. Zhao, J. Li. "Particle Size Regression Correction for NIR Spectrum Based on the Relationship Between Absorbance and Particle Size". Front. Optoelectron. 2013. 6(2): 216-223.

21. T. Svensson, E. Alerstam, D. Khoptyar, J. Johansson, S. Folestad, S. Andersson-Engels. "Near-Infrared Photon Time-of-Flight Spectroscopy of Turbid Materials Up to 1400 nm". Rev. Sci. Instrum. 2009. 80(6): 063105-063105.

22. C. Abrahamsson, T. Svensson, S. Svanberg, S. Andersson-Engels, J. Johansson, S. Folestad. "Time and Wavelength Resolved Spectroscopy of Turbid Media Using Light Continuum Generated in a Crystal Fiber". Opt. Express. 2004. 12(17): 4103-4112.

23. I. Bargigia, A. Tosi, A.B. Shehata, A.D. Frera, A. Farina, A. Bassi, P. Taroni, A. Dalla Mora, F. Zappa, R. Cubeddu, A. Pifferi. "Time-Resolved Diffuse Optical Spectroscopy Up to 1700 nm by Means of a Time-Gated IngaAs/InP Single-Photon Avalanche Diode". Appl. Spectrosc. 2012. 66(8): 944-950.

24. J. Johansson, S. Folestad, M. Josefson, A. Sparén, C. Abrahamsson, S. Andersson-Engels, S. Svanberg. "Time-Resolved NIR/VIis Spectroscopy for Analysis of Solids: Pharmaceutical Tablets". Appl. Spectrosc. 2002. 56(6): 725-731.

25. C. Abrahamsson, J. Johansson, S. Andersson-Engels, S. Svanberg, S. Folestad. "Time-Resolved NIR Spectroscopy for Quantitative Analysis of Intact Pharmaceutical Tablets". Anal. Chem. 2005. 77(4): 1055-1059.

26. D. Khoptyar, A.A. Subash, S. Johansson, M. Saleem, A. Sparén, J. Johansson, S. Andersson-Engels. "Broadband Photon Time-of-Flight Spectroscopy of Pharmaceuticals and Highly Scattering Plastics in the VIS and Close NIR Spectral Ranges". Opt. Express. 2013. 21(18): 20941-20953.

27. C. D'Andrea, E.A. Obraztsova, A. Farina, P. Taroni, G. Lanzani, A. Pifferi. "Absorption Spectroscopy of Powdered Materials Using Time-Resolved Diffuse Optical Methods". Appl. Opt. 2012. 51(32): 7858-7863.

28. N. Souihi, M. Dumarey, H. Wikström, P. Tajarobi, M. Fransson, O. Svensson, M. Josefson, J. Trygg. "A Quality by Design Approach to Investigate the Effect of Mannitol and Dicalcium Phosphate Qualities on Roll Compaction". Int. J. Pharm. 2013. 447(1-2): 47-61.

29. A. Spare'n, O. Svensson, M. Hartman, M. Fransson, J. Johansson. "Matrix Effects in Quantitative Assessment of Pharmaceutical Tablets, Using Transmission Raman and NIR Spectroscopy". Appl. Spectrosc. Paper submitted. 2014.

30. D. Contini, F. Martelli, G. Zaccanti. "Photon Migration Through a Turbid Slab Described by a Model Based on Diffusion Approximation. I. Theory". Appl. Opt. 1997. 36(19): 4587-4599.

31. L. Eriksson, E. Johansson, N. Kettaneh-Wold, S. Wold. Introduction to Multi and Megavariate Data Analysis Using Projection Methods (PCA and PLS). Umea, Sweden: Umetrics AB, 1999.

32. T. Hastie, R. Tibshirani, J. Friedman, J. Franklin. "The Elements of Statistical Learning: Data Mining, Inference and Prediction". Math. Intell. 2005. 27(2): 83-85.

33. A. Savitzky, M.J.E. Golay. "Smoothing and Differentiation of Data by Simplified Least Squares Procedures". Anal. Chem. 1964. 36(8): 1627-1639.

34. P. Geladi, D. MacDougall, H. Martens. "Linearization and Scatter-Correction for Near-Infrared Reflectance Spectra of Meat". Appl. Spectrosc. 1985. 39(3): 491-500.

35. R.J. Barnes, M.S. Dhanoa, S.J. Lister. "Standard Normal Variate Transformation and De-Trending of Near Infrared Diffuse Reflectance Spectra". Appl. Spectrosc. 1989. 43(5): 772-777.

36. E. Alerstam, S. Andersson-Engels, T. Svensson. "Improved Accuracy in Time-Resolved Diffuse Reflectance Spectroscopy". Opt. Express. 2008. 16(14): 10440-10454.

37. G.D. Batten. "Plant Analysis Using Near Infrared Reflectance Spectroscopy: The Potential and the Limitations". Aust. J. Exp. Agric. 1998. 38(7): 697-706.

38. T. Næs, T. Isaksson. "SEP or RMSEP, Which Is Best?" NIR News. 1991. 2(4): 16-0.

39. S.L. Jacques. "Fractal Nature of Light Scattering in Tissues". J. Innov. Opt. Health Sci. 2011. 4(1): 1-7.

40. R. Graaff, J.G. Aarnoudse, J.R. Zijp, P.M.A. Sloot, F.F.M. de Mul, J. Greve, M.H. Koelink. "Reduced Light Scattering Properties for Mixtures of Spherical Particles: A Simple Approximation Derived from Mie Calculations". Appl. Opt. 1992. 31(10): 1370-1376.

41. W.C. Mundy, J.A. Roux, A.M. Smith. "Mie Scattering by Spheres in an Absorbing Medium". JOSA. 1974. 64(12): 1593-1597.

42. A.H. Hielscher, R.E. Alcouffe, R.L. Barbour. "Comparison of Finite-Difference Transport and Diffusion Calculations for Photon Migration in Homogeneous and Heterogeneous Tissues". Phys. Med. Biol. 1998. 43(5): 1285-1302.

Computational effective solution of the inverse problem in time-of-flight spectroscopy

Faisal Kamran, Otto H. A. Abildgaard, Arman A. Subash, Peter E. Andersen, Stefan Andersson-Engels, Dmitry Khoptyar.

Computationally effective solution of the inverse problem in time-of-flight spectroscopy

Faisal Kamran,[1,*] Otto H. A. Abildgaard,[2] Arman A. Subash,[3] Peter E. Andersen,[1] Stefan Andersson-Engels,[2] and Dmitry Khoptyar[2]

[1]*Department of Photonics Engineering, Technical University of Denmark, Denmark*
[2]*Department of Applied Mathematics and Computer Science, Technical University of Denmark, Denmark*
[3]*Department of Physics, Lund University, Sweden*
*faisal309@gmail.com

Abstract: Photon time-of-flight (PTOF) spectroscopy enables the estimation of absorption and reduced scattering coefficients of turbid media by measuring the propagation time of short light pulses through turbid medium. The present investigation provides a comparison of the assessed absorption and reduced scattering coefficients from PTOF measurements of intralipid 20% and India ink-based optical phantoms covering a wide range of optical properties relevant for biological tissues and dairy products. Three different models are used to obtain the optical properties by fitting to measured temporal profiles: the Liemert-Kienle model (LKM), the diffusion model (DM) and a white Monte-Carlo (WMC) simulation-based algorithm. For the infinite space geometry, a very good agreement is found between the LKM and WMC, while the results obtained by the DM differ, indicating that the LKM can provide accurate estimation of the optical parameters beyond the limits of the diffusion approximation in a computational effective and accurate manner. This result increases the potential range of applications for PTOF spectroscopy within industrial and biomedical applications.

References and links

1. L. X. Yu, "Pharmaceutical quality by design: product and process development, understanding, and control," Pharm. Res. **25**(4), 781–791 (2008).
2. H. Huang, H. Yu, H. Xu, and Y. Ying, "Near infrared spectroscopy for on/in-line monitoring of quality in foods and beverages: A review," J. Food Eng. **87**(3), 303–313 (2008).
3. B. M. Nicolaï, K. Beullens, E. Bobelyn, A. Peirs, W. Saeys, K. I. Theron, and J. Lammertyn, "Nondestructive measurement of fruit and vegetable quality by means of NIR spectroscopy: A review," Postharvest Biol. Technol. **46**(2), 99–118 (2007).
4. M. Jamrógiewicz, "Application of the near-infrared spectroscopy in the pharmaceutical technology," J. Pharm. Biomed. Anal. **66**, 1–10 (2012).
5. Y. Roggo, P. Chalus, L. Maurer, C. Lema-Martinez, A. Edmond, and N. Jent, "A review of near infrared spectroscopy and chemometrics in pharmaceutical technologies," J. Pharm. Biomed. Anal. **44**(3), 683–700 (2007).
6. S. Tsuchikawa, "A review of recent near infrared research for wood and paper," Appl. Spectrosc. Rev. **42**(1), 43–71 (2007).
7. S. S. Tsuchikawa and M. Schwanninger, "A review of recent near infrared research for wood and paper (Part 2)," Appl. Spectrosc. Rev. **48**(7), 560–587 (2013).
8. T. Durduran, R. Choe, W. B. Baker, and A. G. Yodh, "Diffuse optics for tissue monitoring and tomography," Rep. Prog. Phys. **73**(7), 076701 (2010).
9. M. Wolf, M. Ferrari, and V. Quaresima, "Progress of near-infrared spectroscopy and topography for brain and muscle clinical applications," J. Biomed. Opt. **12**(6), 062104 (2007).
10. A. Pifferi, A. Farina, A. Torricelli, G. Quarto, R. Cubeddu, and P. Taronia, "Time-domain broadband near infrared spectroscopy of the female breast: a focused review from basic principles to future perspectives," J. Near Infrared Spectrosc. **20**(1), 223–235 (2012).

11. D. Contini, L. Zucchelli, L. Spinelli, M. Caffini, R. Re, A. Pifferi, R. Cubeddu, and A. Torricelli, "Brain and muscle near infrared spectroscopy/imaging techniques," J. Near Infrared Spectrosc. **20**(1), 15–27 (2012).
12. Q. Luo, B. Li, Z. Qiu, Z. Huang, Y. Gu, and X. D. Li, "Advanced optical techniques for monitoring dosimetric parameters in photodynamic therapy," Proc. SPIE **8553**, 85530F (2012).
13. M. S. Patterson, B. Chance, and B. C. Wilson, "Time resolved reflectance and transmittance for the non-invasive measurement of tissue optical properties," Appl. Opt. **28**(12), 2331–2336 (1989).
14. K. Shimizu, A. Ishimaru, L. Reynolds, and A. P. Bruckner, "Backscattering of a picosecond pulse from densely distributed scatterers," Appl. Opt. **18**(20), 3484–3488 (1979).
15. L. V. Wang and H. Wu, *Biomedical Optics:Pprinciples and Imaging* (John Wiley & Sons, 2012).
16. F. Martelli, S. D. Bianco, and A. Ismaelli, *Light Propagation Through Biological Tissue and Other Diffusive Media: Theory, Solution and Software* (SPIE Press, 2009).
17. E. D. Aydin, C. R. E. De-Oliveira, and A. J. H. Goddard, "A finite element-spherical harmonics radiation transport model for photon migration in turbid media," J. Quant. Spectrosc. Radiat. Transf. **84**(3), 247–260 (2004).
18. A. Liemert and A. Kienle, "Analytical solution of the radiative transfer equation for infinite-space fluence," Phys. Rev. A **83**(1), 015804 (2011).
19. A. D. Klose and E. W. Larsen, "Light transport in biological tissue based on the simplified spherical harmonics equations," J. Comput. Phys. **220**(1), 441–470 (2006).
20. M. L. Adams and E. W. Larsen, "Fast iterative methods for discrete-ordinates particle transport calculations," Prog. Nucl. Energy **40**(1), 3–159 (2002).
21. M. S. Patterson, B. Chance, and B. C. Wilson, "Time resolved reflectance and transmittance for the non-invasive measurement of tissue optical properties," Appl. Opt. **28**(12), 2331–2336 (1989).
22. E. Alerstam, W. C. Y. Lo, T. D. Han, J. Rose, S. Andersson-Engels, and L. Lilge, "Next-generation acceleration and code optimization for light transport in turbid media using GPUs," Biomed. Opt. Express **1**(2), 658–675 (2010).
23. E. Alerstam, T. Svensson, and S. Andersson-Engels, "Parallel computing with graphics processing units for high-speed Monte Carlo simulation of photon migration," J. Biomed. Opt. **13**(6), 060504 (2008).
24. A. Liemert and A. Kienle, "Infinite space Green's function of the time-dependent radiative transfer equation," Biomed. Opt. Express **3**(3), 543–551 (2012).
25. J. C. C. Day, R. Bennett, B. Smith, C. Kendall, J. Hutchings, G. M. Meaden, C. Born, S. Yu, and N. Stone, "A miniature confocal Raman probe for endoscopic use," Phys. Med. Biol. **54**(23), 7077–7087 (2009).
26. E. Alerstam, T. Svensson, S. Andersson-Engels, L. Spinelli, D. Contini, A. Dalla Mora, A. Tosi, F. Zappa, and A. Pifferi, "Single-fiber diffuse optical time-of-flight spectroscopy," Opt. Lett. **37**(14), 2877–2879 (2012).
27. A. Puszka, L. Di Sieno, A. D. Mora, A. Pifferi, D. Contini, G. Boso, A. Tosi, L. Hervé, A. Planat-Chrétien, A. Koenig, and J. M. Dinten, "Time-resolved diffuse optical tomography using fast-gated single-photon avalanche diodes," Biomed. Opt. Express **4**(8), 1351–1365 (2013).
28. E. Simon, F. Foschum, and A. Kienle, "Hybrid Green's function of the time-dependent radiative transfer equation for anisotropically scattering semi-infinite media," J. Biomed. Opt. **18**(1), 015001 (2013).
29. E. Simon, F. Foschum, and A. Kienle, "Time-resolved diffuse spectroscopy measurements using a hybrid Green's function for the radiative transfer equation," Proc. SPIE **8799**, 879906 (2013).
30. O. H. A. Nielsen, A. A. Subash, F. D. Nielsen, A. B. Dahl, J. L. Skytte, S. Andersson-Engels, and D. Khoptyar, "Spectral characterizations of dairy products using photon time-of-flight spectroscopy," J. Near Infrared Spectrosc. **21**(5), 375–383 (2013).
31. D. Khoptyar, A. A. Subash, S. Johansson, M. Saleem, A. Sparén, J. Johansson, and S. Andersson-Engels, "Broadband photon time-of-flight spectroscopy of pharmaceuticals and highly scattering plastics in the VIS and close NIR spectral ranges," Opt. Express **21**(18), 20941–20953 (2013).
32. E. Alerstam, S. Andersson-Engels, and T. Svensson, "White Monte Carlo for time-resolved photon migration," J. Biomed. Opt. **13**(4), 041304 (2008).
33. B. W. Pogue and M. S. Patterson, "Review of tissue simulating phantoms for optical spectroscopy, imaging and dosimetry," J. Biomed. Opt. **11**(4), 041102 (2006).
34. T. Svensson, E. Alerstam, D. Khoptyar, J. Johansson, S. Folestad, and S. Andersson-Engels, "Near-infrared photon time-of-flight spectroscopy of turbid materials up to 1400 nm," Rev. Sci. Instrum. **80**(6), 063105 (2009).
35. E. Alerstam, S. Andersson-Engels, and T. Svensson, "Improved accuracy in time-resolved diffuse reflectance spectroscopy," Opt. Express **16**(14), 10440–10454 (2008).
36. S. T. Flock, S. L. Jacques, B. C. Wilson, W. M. Star, and M. J. C. van Gemert, "Optical properties of Intralipid: a phantom medium for light propagation studies," Lasers Surg. Med. **12**(5), 510–519 (1992).
37. H. J. van Staveren, C. J. M. Moes, J. van Marle, S. A. Prahl, and M. J. C. van Gemert, "Light scattering in Intralipid-10% in the wavelength range of 400-1100 nm," Appl. Opt. **30**(31), 4507–4514 (1991).
38. H. Karlsson, I. Fredriksson, M. Larsson, and T. Strömberg, "Inverse Monte Carlo for estimation of scattering and absorption in liquid optical phantoms," Opt. Express **20**(11), 12233–12246 (2012).
39. E. Alerstam, *Enhancing the Performance of Time-Resolved Spectroscopy* (Lund University, 2007).
40. L. V. Wang and S. L. Jacques, "Source of error in calculation of optical diffuse reflectance from turbid media using diffusion theory," Comput. Methods Programs Biomed. **61**(3), 163–170 (2000).
41. T. Svensson, E. Alerstam, M. Einarsdóttír, K. Svanberg, and S. Andersson-Engels, "Towards accurate in vivo spectroscopy of the human prostate," J Biophotonics **1**(3), 200–203 (2008).

42. P. Di Ninni, F. Martelli, and G. Zaccanti, "The use of India ink in tissue-simulating phantoms," Opt. Express **18**(26), 26854–26865 (2010).
43. L. Spinelli, M. Botwicz, N. Zolek, M. Kacprzak, D. Milej, P. Sawosz, A. Liebert, U. Weigel, T. Durduran, F. Foschum, A. Kienle, F. Baribeau, S. Leclair, J. P. Bouchard, I. Noiseux, P. Gallant, O. Mermut, A. Farina, A. Pifferi, A. Torricelli, R. Cubeddu, H. C. Ho, M. Mazurenka, H. Wabnitz, K. Klauenberg, O. Bodnar, C. Elster, M. Bénazech-Lavoué, Y. Bérubé-Lauzière, F. Lesage, D. Khoptyar, A. A. Subash, S. Andersson-Engels, P. Di Ninni, F. Martelli, and G. Zaccanti, "Determination of reference values for optical properties of liquid phantoms based on Intralipid and India ink," Biomed. Opt. Express **5**(7), 2037–2053 (2014).
44. A. Pifferi, R. Berg, P. Taroni, and S. Andersson-Engels, "Fitting of time-resolved reflectance curves with a Monte Carlo model," in OSA Proc. Adv. Opt. Imaging Photon Migr., Proc. Top. Meet. **2**, 311–314 (1996).
45. A. Pifferi, P. Taroni, G. Valentini, and S. Andersson-Engels, "Real-time method for fitting time-resolved reflectance and transmittance measurements with a monte carlo model," Appl. Opt. **37**(13), 2774–2780 (1998).
46. S. L. Jacques, "Optical properties of biological tissues: a review," Phys. Med. Biol. **58**(11), R37–R61 (2013).
47. A. Liemert and A. Kienle, "Explicit solutions of the radiative transport equation in the P3 approximation," Med. Phys. **41**(11), 111916 (2014).

1. Introduction

Diffuse optical spectroscopy (DOS) considerably extends conventional spectroscopic analysis in turbid samples and enables monitoring of not only absorption but also scattering properties. The absorption properties of a sample is characterised by the absorption coefficient (μ_a), whereas the transport-reduced scattering coefficient (μ'_s) quantifies the macroscopic scattering in a sample.

DOS thus enables practical and cost-efficient means to monitor structural properties and chemical composition of diverse samples. It is widely used for quality control [1] and process monitoring in food [2, 3], pharmaceuticals [4, 5] and timber [6, 7] industries. Other important DOS applications are in biomedical diagnostics [8–11] and medical treatment monitoring [12], respectively. For biomedical applications DOS is of particular interest due to its non- or minimally-invasive character, reducing risks for investigation-induced pain or infection.

Photon time-of-flight (PTOF) and frequency-domain techniques extend the capabilities of conventional continuous wave (CW) DOS, by separating absorption and scattering properties in comparison to merely measuring the light attenuation [13, 14]. This enriches the diagnostic potential of the technique, and provides potential for use in wider application areas.

In PTOF spectroscopy absorption and scattering are independently evaluated by monitoring of the propagation of short (picosecond) light pulses through turbid sample [15]. The evaluation generally requires solving an inverse problem where prediction from a light propagation model is fitted to the measured shape of propagated light pulses [15]. The light propagation models used for this purpose are derived from the radiative transport equation [16].

Although some options for modelling light propagation are available [17–20], until recently the practical choice was limited to either the analytical diffusion model (DM) approximation [21] or numerical Monte-Carlo simulations (MCS). Both techniques have drawbacks. The diffusion approximation assumes many scattering events, and thus its applicability range is limited to $\mu'_s \gg \mu_a$ and to large separation between the light source and detection positions in the medium. Although strongly facilitated by recent advances in parallel based GPU-computations [22, 23], MCS are still quite elaborate, time-consuming and a demanding numerical technique for solving inverse problems. In this way, the lack of universal and computationally effective analytical modelling considerably hinders wider application of DOS in many important areas including both biomedical and industrial applications.

Recently a new analytical solution to the radiative transport equation for the fluence in infinite space was presented by Liemert and Kienle [24]. On the basis of comparison to MCS, the authors claimed that their model, in the following referred as the Liemert-Kienle model (LKM), is effectively free from limitations adherent to DM, while being computationally much more efficient than MCS. If the accuracy of the model is verified in independent

studies, this result constitutes a remarkable advance in the field of DOS that strongly facilitates wider application of the technique. Indeed the claimed precision and computational simplicity of the LKM would enable high accuracy of real-time DOS measurements for the range of optical parameters, typical for biological tissue and numerous common food products. Furthermore the LKM claims to facilitate measurements at small source to detector separations, which is highly desirable for the development of miniature probes for medical and cost-efficient industrial applications [25–27].

To date the LKM has been developed and tested by the same group in comparisons to MCS only [18, 24, 28, 29]. To the best of our knowledge, the LKM has neither been evaluated by an independent group nor been used for solving the inverse problem in the infinite geometry for evaluating actual experimental data.

The objective of the present paper is thus to make the first independent evaluation of the performance of the LKM for assessing the absorption and reduced scattering coefficients of a turbid media in the infinite geometry. For this, intralipid/ink-based phantoms, measured using our photon-time-of flight spectrometer, were employed [30, 31]. We compare the LKM evaluated optical properties from such measurements to those obtained by evaluations using previously evaluated white Monte-Carlo (WMC) [32] and diffusion model (DM) [21] algorithms. In this way we also present first ever reported verification of LKM by independent comparison to MCS. The aim is to clarify the accuracy and validation range of this novel model for PTOF data analysis, and also what impact this may have for industrial and biomedical applications, respectively.

2. Materials and methods

The liquid optical phantoms were prepared from intralipid 20% (Fresenius Kabi AB, Uppsala, Sweden) and prediluted India ink (Emergo Europe, The Hague, The Netherlands) added in controlled amounts to 500 ml of tap water in a 1000 ml beaker using an Eppendorf pipette. Although the optical properties of ink and intralipid are not known with a precision better than 85% - 90% and may vary slightly from batch to batch [33], the absorption and scattering of the phantom solution is linearly proportional to the ink and intralipid concentrations, respectively. This relation is customarily used for linearity calibrations in DOS systems.
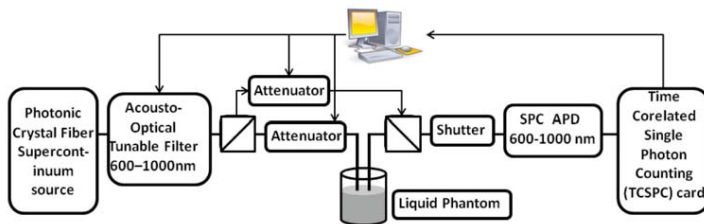
Fig. 1. Schematics of the PTOF spectrometer. SPC - Single photon counting, APD -Avalanche photodiode.

The PTOF spectrometer used for experiments was recently presented [30, 31]. The schematic of the instrument is shown in Fig. 1. To summarise, a super-continuum source (SuperK Extreme EXW 12, NKT Photonics A/S, Birkerød, Denmark) generates light pulses with a broad spectrum, from which spectrally narrow pulses are selected using a PC-controlled acousto-optical tunable filter (SuperK SELECT, NKT Photonics A/S, Birkerød, Denmark). Most of the light power is injected into the centre of the liquid phantom via a 400 μm core diameter graded index fibre. A tiny fraction of the power is routed around the sample for the purpose of timing stabilisation [31]. This timing reference further increases the

measurement accuracy by allowing for compensation of temporal drifts in the system. Both the light pulse collected at a predefined distance within the phantom and the pulse routed around it are detected by a single photon counting detector (PDM, Micro Photon Devices, Bolzano, Italy) connected to a time-correlated single photon counting (TCSPC) card (SPC-130 Becker & Hickl GmbH, Berlin, Germany). An appropriate light power for TCSPC was achieved using dedicated PC controlled optical attenuators (OZ Optics Ltd, Ottawa, Canada).

The PTOF signals were collected at a count rate of approximately 80 kHz for the duration of 32 seconds to yield approximately 2.5×10^6 counts per time-of-flight curve. The full width at half maximum of the instrument response function (IRF) is 53 ps and was taken into account during data evaluation by convolving it with the models. The IRF was measured through double-sided black printed office paper inserted between the source and detector fibres [34]. In this study we used 832 nm light. However, the actual wavelength is not of importance for model verification. The average optical power at the sample was approximately 3 mW.

The flat cut graded index fibres, inserted into thin stainless steel tubes for mechanical stability, were immersed in the phantom vertically from a metallic holder fixed to a stand. The separation between the fibres can be adjusted via a fitted micro gauge. The fibre separation was carefully measured from fibre centre to centre.

Three models for light propagation were implemented as MATLAB scripts for evaluation of μ_s' and μ_a from the recorded PTOF curves: the standard DM for isotropic media [21], a pre-calculated database based on a WMC algorithm [32, 35], and the LKM [24]. The optical properties were, in all cases, assessed with MATLAB, using a Levenberg-Marquardt algorithm on the measured PTOF data. The width of a time-bin used in the measurements was 3.0538 ps. The scattering anisotropy (g) of intralipid is not known exactly and has to be approximated. Diffuse reflectance measurements by Flock *et al*. [36] and Mie theory approximations by van Staveren *et al*. [37] suggest g = 0.79 and g = 0.62, respectively, at 832 nm. In our experiments, g = 0.7 was used for both LKM and WMC as an approximate mean value. This value was previously used for MCS [38] and has shown to produce accurate estimation for the optical properties of intralipid phantoms [32]. In all cases the thresholds for the model fitting range was set to 10% of the peak value on the rising edge and the falling edge, respectively. Additionally, a threshold of 90% of the peak value on the rising edge was also used to evaluate the optical properties with DM. The P_N-approximation RTE solution in the framework of the LKM depends on number of parameters that set balance between approximation accuracy and computational time [24]. The approximation order of N = 25 provided stabile LKM solutions in the whole range of evaluated optical properties. The other parameters, namely an approximation sphere radius of 50 mm and 100 discretization wavenumbers were used as suggested in original work by Liemert *et al*. [24]. Furthermore, in order to account for non-negligible core diameter (400 µm) of the source and detector fibres, in the analysis we average PTOF curves generated with DM and LKM over 16 distances between loci at the fibre tips, representing the distance distribution between the fibre cores [39]. WMC simulations, on the other hand, do not assume an isotropic source but are performed for a pair of fibres and their numerical aperture is already taken into account [32]. Also, WMC does not assume an isotropic source model. An example of the time resolved data set is presented in Fig. 2.

3. Results and discussion

The performance of the LKM was evaluated in two series of measurements, providing means to control its validity under conditions when the diffusion model is known to be inaccurate [35, 40]. The diffusion approximation is valid only when light has undergone a sufficiently large number of scattering events. In the first series of measurements we stepwise increased the pre-diluted ink concentration of the water/intralipid solution to gradually increase

absorption. In the second series, we tested the LKM performance by its ability to provide consistent evaluated properties at different source-detector fibre separations.
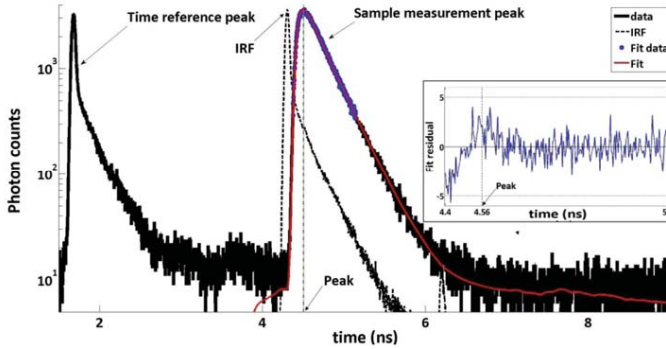

Fig. 2. An illustration of the time-resolved measurement with the tested LKM using PTOF spectroscopy and fit residuals (inset).
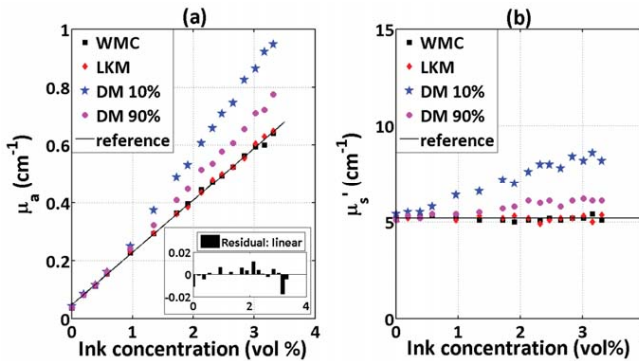

Fig. 3. Evaluated optical properties, μ_a in plot (a) and μ_s' in plot (b), presented for a ~2.8% (vol) of intralipid phantom with gradually increasing concentration of prediluted ink. Evaluations using WMC and LKM are depicted as black squares and red diamonds, respectively. The DM, with rising edge threshold at 10% of the peak and threshold at 90% of the peak, is presented with blue stars and magenta circles, respectively. The black lines present the linear fit to WMC data serving as reference value. The residual to the fit for (a) is presented in inset figure. The estimated specific absorption value for ink is 24 cm^{-1}.

In Fig. 3 the evaluated values of μ_a and μ_s' are plotted individually, for measurement series performed at 832 nm on intralipid phantoms with a reduced scattering coefficient of $\mu_s' \approx 5.2\,\text{cm}^{-1}$, and gradually increased ink concentration. The measurements were performed with a source-detector fibre separation of 15 mm, corresponding to approx. 8 times the effective scattering mean-free-path length. One can observe that the DM results in inaccurate estimations of μ_a and μ_s' when μ_a exceeds a value of approximately 0.3 cm^{-1}. In particular,

the limitation of the DM causes crosstalk in the evaluated optical parameters manifesting itself in a non-linear response in both absorption and reduced scattering with an increased ink concentration. Predictions of DM often has large errors when earlier part of the time profile before the peak is used in fitting. Therefore, we also use a threshold value of 90% of the peak on the rising edge in addition to the value of 10% to evaluate the performance of the DM. DM started to fail for higher absorption values. In contrast to DM, the values evaluated with LKM and WMC are consistent with the measurement protocol and produce a linear response in the entire evaluated absorption span. The residual of linear fit to WMC data, presented in Fig. 3(a) inset, shows the deviation of less than 4% from linear behaviour and 99% confidence interval for the slope of the regression line is 0.1807 ± 0.0051. For LKM, the deviation from linear behaviour is also less than 4%. In this study, we consider WMC as "gold standard" against which other techniques are evaluated as the accuracy of WMC with PTOFS is well established [34, 35, 41]. We note the small offset for zero ink concentration caused by residual absorption of other chromophores in the phantom. It has been shown that although the batch to batch variations of optical properties are large for India Ink, the ratio of specific absorption to extinction coefficient remains almost unchanged [42]. Using the suggested single scattering albedo value of 0.115 gives the specific extinction coefficient value of 27.1 cm^{-1}. By using the predilution ratio of 7.56×10^{-3} vol%, the specific absorption value of ink was estimated to be 24 cm^{-1}. This gives the absorption to extinction ratio of 0.8856. This value matches perfectly with the presented value by Ninni *et al.* [42]. Our results also fall within the range of specific absorption coefficients presented in [43] with large batch to batch deviations recorded. As it may be expected [28], LKM and WMC evaluated μ'_s remains fairly constant with measurement precision within 5% whereas μ_a grows linearly in proportion to the added ink volume. The differences between the optical parameters provided by the two techniques are within the precision of the measurements. Linearity of μ_a is observed for even very low ink concentrations [Fig. 3(a)]. This is achieved by limiting of the fitting interval at falling edge side of PTOF curve to 10% of the peak value, which removes the long photon path contribution to the fitted curve and allows avoiding influence of boundary losses. Thus, we conclude that LKM does indeed, provide as accurate values as MCS for evaluation of PTOF data in the entire range evaluated, i.e. up to $\mu_a \approx \mu'_s / 7$. Compared to WMC, LKM alleviates the need of developing new MCS and get PTOF distribution for arbitrary μ_a and μ'_s. We note that due to scalability of light propagation modelling for an isotropic infinite media [44, 45] the results of the current validation experiment can be readily generalized to other values of μ'_s corresponding to biological tissue [46], dairy products [30], and other diverse turbid samples.

Next, we investigated the dependence of the optical properties on the distance between the source and collection fibres. Ideally the evaluated μ'_s and μ_a are independent of the fibre separation. In Fig. 4, the resulting μ'_s and μ_a coefficients as evaluated by the DM, the LKM and the WMC model at various inter-fibre distances are presented for two phantoms with different optical properties. A general observation is that all models eventually break down at extremely short fibre separations, with tendency towards increased scattering and absorption. The performance of both the LKM and WMC is, however, significantly less affected at short distances in comparison to the DM. At short distance, DM model breaks down because of insufficient numbers of scattering events. In Figs. 4(c) and 4(d), we observe approximately 8.8% difference in mean absorption evaluated with WMC in high and low scattering phantoms. This difference can result from boundary effects that may have influenced our measurements specifically in the weakly scattering sample. However, it is important to note that the measured absorption values are extremely low (i.e. ca. 0.04 cm^{-1}) and by absolute value are comparable to the estimated accuracy of our setup. We also note that the apparent

breakdown of the WMC and LKM-based evaluation at the distance shorter than 6 mm does not necessarily suggest a failure of LKM, but most likely is coming from the limitations of the present experimental configuration. This may include different factors such as limitations of the finite fibre width modelling currently implemented in our evaluation script, poor temporal resolution, and inaccuracy in the estimated g value. Accurate verification of LKM performance at short inter-fibre separation would generally require higher temporal resolution of PTOF measurements than feasible with the current setup. Additionally, advanced fibre probe design may be needed in order to better fit to isotropic source approximation used in the modelling. Notably such experiment can also lead to highly accurate estimations of the intralipid scattering anisotropy (g) as it can be used as a fit parameter when using the LKM.
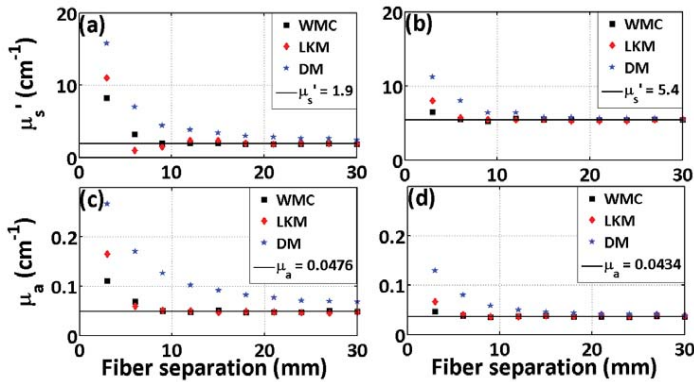

Fig. 4. Effect of source and detector fibre separation on evaluated optical properties for two different levels of scattering. The evaluated reduced scattering is presented in (a, b) and absorption in (c, d). The evaluated results by WMC, LKM and DM are depicted as black squares, red diamonds and blue stars, respectively. Black lines indicate the mean value of optical property evaluated using WMC, excluding the first 2 measurements in 'a' and 'c' and the first measurement in 'b' and 'd'.

The current findings are fully consistent with the recent LKM verification of heuristic models presented by the Kienle group [28, 29]. Eliminating the need for extensive pre computations of MC simulations, PTOF spectroscopic evaluation is computationally effective and opens a potential for future in-line applications requiring fast analysis. Additionally, the robust parameterisation presented in this article shows the strong linearity and independence of the instrument setup for the optical properties. The present assessment thus provides an independent validation of the model and robustness of the system for parameters relevant for many biomedical and industrial applications.

4. Conclusions

We presented the first independent experimental verification of a semi-analytical model for solving the radiative light transport equation in scattering turbid media in infinite geometry, recently presented by Liemert and Kienle [24]. The performance of the standard diffusion approximation, a Monte-Carlo based algorithm and the Liemert-Kienle model for evaluation of PTOF data measured on ink/intralipid solution series with various absorber concentrations and at various source-detector separations was compared. We emphasize that this is the first case that the LKM in infinite geometry is used for evaluation of experimental data and the first time it is independently verified by MCS. We observed that the LKM performs equally

well as the WMC in the range of optical and measurement parameters where diffusion approximation is inaccurate, which suggests that the LKM is a very good approximation in this parameter regime. The range of investigated optical properties covers materials ranging from biological tissue to fruits and dairy products. The availability of computationally efficient analytical approximations of the radiative transport equation constitutes an important prerequisite in the field of diffuse optical spectroscopy. The results suggest that the LKM, together with its recent extension to semi-infinite measurements geometry [47], may facilitate a broad range of applications for time-of-flight spectroscopy in the future.

PAPER IV

Sensitivity analysis for Oblique incidence reflectometry using Monte Carlo simulations.

Faisal Kamran, Peter E. Andersen.

Sensitivity Analysis for Oblique Incidence Reflectometry Using Monte Carlo Simulations

FAISAL KAMRAN[1,*] **AND PETER E. ANDERSEN**[1]

[1] *Technical University of Denmark, Department of Photonics Engineering, Frederiksborg 399, Denmark, 4000*
Corresponding author: faisal309@gmail.com

Oblique incidence reflectometry has developed into an effective, non-contact and non-invasive measurement technology for the quantification of both the reduced scattering and absorption coefficients of a sample. The optical properties are deduced by only analysing the shape of the reflectance profiles. This article presents the sensitivity analysis of the technique in the turbid media. Monte Carlo simulations are used to investigate the technique and its potential to distinguish the small changes between different levels of scattering. We present various regions of dynamic range of optical properties in which the system demands vary to be able to detect subtle changes in the structure of the medium, translated as measured optical properties. Effects of variation in anisotropy are discussed and results presented. Finally, experimental data of milk products with different fat content is considered as an example for comparison. © 2015 Optical Society of America

1. INTRODUCTION

Accurately estimated optical properties of highly scattering media, also known as turbid media, are indispensable in biomedical science. An arsenal of measurement techniques [1–4] and theoretical advances [5–10] to capture light propagation in turbid media is a testimony to its significance. The microstructure of turbid media holds huge significance because of its influence in altering various optical properties of the medium [11–15]. As optical properties indicate changes in chemical composition and/or structural organization of a sample, their quantification may improve product quality [16] and help estimate macroscopic effects of the molecular structure. Oblique incidence reflectometry (OIR) [17] is one of the techniques, developed over the last two decades to investigate turbid media for quantification of their optical properties. In addition, its simplicity and non-destructive approach makes it feasible for non-contact, non-invasive real time measurements.

Light propagation in homogeneous turbid media is a complicated phenomena, determined by the sample geometry and the following four optical properties of the medium [18]: the refractive index n, the mean cosine of the scattering angle (the asymmetry parameter or anisotropy) g, the absorption coefficient μ_a and the scattering coefficient μ_s. Light transport in turbid media is a complicated phenomenon. Scattering is influenced by the structural characteristics of the material, such as density, cellular structures and the interfaces between cells. Absorption, on the other hand, is related to the chemical constituents of the material;

hence, it can be used to probe the chemical constituents of samples. In a strongly scattering material, photons often undergo multiple scatterings before being absorbed or being re-emitted from the material. Such multiply scattered light is referred to as diffuse light which can be spatially resolved using fibre probes or a camera and presented as diffuse reflectance profile, R(r). Light's behaviour is changed in the diffuse regime and different combinations of two individual properties may lead to the same effect, which is explained by similarity relation [19]. From diffuse light, instead of measuring μ_s, the reduced scattering coefficient $\mu_s' = \mu_s(1 - g)$ may be extracted by fitting an analytical expression to the shape of R(r). This poses a challenge in separating μ_s and g, once the bulk property of μ_s' has been extracted from R(r).

OIR is a non-invasive optical measurement technique, capable of extracting μ_a and μ_s' by analysing the spatially resolved diffuse reflectance profiles. Both optical fibre [20–22] and camera [17, 23–25] based approaches have been demonstrated. However, OIR is a technique based on a diffusion model and thereby has inherent limitations due to approximations made in constraining light transport theory. The two important questions are: a) what parameters cause the physical changes in a sample that influence the optical properties and b) how sensitive is the method of observing these changes? Dairy products consumed globally often in the form of milk, powder, cheese, cream or yoghurt are good examples of the diversity in products caused by various controlled changes.

Milk is a complex emulsion of fat and protein particles in water. The basic difference in various forms of milk is the fat percentage, which is the main cause of scattering in dairy products. Transforming milk into various products begins with pretreatment of milk and then the addition of starter culture to initiate fermentation process. The details of processes and physical food properties are already covered [26, 27]. These processes are designed to change the pH value of milk by increasing acidity levels and causing change in the microstructure. These changes are both time and temperature sensitive and require strict control, thus demanding ways to measure those changes accurately. For commercially available milk and stirred yoghurt products, the μ_s' could range from ~5 cm^{-1} to ~80 cm^{-1} for different fat levels [14]. It may not be essential, however, to cover the whole dynamic range of the properties. Depending on whether optical properties are observed near the lower or higher values in the aforementioned dynamic range, the resolution requirements for sensitivity to measure the change could vary.

Monte Carlo (MC) simulation [28] offers a dynamic and flexible approach to model light propagation in turbid media. Recent development of a 3D MC model [29] for light propagation in heterogeneous structures has made it easy to adapt the modeling for a wide range of applications. Sensitivity analysis, in terms of resolution, of OIR with this gold standard can shed light on the accuracy and precision of not only the technique but the requirements of the measurement system as well. It is the sensitivity to changes in scattering that requires a certain performance of the detection scheme.

In this paper we explore the OIR technique using MC simulations to determine the working limits on resolution of an imaging system, within which the system can reliably produce the desired results. The importance of a priori knowledge of g is emphasized for the accurate estimation of optical properties. We show that the technique itself is limited only by its implementation and measurement accuracy of the instrument. Our sensitivity analysis shows that subtle changes in the scattering properties of the sample can impose resolution requirements on system depending on the scale of the changes produced in the sample. In this way we can determine to what extent the expected optical properties have to alter before producing a detectable change in estimated/measured properties by the system. We use the sensitivity analysis to assess the performance of an imaging system in terms of accurate distinction of subtle changes in optical properties which may arise due to subtle change in the structure or chemical composition of the sample during production stage. In the end we compare the MC results with previously presented results on milk samples with different fat content.

2. MATERIALS AND METHODS

A. Oblique incidence reflectometry

Wang et al. [17] proposed OIR based on an isotropic source point which was further developed by Lin et al. [20] into a 2-point source model. The light incident on the surface of a sample at an angle refracts and travels in the medium at least one transport mean free path (1mfp') before it encounters any optical interaction with particles of the medium. Based on MC results [17, 20], 1mfp' was given as:

$$1mfp' = \frac{1}{0.35\mu_a + \mu_s'} \tag{1}$$

Close to the entry point, light does not lose its directionality

and retains information about anisotropy of the medium. But as it travels farther, the directionality is lost and light becomes diffuse with uniform distribution in all directions. The center of this diffuse part is called diffusion center which is displaced by a distance Δx from the entry point. Estimation of Δx is one of the most important factors as it enforces resolution requirements on the measurement systems and is directly related to the estimation of μ_s'. This link is established through diffusion coefficient, D [20]

$$3D = 1mfp' = \frac{n_{med}\Delta x}{Sin\theta_i} \tag{2}$$

where θ_i is the incident angle and n_{med} is refractive index of the medium. OIR is based on diffusion approximation to transport theory which assumes a positive point source buried in the medium. Eq. 1 and Eq. 2 show the actual position of that point source in the medium and how it is shifted due to angular incidence of light, governed by Snell's law.

Within the diffusion limit, light propagation can be modelled by the analytical expression for light propagation using diffusion approximation [20]. It is used to fit the diffuse portion of the reflectance profile to estimate the total attenuation coefficient μ_{eff}. These two parameters, Δx and μ_{eff}, can be used to estimate the desired optical properties:

$$\mu_a = D\mu_{eff}^2 \tag{3}$$

$$\mu_s' = \frac{1}{3D} - 0.35\mu_a \tag{4}$$

For media with high albedo, absorption has negligible effect and μ_s' is almost entirely dependent on accurate estimation of Δx. Light decay in a diffuse medium is based on absorption of the medium and the diffusion coefficient which relates the shape dependent spatial distribution of diffuse reflectance profile to its attenuation coefficient [20]. Eq. 3 and Eq. 4 express the link between optical properties and shape of the profile in diffusion approximation.

B. Oblique monte carlo

Acknowledged as a gold standard, Monte Carlo can provide an optimal numerical validation for any method based on simulating radiative transfer. We used the open source 3D MC model [29] for simulating light propagation in turbid media. The code was modified to accept the incident light at an angle and a data library of oblique MC profiles for the range of scattering properties was created. An infinitely small beam of photons was launched at an angle on the surface of a medium defined by fixed μ_a, μ_s and g. The sample is a cube of cube-shaped voxels for storing energy as photons propagate through them. The energy stored on the top surface of the medium, as a result of photon transport in the medium and returning to the surface, serves as a diffuse reflectance map. The laser beam shape and size are taken in account by convolving with the surface profile. To extract a diffuse reflectance profile from MC simulation, a line is scanned on the surface along the direction of incidence beam. The apparent diffuse center of the profile was calculated using the method explained by Lin et al. [20].

Anisotropy values of $g = 0.7$, $g = 0.8$, $g = 0.9$ and $g = 0.95$ were used to investigate the significance of g in OIR. For simplification, we kept $\mu_a = 0.02$ cm^{-1} for sensitivity analysis and $\mu_a = 0.05$ cm^{-1} for experimental verification, to mimic its negligible effect [30] for high albedo, in both cases. The number of photon packets used for simulations varied between 5-10
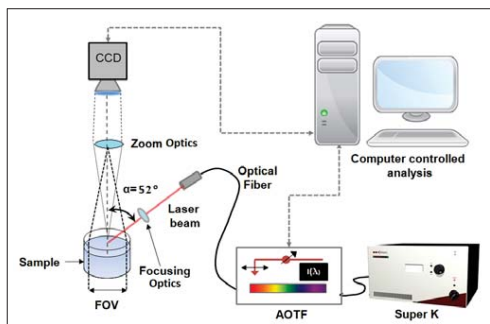
Fig. 1. Illustration of oblique incidence reflectometry setup. FOV = field of view, AOTF = acousto-optic tunable filter. $\alpha =$ light entrance angle.

Fig. 2. A simulated spectrograph of diffuse reflectance profiles for OIR with μ_s' changing from 5 to 80 cm^{-1}. $g = 0.7$ and $\mu_a = 0.02$ cm^{-1}. The displacement is shown by movement of the diffuse profile center as a shift.

Fig. 3. Displacement as a function of reduced scattering for a range of μ_s' in an high albedo turbid medium.

million depending upon optical properties and each simulation was run for 30 minutes.

C. Experimental verification

The ability to resolve the changes occurring within the scatterer structure of a turbid medium is dependent upon the sensitivity of the instrument, as well as the technique itself. MC simulated OIR was used to explore the sensitivity requirements of measuring system considering dairy products, i.e., milk, as an example.

Nielsen et al. [25] recently showed reliable estimation of optical properties of dairy products using OIR with instrument built for in-line inspection. The experimental setup is shown in Fig. 1. We used the milk data as an example to study effects of g as well as sensitivity requirements of the measuring system. The assumed refractive index of milk is, $n_{milk} = 1.347$ [31]. The CCD camera used had a resolution of 8 mega pixel with a final 3.2μm pixel size on image surface.

The collimated laser beam at an incidence angle projects an elliptical profile on the sample surface which is convolved with MC simulations to take the shape and size of the beam into account. The light intensity does not have impact on OIR profile other than the signal clarity. To simulate the real system measurements, the important parameter is the effective resolution on the CCD which is the result of field of view (FOV), focal length and magnification of the collection lens. MC profiles were compared to experimentally acquired profiles of 0.5% fat, 1.5% fat and 3.5% fat milks at 9 different wavelengths i.e., 500-900nm at 50nm interval. We used a MATLAB script with a Levenberg-Marquardt fitting algorithm on the MC simulated data to deduce optical properties. Using Lorenz-Mie theory [32], estimated μ_s' is fitted with '$a\lambda^{b'}$' over measured wavelengths. 'a' relates to the concentration of the scatterers while 'b' distinguishes the size of the particles.

3. RESULTS AND DISCUSSION

Figure 2 shows an example of a simulated spectrogram of diffuse reflectance profiles based on oblique MC fitted with **R(r)** from the OIR model. The extended dynamic range of μ_s' in arbitrary turbid medium is presented as a function of displacement produced. The image is in false colour and an overview of the effects

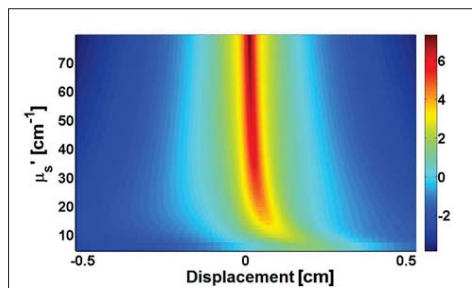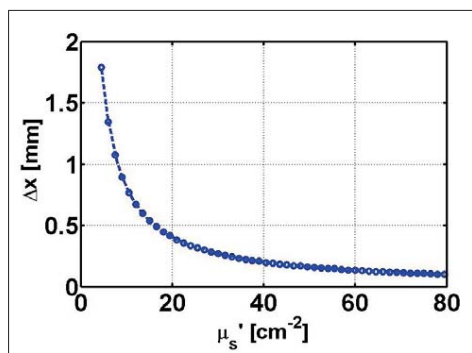produced by different scales of μ_s' can be seen. For high scattering, tails of the profile are well defined (green-blue regions) that indicate diffuse light while for low scattering, although intensity center has displaced enough, the diffusion process has not yet entirely taken place in the image range. In order to measure the displacement, the required sensitivity of the instrument varies based on the range of scattering. Figure 2 shows two system requirements:

- Ability to resolve displacement for high scattering regimes as the profiles are tightly squeezed close to the entry point (indicated by 0).

- Wide field of view for low scattering to acquire sufficient part of the diffuse profile for the fitting procedure.

Larger values of scattering produced very small Δx with a well defined scattering profile. However, decrease in reduced scattering ensures that light travels further before entering the diffuse regime; thus producing larger displacements of the diffusion center.

The change produced by μ_s' is, however, relative to the dynamic range. This is visualized in Fig. 3 showing Δx as a function

Table 1. Table to give length scales of optical interactions for a wide dynamic range of reduced scattering in a high albedo turbid medium. $\mu_a = 0.02cm^{-1}$ and $g = 0.7$. $\delta\Delta x$ = change in Δx caused due to 10% change in μ'_s, FOV = field of view requirement, Resolution = resolution requirement, ↓ or ↑ = direction of increase.

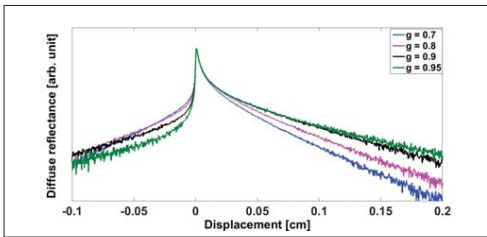| $\mu'_s(cm^{-1})$	ExpectedΔx (μm)	$\delta\Delta x$ ($\pm\mu m$)	FOV	Resolution
80	99.2	9.6	↓	↑
70	112	9.6	↓	↑
60	131.2	12.8	↓	↑
50	156.8	12.8	↓	↑
40	198.4	19.2	↓	↑
30	262.4	22.4	↓	↑
20	393.6	35.2	↓	↑
10	787.2	73.6	↓	↑

Fig. 4. Effect of phase function, g, on changing diffusion profile.
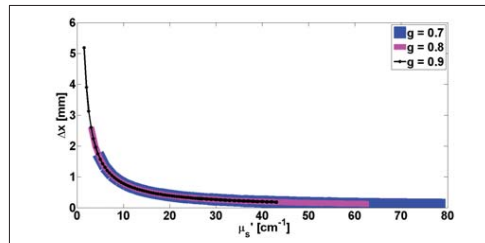

Fig. 5. Shift in dynamic range and resolution requirement of optical properties caused by g parameter.

tion of the reduced scattering coefficient, thus emphasizing the fact that resolution requirements of a system depends on the dynamic range of the reduced scattering. In Fig. 3, a wide range of μ'_s is modelled using MC simulations and the corresponding Δx is estimated. The range of Δx produced is from 102 μm to 1.79 mm from high to low scattering respectively. To emphasize the changing resolution requirements, μ'_s was varied in consistent steps of 1.5 cm^{-1} which corresponds to 30% change in lowest scattering and 1.9 % change in highest scattering regions respectively. This variation in relative change, produced in optical properties, translates into the measurable quantity, namely displacement (Δx). Whether that displacement can be detected by the imaging system depends on the resolution of the system. A small change in a relatively dilute medium can produce a large easily detectable change in Δx while a similar change in an optically dense medium may not be detectable at all by the same system. Thus, appropriate resolution of a system to measure such change becomes paramount in reliable estimation of optical properties. This requirement will be further discussed with an example in Table 1, see further below.

Another factor affecting the OIR estimated properties is the wavelength dependence of the anisotropy g [33], which is an inherent limitation and a potential source of error in OIR [34]. As OIR is diffusion-based method, information on the anisotropy is lost before the method becomes valid. Thus, any change in g that alters the diffuse profile is instead linked to the scattering

of the medium. This makes a priori knowledge of g, in a sample, of high relevance as an inaccurately assumed g will affect the results. Figure 4 shows the changes introduced to estimated diffusion profiles by varying g while all other properties are kept constant. The similarity relation states that light propagation in a medium is not affected when μ'_s is kept unchanged thus producing similar profiles for simultaneously varying μ_s and g. However, this strictly holds for diffuse light and accordingly close to the surfaces or sources one experiences the effects of the individual properties. When light is incident at an angle, anisotropy has an angular component along a horizontal direction which causes a change in the profile. This change can be reflected as variation in estimation of the diffuse center of the profile when sample optical properties are changed even while keeping the μ'_s constant.

Changes in light propagation caused due to whether μ'_s or only g are both translated into displacement of the diffusion center in a similar way, affecting the estimation of optical properties. In Fig. 5, again the modelled μ'_s range is used to estimate Δx but this time with varying g. Figure 5 shows the effect of a change in g on dynamic range of optical properties. By increasing g from 0.7 to 0.9, the range of μ'_s is reduced thus increasing the estimated Δx. For lower values of g, light experiences more scattering but as g approaches 1, scattering starts to disappear and light propagates through the medium. In Fig. 5 it can observed
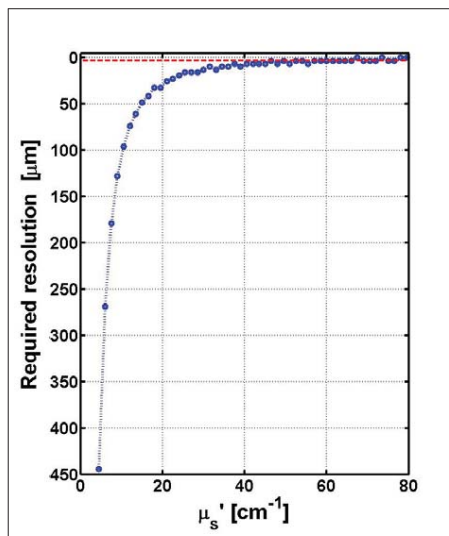
Fig. 6. Required resolution to detect a change of 1.5 cm^{-1} in μ'_s at different dynamic ranges of scattering. Red horizontal line marks the 3.2 μm pixel size.

that for $g = 0.7$, μ'_s ranges from 5 to 80 cm^{-1}. But with $g = 0.9$ the range changes from 1.5 to 43 cm^{-1}. This change in g has a stronger effect on higher scattering values. However, even large jumps between optical properties produce very little affect on the measurable displacement. To be able to detect these changes accurately, the resolution requirements are extremely high. On the other hand, towards the lower scattering values, changing g can produce large measurable displacements which can easily be measured, making a system sensitive to such variations.

These variations limit an imaging systems' range for measuring different media as the optical properties are expressed at different length scales. In general, to cover a wide range of μ'_s, an imaging system with very high resolution as well as wide field of view (FOV) would be ideal. Such high-end system can be complex and expensive. If, on the other hand, the need is to investigate a confined (smaller) range of properties, a standard and less expensive camera or objective may suffice.

To illustrate how resolution requirements of an imaging system change, Table 1 presents μ'_s at various scales in dynamic range. A 10% change is introduced in μ'_s and the corresponding change in estimated displacement ($\delta\Delta x$) is presented. For each value of μ'_s, a MC profile is generated, model is fitted and finally both Δx and $\delta\Delta x$ are estimated. Δx is measured as a difference between the light entry point and apparent diffuse center of the profile determined using the method described by Lin et al. [20]. $\delta\Delta x$ is estimated by recording the variation in Δx caused by change in the profile due to 10% change in reduced scattering coefficient. These changes affect the FOV and effective resolution required. As shown, the change produced in Δx, by the same percentage variation of optical property, varies significantly over the range of μ'_s. This variation dictates the imaging

system demands and there is often a compromise between the two requirements: FOV and resolution. As light travels further in low scattering media, a larger FOV is necessary to cover tails of diffusion profile over several centimetres. For high scattering a smaller FOV is better to provide higher resolution at the CCD plane to be able to resolve small displacements. As FOV is the spatial distribution of the light captured on the CCD, it has to be wide enough to cover diffuse section of the light. The distance over which the light may become diffuse varies from few millimetres for highly scattering media to 4-6 cm for very low scattering media. The baseline can be set based on experimental inspection. The wavelength of the light plays an important role in setting baseline as lower wavelengths scatter more than higher wavelengths, needing a relatively smaller FOV. Resolution is defined by density of pixels on a CCD frame and can be changed by altering the pixel size to pack less or more number of pixels. More pixels can sample the same profile better which is an advantage. A CCD frame with large pixel size will have higher signal to noise ratio but will not be able to resolve fine changes. The same CCD frame with smaller pixel size possesses better resolving power albeit at the expense of lower signal to noise ratio.

We can divide $\delta\Delta x$ into three regions: under $\sim$20 μm, between 20-70 μm and above 70 μm. Any change below 20 μm is physically undetectable without the use of a microscope objective. Between $\sim$20-70 μm, a high resolution camera with $\sim$1.5 2 times magnification of objective lens and noise filtering, could detect the change. Above $\sim$70 μm, a standard 6-8 MP camera with pixel size range of 3-5 μm would suffice to accurately measure the change.

The sensitivity to the change in scattering, changes with the amount of scattering itself. In Fig. 6, this sensitivity is shown in terms of estimated resolution requirements for various ranges of μ'_s. For lower scattering values, the changes produced are large which makes the resolution requirement relaxed. However, as scattering increases, the changes produced are smaller thus tightening the resolution requirements as well. Although theoretically, it appears that a 3.2 μm pixel size (indicated by the red line) should be sufficient to measure these changes in whole dynamic range, practically, however, it is not feasible. Signal to noise ratio in CCDs decreases proportionally with decreasing pixel size thus making it hard to accurately distinguish between intensity levels in neighbouring pixels. This increases uncertainty in estimation of small changes and often require over $\sim$15-20 pixels to reliably resolve a change. This means that to accurately measure a change in scattering, the displacement produced should be at least $\sim$45-65 μm apart on CCD. As the change gets smaller, the error in estimation increases due to higher uncertainty.

In Fig. 7, we compare our estimated results from oblique MC simulations to experimentally acquired measured data using the OIR on dairy products. Measurements of μ'_s on three milk samples with varying fat content are shown in green error bars (for 5 repetitive measurements). The brown curve is the Lorenz-Mie theory prediction for the μ'_s as function of wavelength. For all 5 measurements on a each sample, at 9 different wavelengths in the range of 500-900nm with 50nm step size, we used oblique MC data base to match the profiles and estimate μ'_s. The procedure was repeated for $g = 0.7$, $g = 0.8$ and $g = 0.9$ with $a\lambda^b$ fit through the mean of 5 repeated measurements. The results indicate the variations of estimated μ'_s from that of MC simulations. These differences can be attributed to two important aspects of OIR:
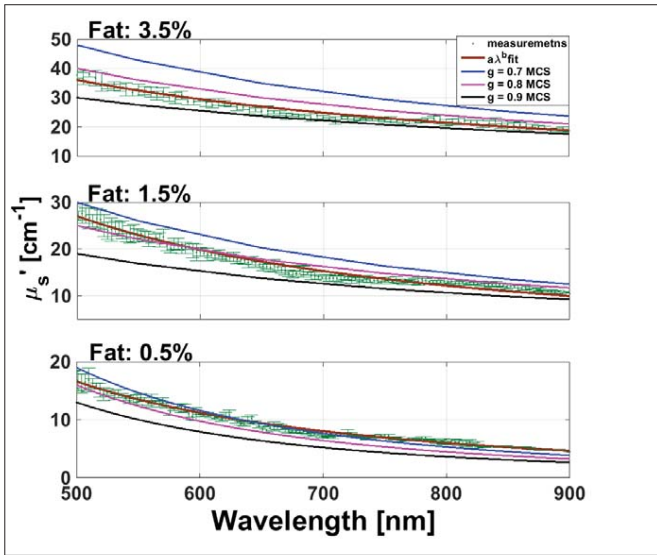
Fig. 7. Reduced scattering measurements on milk samples (green) with different fat content [25] along with fitted Lorenz-Mie theory approximation, $a\lambda^b$ fit (brown curve). Lorenz-Mie approximations fitted through oblique MC measurements with different g values are also presented for comparison as blue, magenta and black lines. MCS = Monte Carlo Simulation.

- model based variation and

- inaccuracies related to estimation of g

Model based variation is an inherent characteristic of the technique. Modelling assumptions and approximations put limits on the accuracy of measurements. The entry point estimation is a major hurdle in camera based approaches for real-time measurements of OIR. Because of finite beam size and elliptical projection of beam profile on the surface, it is a challenge to get the exact entry point of the light into the medium. Another limitation on accuracy is cross-talk which is inter communication between μ_a and μ_s' [35] especially for low albedo. In milk, either water absorption peaks or sample residual absorption can cause cross-talk affecting the accuracy below 500nm and above 900nm. The cross-talk effect can be removed by post processing of estimated properties or pre-compensating the profiles for such effects based on prior knowledge.

Inaccuracy in assumption of g value for milk is another major source of error. Experimental results shown in Fig. 7 were achieved with assumption of g=0.7. However, it has been reported that in practice, the g value can vary from 0.68 for regular milk with blue light to 0.93 for low fat milk at red light [36]. As shown in Fig. 5, change in g can cause deviations in the measured Δx, thus an inaccurate assumption of g in OIR can lead to inaccurate estimate of μ_s', emphasizing the significance of a priori knowledge of g. This implies that, given good resolution of the system, the OIR technique can produce estimates with good precision but the accuracy is compromised which leads to differences in OIR and MC results. We can observe the g variation effects in the mismatch of results as well. In the region where the assumed g is possibly close to the actual g, a close

match is observed between MC results and the measurements but they start to deviate as the mismatch grows. The OIR can over estimate results especially with tight resolution requirements or limited FOV where there is not enough diffuse profile for fitting. This factor can also introduce mismatch to the MC simulated results. As this effect is prominent towards higher values for the scattering, we note the larger variations towards high scattering values at lower wavelengths compared to low scattering values at higher wavelengths.

Inaccurate estimation of the light entry point is another important factor contributing towards uncertainty in measuring Δx. In milk measurements by OIR, perturbations across the light entry point observed on the CCD were spread over $\sim$ 20-30 pixels producing uncertainty in a range of $\sim$ 60-90 μm for the estimation of the center. In Fig. 6, the μ_s' below $\sim$ 15 cm^{-1} start producing displacements that fall outside this limit. This low uncertainty in displacement estimate can be observed as high precision measurements for μ_s' below $\sim$15 cm^{-1} indicated by small error bars on OIR measurements in Fig. 7. As μ_s' increases, the uncertainty in estimation also increases up to 15% shown by larger error bars. Δx is calculated as thr distance between two estimates: more reliably estimated diffusion center, and light entry point affected by light intensity profile and perturbations on CCD pixels. Thus the entry point estimation becomes dominant factor in determining the effective resolution of the system because of the uncertainty it may introduce.

Theoretically, OIR is not resolution limited but the method is limiting with the definition of its application in the diffuse region. From OIR, it is not possible to get g of the medium because solving the inverse problem can lead to only μ_s'. To correctly estimate the entry point, a priori knowledge of g can also be useful

for tracing back the light to its origin. This might be achieved by analyzing higher order moments of non-diffuse light that are close to the center. Although, experimental measurements are affected by both cross-talk and the effect of anisotropy, g is not quantified in OIR, indicating that it could be a stronger influence on limiting accuracy. In summary, it is important to potentially include anisotropy estimation in measurements [37, 38] to improve upon the accuracy of the method.

4. CONCLUSIONS

In this paper, we addressed the issue of sensitivity related to oblique incidence reflectometry (OIR). We used MC simulations to demonstrate a large dynamic range of optical properties of a high albedo turbid medium to analyse the scales of optical interactions at various regions of dynamic range. We showed that the resolution requirement of OIR is dependent on the scale of reduced scattering.

We have shown the effects of varying anisotropy on the estimated optical properties and the displacements produced by OIR. We propose that to improve the accuracy of OIR measurements, it is essential to incorporate the wavelength dependence of g, methods to accurately quantify the entry point of the light into the medium and compensation for cross-talk.

We showed that a compromise has to be made between resolution and FOV of an imaging system to achieve reliable performance from an imaging system. To measure small changes in optically dense samples, resolution is the key system requirement while wide FOV is necessary to image optically dilute samples.

By comparing MC simulations to OIR measurements of milk samples with varying fat content, importance of a priori knowledge of g was made clear. The comparison also provided evidence in support of sensitivity analysis conducted using MC simulations.

REFERENCES

1. F. Martelli and G. Zaccanti, "Calibration of scattering and absorption properties of a liquid diffusive medium at nir wavelengths. cw method," Optics express **15**, 486–500 (2007).
2. U. Netz, I. Gersonde, J. Toelsner, and G. Illing, "Frequency domain diffuse fluorescence tomography for detection of deep lesions," in "European Conference on Biomedical Optics," (Optical Society of America, 2011).
3. J. Stott and D. Boas, "A practical comparison between time-domain and frequency-domain diffusive optical imaging systems," in "Biomedical Topical Meeting," (Optical Society of America, 2002).
4. V. Ntziachristos and B. Chance, "Accuracy limits in the determination of absolute optical properties using time-resolved nir spectroscopy," Medical physics **28**, 1115 (2001).
5. C. Crofcheck, F. Payne, and M. Mengüç, "Characterization of milk properties with a radiative transfer model," Applied optics **41**, 2028–2037 (2002).
6. C. Fagan, M. Castillo, F. Payne, C. O'Donnell, M. Leedy, and D. O'Callaghan, "Novel online sensor technology for continuous monitoring of milk coagulation and whey separation in cheesemaking," Journal of agricultural and food chemistry **55**, 8836–8844 (2007).
7. D. Álvarez, M. Castillo, Y. Xiong, and F. Payne, "Prediction of beef meat emulsion quality with apparent light backscatter extinction," Food Research International **43**, 1260–1266 (2010).
8. J. Qina and R. Lub, "Hyperspectral diffuse reflectance for determination of the optical properties of milk and fruit and vegetable juice," .
9. J. Qin and R. Lu, "Measurement of the absorption and scattering properties of turbid liquid foods using hyperspectral imaging," Applied spectroscopy **61**, 388–396 (2007).
10. J. Qin and R. Lu, "Monte carlo simulation for quantification of light transport features in apples," Computers and electronics in agriculture **68**, 44–51 (2009).
11. R. Samatham, P. Campagnola, and S. L. Jacques, "Optical properties of mutant versus wild-type mouse skin measured by reflectance-mode confocal scanning laser microscopy (rcslm)," Journal of biomedical optics **13**, 041309–041309 (2008).
12. J. L. Skytte, O. H. A. Nielsen, U. Andersen, J. M. Carstensen, A. L. Dahl, R. Larsen, F. Møller, F. Kamran, and J. R. Frisvad, "Decomposition of diffuse reflectance images-features for monitoring structure in turbid media," in "InsideFood Symposium," .
13. B. M. Agrawal and M. P. Mengüç, "Forward and inverse analysis of single and multiple scattering of collimated radiation in an axisymmetric system," International Journal of Heat and Mass Transfer **34**, 633–647 (1991).
14. O. H. A. Nielsen, A. A. Subash, F. D. Nielsen, A. B. Dahl, J. L. Skytte, S. Andersson-Engels, and D. Khoptyar, "Spectral characterizations of dairy products using photon timeof- flight spectroscopy," Near Infrared Spectroscopy **21**, 375–383 (2013).
15. F. Bijnen, H. Van Aalst, P.-Y. Baillif, J. Blonk, D. Kersten, F. Kleinherenbrink, R. Lenke, and M. Vander Stappen, "In-line structure measurement of food products," Powder technology **124**, 188–194 (2002).
16. C. Soukoulis, P. Panagiotidis, R. Koureli, and C. Tzia, "Industrial yogurt manufacture: monitoring of fermentation process and improvement of final product quality," Journal of dairy science **90**, 2641–2654 (2007).
17. L. Wang and S. L. Jacques, "Use of a laser beam with an oblique angle of incidence to measure the reduced scattering coefficient of a turbid medium," Applied optics **34**, 2362–2366 (1995).
18. A. Welch and M. van Gemert, *Optical-thermal response of laser irradiated tissue* (Springer, 2011).
19. H. Van De Hulst, "Multiple light scattering. vols. _1_and_2." New York NY (USA): Academic Press, 739 p. **1** (1980).
20. S.-P. Lin, L. Wang, S. L. Jacques, and F. K. Tittel, "Measurement of tissue optical properties by the use of oblique-incidence optical fiber reflectometry," Applied optics **36**, 136–143 (1997).
21. A. Garcia-Uribe, K. C. Balareddy, J. Zou, and L. V. Wang, "Micromachined fiber optical sensor for in vivo measurement of optical properties of human skin," Sensors Journal, IEEE **8**, 1698–1703 (2008).
22. A. Garcia-Uribe, J. Zou, M. Duvic, J. H. Cho-Vega, V. G. Prieto, and L. V. Wang, "In vivo diagnosis of melanoma and nonmelanoma skin cancer using oblique incidence diffuse reflectance spectroscopy," Cancer research **72**, 2738–2745 (2012).
23. T. Lindbergh, M. Larsson, I. Fredriksson, and T. Strömberg, "Reduced scattering coefficient determination by non-contact oblique angle illumination: methodological considerations," in "Biomedical Optics (BiOS) 2007," (International Society for Optics and Photonics, 2007), pp. 64350I–64350I.
24. P. Sun, X. Cao, R. Yang, F. Xie, J. Ding, and F. Zhang, "Basic research on determining optical properties of tissues in vivo by measuring diffuse reflectance with a charge-coupled device," Optica Applicata **41**, 541–555 (2011).
25. O. H. A. Nielsen, F. Kamran, A. B. Dahl, J. L. Skytte, F. D. Nielsen, P. E. Andersen, R. Larsen, and J. Frisvad, "Non-invasive assessment of dairy products using spatially resolved diffuse reflectance spectroscopy," Submitted to Applied Spectroscopy **-**, – (2014).
26. J. A. Lucey, "Cultured dairy products: an overview of their gelation and texture properties," International Journal of Dairy Technology **57**, 77–84 (2004).
27. W. Lee and J. Lucey, "Formation and physical properties of yogurt," Asian-Aust. J. Anim. Sci **23**, 1127–1136 (2010).

28. L. Wang, S. L. Jacques, and L. Zheng, "Mcml—monte carlo modeling of light transport in multi-layered tissues," Computer methods and programs in biomedicine **47**, 131–146 (1995).

29. S. Jacques and S. Prahl, "optical properties," http://omlc.ogi.edu/education/ (2012). [Online; accessed 01-Dec-2014].

30. T. Svensson, E. Alerstam, M. Einarsdóttír, K. Svanberg, and S. Andersson-Engels, "Towards accurate in vivo spectroscopy of the human prostate," Journal of Biophotonics **1**, 200–203 (2008).

31. A. J. Jaaskelainen, K. E. Peiponen, and J. A. Raty, "On reflectometric measurement of a refractive index of milk," Journal of dairy science **84**, 38–43 (2001).

32. J. R. Mourant, T. Fuselier, J. Boyer, T. M. Johnson, and I. J. Bigio, "Predictions and measurements of scattering and absorption over broad wavelength ranges in tissue phantoms," Applied Optics **36**, 949–957 (1997).

33. P. Thueler, I. Charvet, F. Bevilacqua, M. S. Ghislain, G. Ory, P. Marquet, P. Meda, B. Vermeulen, and C. Depeursinge, "In vivo endoscopic tissue diagnostics based on spectroscopic absorption, scattering, and phase function properties," Journal of biomedical optics **8**, 495–503 (2003).

34. L. V. Wang and S. L. Jacques, "Source of error in calculation of optical diffuse reflectance from turbid media using diffusion theory," Computer methods and programs in biomedicine **61**, 163–170 (2000).

35. E. Alerstam, S. Andersson-Engels, and T. Svensson, "Improved accuracy in time-resolved diffuse reflectance spectroscopy," Opt. Express **16**, 10440–10454 (2008).

36. S. G. Narasimhan, M. Gupta, C. Donner, R. Ramamoorthi, S. K. Nayar, and H. W. Jensen, "Acquiring scattering properties of participating media by dilution," ACM Transactions on Graphics (TOG) **25**, 1003–1012 (2006).

37. T. Svensson, R. Savo, E. Alerstam, K. Vynck, M. Burresi, and D. S. Wiersma, "Exploiting breakdown of the similarity relation for diffuse light transport: simultaneous retrieval of scattering anisotropy and diffusion constant," Optics letters **38**, 437–439 (2013).

38. E. Alerstam and T. Svensson, "Observation of anisotropic diffusion of light in compacted granular porous materials," Physical Review E **85**, 040301 (2012).